

# Exploiting the Optical Limits of Thin-Film Solar Cells: A Review on Light Management Strategies in Cu(In,Ga)Se<sub>2</sub>

António J. N. Oliveira, Jennifer P. Teixeira,\* Duarte Ramos, Paulo A. Fernandes, and Pedro M. P. Salomé

Light management strategies are of utmost importance to allow Cu(In,Ga)Se<sub>2</sub> (CIGS) technology market expansion, as it would enable a conversion efficiency boost as well as thinner absorber layers, increasing sustainability and reducing production costs. However, fabrication and architecture constraints hamper the direct transfer of light management architectures from other photovoltaic technologies. The demand for light management in thin and ultrathin CIGS cells is analyzed by a critical description of the optical loss mechanisms in these devices. Three main pathways to tackle the optical losses are identified: front light management architectures that assist for an omnidirectional low reflection; rear architectures that enable an enhanced optical path length; and unconventional spectral conversion strategies for full spectral harvesting. An outlook over the challenges and developments of light management architectures is performed, establishing a research roadmap for future works in light management for CIGS technology. Following the extensive review, it is expected that combining antireflection, light trapping, and conversion mechanisms, a 27% CIGS solar cell can be achieved.

desired impact. The conventional energy distribution model, based on one-way flow from central generation stations to end users, is moving toward a more decentralized and efficient energetic foster practice.<sup>[1,2]</sup> This energy fostering concept is gaining momentum as a virtual network/community of distributed energy resources and storage systems, ensuring a balance between local energy generation and demand.<sup>[3–7]</sup> Among all forms of distributed energy resources, the most common scheme is centered in residential-scale photovoltaic (PV) systems.<sup>[1,2]</sup> Thus, energy market decentralization is strongly dependent on an effective reduction in the PV (and storage) costs and on an expansion in the landscape- and, more importantly, building-integrated PV (BIPV), as currently it is estimated that 90% of electricity consumption occurs in urban areas.<sup>[8]</sup>


The PV generation costs are remarkably linked with the solar cells' power conversion efficiency value.<sup>[9]</sup> Accordingly, the current forecasts for reductions in the levelized cost of electricity (LCoE) depend on: 1) research and technology progress, focused to increase the efficiency value of PV module production and 2) increase in the PV production economy of scale. Regardless of the silicon (Si) wafer technology leadership in the PV market, those cells are fast approaching an economical and a technological development plateau. From the PV commercially available portfolio, Cu(In,Ga)

## 1. Introduction

An increased demand for energy has emerged, as we are experiencing an era of continuous and fast technological progress. To meet that request and net zero emissions by midcentury, demand-side management has to set the aforementioned technological progress to good profit. Energy systems are facing a global transition—that is clear—however, and so far, not yet with the

A. J. N. Oliveira, J. P. Teixeira, D. Ramos, P. A. Fernandes, P. M. P. Salomé  
INL—International Iberian Nanotechnology Laboratory  
Avenida Mestre José Veiga  
4715-330 Braga, Portugal  
E-mail: jennifer.teixeira@inl.int

A. J. N. Oliveira, P. A. Fernandes  
i3N  
Departamento de Física da Universidade de Aveiro  
Campus Universitário de Santiago  
3810-193 Aveiro, Portugal

 The ORCID identification number(s) for the author(s) of this article can be found under <https://doi.org/10.1002/adpr.202100190>.

© 2022 The Authors. Advanced Photonics Research published by Wiley-VCH GmbH. This is an open access article under the terms of the Creative Commons Attribution License, which permits use, distribution and reproduction in any medium, provided the original work is properly cited.

DOI: 10.1002/adpr.202100190

A. J. N. Oliveira, P. M. P. Salomé  
Departamento de Física  
Universidade de Aveiro  
Campus Universitário de Santiago  
3810-193 Aveiro, Portugal

D. Ramos  
Departamento de Ciência dos Materiais  
Faculdade de Ciências e Tecnologia  
Universidade Nova de Lisboa  
Campus de Caparica, 2829-516 Caparica, Portugal

P. A. Fernandes, P. M. P. Salomé  
CIETI  
Departamento de Física  
Instituto Superior de Engenharia do Porto  
Instituto Politécnico do Porto  
Porto 4200-072, Portugal

Se<sub>2</sub> (CIGS) solar cells can potentially produce cheaper modules than Si, with comparable electrical performance due to a high absorption coefficient enabling thin layers;<sup>[10]</sup> great thermodynamic stability; solid record efficiency;<sup>[11]</sup> one-step module manufacturing, with a low number of participants in the value chain;<sup>[12]</sup> already commercialized in flexible substrates;<sup>[13]</sup> and low-energy payback time.<sup>[8]</sup> Despite these favorable features, and the remarkable progress in terms of efficiency value in the last decade,<sup>[11,14,15]</sup> the CIGS module production has stagnated.<sup>[16]</sup> It is clear that the CIGS marketplace strongly depends on an efficiency boost, along with a decrease in the raw materials consumption, that is, through a sharp reduction in its production cost and on diminishing the cell-to-module efficiency gap.<sup>[17]</sup> Indeed, CIGS thin-film-based solar cells have demonstrated efficiency values of 23.35%,<sup>[11]</sup> which is still far from the monocrystalline Si (mono-Si) record value of 26.6%.<sup>[18]</sup> A significant part of this gap in state-of-the-art efficiency values, between mono-Si and CIGS technologies, is due to their differences in cell design complexity. For instance, conventional CIGS solar cells lack light management strategies, and passivation has predominantly been tackled through alkali-based doping<sup>[19–23]</sup> and in-depth bandgap gradients,<sup>[24–29]</sup> presenting mostly the same architecture since the 1980s.<sup>[30,31]</sup>

High-efficiency CIGS solar cell devices commonly have a substrate configuration, as depicted in **Figure 1a** and shown in **Figure 1b**, where an illustration of the CIGS solar cell architecture, as well as a photograph of a real cell, are presented, respectively. The required CIGS off-stoichiometry composition, as well as its complex nature with four atomic elements, contribute to a high recombination density, which leads to increased open-circuit voltage ( $V_{oc}$ ) losses. Modified in-depth bandgap gradients and alkali postdeposition treatments (PDT) have been successfully explored to decrease recombination and improve the  $V_{oc}$  value. Furthermore, various optical loss mechanisms limit the performance of thin devices, such as shading from the metallic contacts, reflection, and parasitic absorption in the window and buffer layers. Therefore, state-of-the-art thin-film CIGS devices can be improved using broadband angle-independent antireflection (AR), light trapping, and spectral conversion strategies.

A decrease in the manufacturing cost and higher throughput can be accomplished by thinned-down absorbers, ultrathin (<700 nm). A reduced thickness would additionally result in a

higher steady-state carrier density per volume, hence dampening bulk recombination effects and theoretically resulting in an increased  $V_{oc}$  value.<sup>[32,33]</sup> However, ongoing attempts to reduce CIGS thickness have led to a significant decrease in the performance compared with state-of-the-art thin devices,<sup>[11,34]</sup> as ultrathin solar cells are more affected by a high recombination velocity at the rear and incomplete light absorption. Conventionally in CIGS, an in-depth bandgap gradient, manifested as an increase in the conduction band minimum energy value toward the rear contact, effectively reduces the rear interface recombination rate.<sup>[25]</sup> Such a concept is far from optimized for ultrathin cells.<sup>[35]</sup> Thus, other strategies, such as patterned dielectric layers, have been studied.<sup>[36–40]</sup> Moreover, in ultrathin solar cells, the absorber thickness value is lower than the optical thickness required to fully absorb the incoming light, resulting in high optical losses, which leads to a short-circuit current density ( $J_{sc}$ ) value decrease.<sup>[41–43]</sup>

In PV technologies, such as Si-based,<sup>[44,45]</sup> dye-sensitized,<sup>[46,47]</sup> and perovskite,<sup>[48,49]</sup> light management approaches ranging from microscale to several nano-optical concepts have been explored aiming to decrease optical losses, with several works reviewing the existent light management strategies in each technology.<sup>[50–54]</sup> Despite the efforts to implement light management in the aforementioned solar cells, in CIGS devices, these schemes have mostly consisted in the use of AR layers and replacement of the molybdenum (Mo) reflector.<sup>[11,55,56]</sup> Notwithstanding, the Mo rear contact replacement by a perfect reflective approach only allows for a twofold increase in the optical path length. As a comparison, light-trapping systems demonstrating optical path length enhancements close to the Lambertian limit— $4n^2$ , where  $n$  stands for the refractive index—have been demonstrated for mono-Si technology.<sup>[52,57]</sup> Hence, in ultrathin CIGS solar cells, it is of critical importance to implement nanophotonic or plasmonic schemes that would enable longer optical path lengths, by trapping light in the absorber.  $J_{sc}$  enhancement obtained through light trapping yields a logarithmic increase in the  $V_{oc}$  value and additionally an optimized optical architecture may allow for an  $V_{oc}$  increase, through photon recycling. An optimized light confinement increases the probability of reabsorption of photons emitted upon radiative recombination at the CIGS layer.<sup>[58]</sup> Nonetheless, for an effective

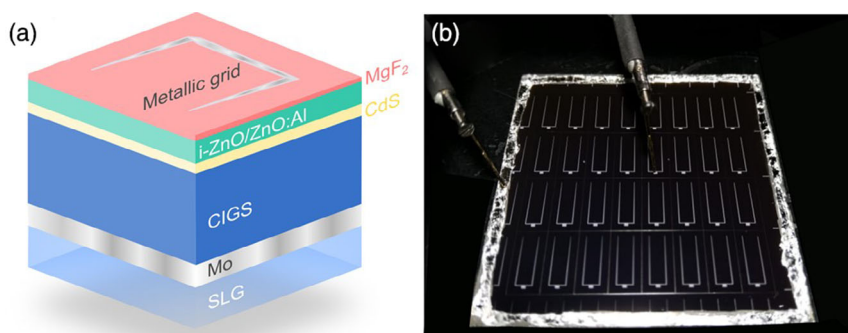


**Figure 1.** a) Schematic representation of a conventional CIGS solar cell: a rigid SLG substrate coated with molybdenum (Mo), then the heterojunction composed of CIGS p-type and cadmium sulfide (CdS) n-type layers, followed by an i-ZnO/ZnO:Al (AZO) window, and finally an AR magnesium fluoride (MgF<sub>2</sub>) coating and the metal grids. b) Photograph of a real CIGS solar cell during current–voltage illuminated measurements.

$V_{oc}$  increase, the radiative recombination rate should be dominant over nonradiative, highlighting the importance of very high material quality.<sup>[58]</sup> Thus, efficient light-trapping strategies are required, for ultrathin CIGS technology to be able to preserve or even surpass the thin-film performance. Despite the benefits mentioned previously, up until now, photonic and/or plasmonic nanostructures integration in CIGS solar cells remains a complex step, as structural and fabrication constraints influence the viability of these light management approaches.<sup>[12,41,42,52,59]</sup> Before reaching the absorber, light travels through thick transparent conductive oxide (TCO) layers and a cadmium sulfide (CdS) buffer layer. Therefore, promoting a longer optical path length through light management schemes on the front CIGS cells layers may be challenging, as it leads to parasitic absorption in the window and buffer layers. Nevertheless, heavy alkali doping enables to use efficient thinner CdS layers in the CIGS solar cell without electrical losses, allowing for an improved optical response.<sup>[23]</sup> In contrast, different wide-bandgap materials, such as Zn(O,S),  $Zn_{1-x}Sn_xO_y$ ,  $Zn_{1-x}Mg_xO$ ,  $In_2S_3$ , or even the Zn(O,S,OH)<sub>x</sub>/Zn<sub>0.8</sub>Mg<sub>0.2</sub>O double layer used in the current CIGS champion cell, have been studied as buffer layers, enabling a better UV solar cell response than CdS.<sup>[12,60–64]</sup> In regard to the implementation of light management schemes at the absorber rear, the CIGS deposition process needs to be contemplated, essentially if we consider that the CIGS layer is usually deposited by coevaporation at temperatures above 500 °C in an aggressive selenium (Se) atmosphere.<sup>[12]</sup> Hence, the thermal and chemical stability of rear light management schemes is of utmost importance. For instance, direct implementation of gold (Au) or silver (Ag) layers or nanostructures is difficult, as these metals would diffuse into the absorber, degrading the device electrical performance.<sup>[65]</sup> Nevertheless, CIGS solar cells produced under low substrate temperatures have already presented promising results.<sup>[66]</sup> Substrate temperatures lower than 350 °C have been successfully used in a Ag-based alloy (ACIGS) solar cell.<sup>[67]</sup> This expertise might be a key element to provide a wider portfolio of rear optical schemes to the CIGS technology. Thus, it is crucial to understand if nanophotonic and plasmonic architectures can be integrated in CIGS technology, to take full advantage of their light management benefits and access thin and ultrathin solar cells' full potential. M. Schmid provides a comprehensive review over strategies and current challenges to implement nanostructures, more particularly metallic and dielectric nanoparticles (NPs), in ultrathin solar cells to shrink the gap to the thin counterpart.<sup>[41]</sup> In the present review, a detailed description of the implementation of light management architectures in both thin and ultrathin CIGS solar cells is performed. Furthermore, the advances done so far in spectral conversion strategies in CIGS solar cells, that can boost the  $J_{sc}$  to values above the limit established by Shockley and Queisser (SQ), are as well discussed. Optical modeling and simulations are key pillars for the development and optimization of advanced light management.<sup>[68]</sup> Therefore, an extensive selection of the works reviewed herein are based on optical modeling of light management architectures in CIGS solar cells. Those models can be classified according to the dimensions of the simulated features with respect to the incident light wavelength.<sup>[69]</sup> In the cases where the simulated features are much larger than the incident light wavelength, macro-optical models based on geometric optics are often used. These models are centered in

equations and theory that can describe light by its intensity or photon flux without the need for phase information of electromagnetic waves, such as ray tracing.<sup>[69]</sup> Hence, macromodels allow to perform extensive iterative optimization procedures.<sup>[68]</sup> Nonetheless, to accurately simulate complex geometries with dimensions lower or at the same scale of the incident wavelength, macromodels based on geometric optics are insufficient, as electromagnetic wave propagation of light needs to be considered.<sup>[69]</sup> Combinations of different methods and theories, such as effective medium theory (EMT), scalar scattering theory, transfer matrix method, or scalar vector theory, might be used to simulate this optical problem.<sup>[69]</sup> However, often valid descriptions for the complex situations cannot be found analytically and rigorous optical modeling approaches are required.<sup>[69]</sup> These models are able to provide a better description of complex architectures by solving the Maxwell equations on the considered structures. Several numerical methods with different spatial discretization schemes of the simulation domain, such as finite-difference time domain (FDTD),<sup>[43]</sup> finite-element method (FEM),<sup>[70]</sup> and rigorous coupled wave analysis (RCWA),<sup>[71]</sup> have been used to rigorously solve the Maxwell equations in complex light management architectures in CIGS solar cells, ranging from the integration of NPs in the solar cell structure to subwavelength-textured surfaces. However, a dense spatial subwavelength discretization of the simulated architectures is required by any of the available solving methods. Hence, the complexity of the simulation method may become too large, requiring high computational resources.<sup>[69]</sup>

This article contains six sections, including Introduction (Section 1). In Section 2, an overview of the optical loss mechanisms in CIGS solar cells is made, while in Section 3, an in-depth review of the reported light management architectures is presented, with a critical analysis on their viability and capability to enhance the optical performance in CIGS devices. The light management benefits of the current state-of-the-art mono-Si solar cell architecture are presented in Section 4, along with a discussion on their viability to be integrated into CIGS devices. In Section 5, a comprehensive summary of the reviewed light management strategies is performed, establishing research guidelines for future works in light management for CIGS solar cells. In addition, there is an Experimental Section to detail information about simulations presented in this work, as well as the search criteria for the overview of the light management field.

## 2. Demand for Light Management

Conventionally, a single-junction solar cell efficiency upper limit is established by the SQ model.<sup>[72]</sup> Ultimately, the solar cell efficiency limit of  $\approx 33\%$  predicts an optimal bandgap of 1.34 eV.<sup>[73]</sup> Nevertheless, the SQ detailed balance considers a step function for the materials absorbance depending on a single physical property, the absorber bandgap energy value, which is a rather simple assumption. Absolute zero light reflection is not compatible with solar cell (multi-)media optical properties; indeed, CIGS solar cells' layers have  $n$  ranging from 1.89 to 2.96 and extinction coefficient ( $k$ )  $> 0$ .<sup>[10]</sup> Moreover, tail states at the edges of CIGS conduction and valence bands extend the density of states into the bandgap, violating the SQ assumption of a step-function absorbance.<sup>[74,75]</sup> Thus, when the SQ model is compared with

real solar cell devices, it overestimates the solar cell efficiency, while underestimating the physical fundamentals governing the solar cell working principle. Thereby, there are a considerable number of studies that assess features beyond the SQ model, considering absorber and architecture key criteria.<sup>[76–80]</sup> As an example, Rau and Kirchartz conceptually demonstrated that for real cells' absorbance, a Gaussian distribution function should be used to describe the absorption edge, instead of an ideal step function.<sup>[80]</sup> Notwithstanding, the SQ model is still widely used to evaluate solar cell performance, as its abstraction level allows for a fair crosslink between technologies. Thus, while the Si technology already reached 97% of the  $J_{sc}$  value predicted by the SQ limit, thin-film CIGS world record cell only achieved 89%.<sup>[11,18]</sup> Nonetheless, the world record mono-Si architecture presents interdigitated back contacts (IBCs) that avoid shading losses, optimized AR, light trapping, and passivation.<sup>[18]</sup> The introduction of the same capabilities in the CIGS world record device would bring  $J_{sc}$  from  $39.6 \text{ mA cm}^{-2}$ <sup>[11]</sup> to  $43.2 \text{ mA cm}^{-2}$  and increase the power conversion efficiency from the world record value of 23.35% to 25.51%. However, the scenario when

a 490 nm CIGS champion cell is considered is far behind what is required for ultrathin technological dissemination, performing just at 70% of its correspondent  $J_{sc}$  SQ limit value.<sup>[34]</sup> In this framework, CIGS still has a significant technological potential to shrink the gap from the present state-of-the-art efficiency values and its theoretical upper limits. In the way to reach upper conversion efficiency values, the present review brings a roadmap to tackle optical losses assigned to CIGS solar cells via light management approaches.

Any process that prevents efficient light absorption is considered an optical loss. Various mechanisms are responsible for hindering the complete harvesting of the solar spectrum that reaches the solar cell, as shown in **Figure 2a**, along with the respective  $J_{sc}$  loss for an ultrathin CIGS solar cell.<sup>[81]</sup> First, the phenomena that prevent light to reach the absorber layer have to be considered. Shading effects from the solar cell metallic contacts will reduce the active area, leading up to  $1 \text{ mA cm}^{-2}$  of  $J_{sc}$  loss. However, other contact design architectures enable the minimization or even elimination of shading effects, as in the case of IBCs.<sup>[18,82]</sup> In contrast, as the incident light interacts with the

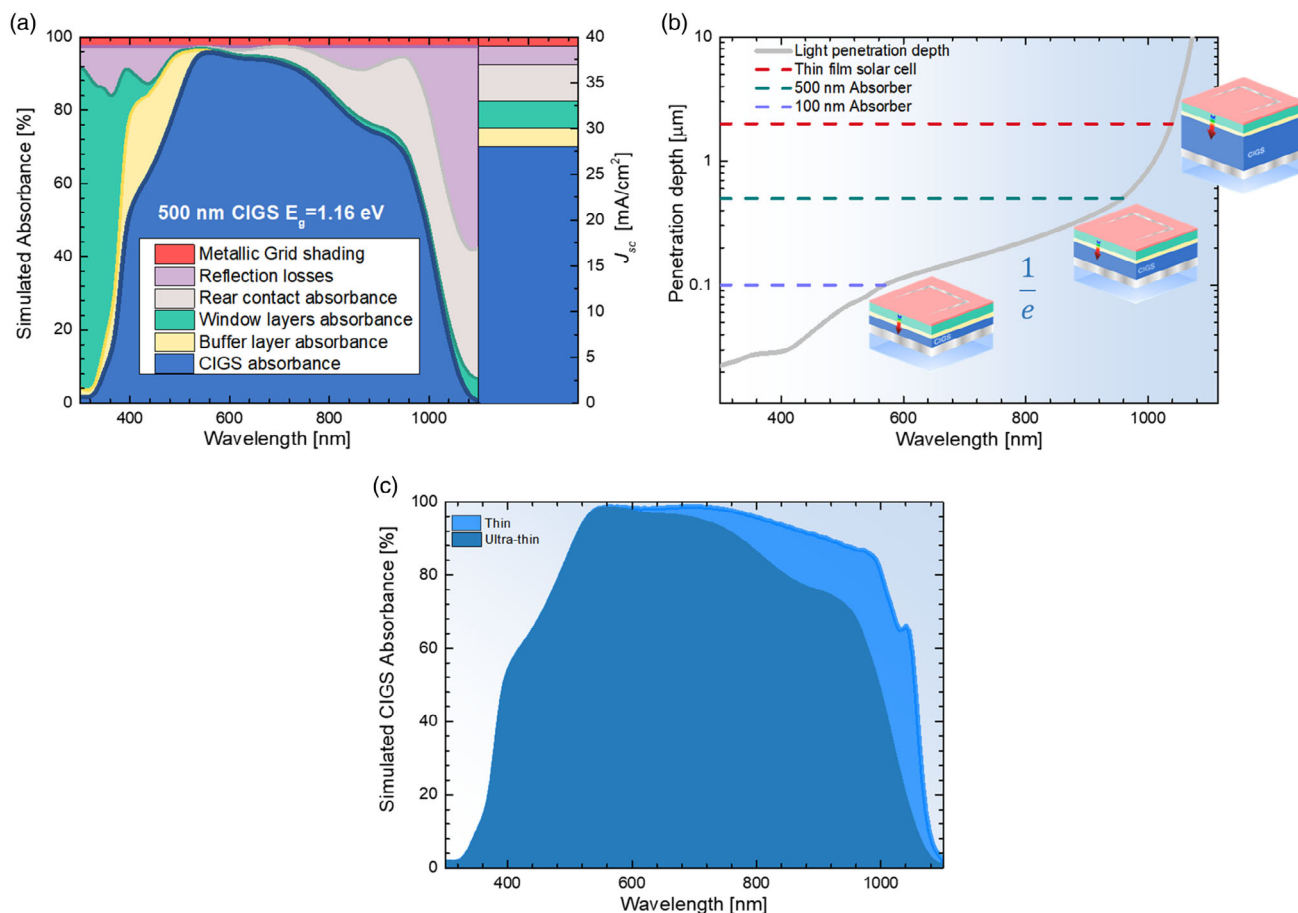


**Figure 2.** a) Simulated ultrathin CIGS solar cell absorbance with corresponding  $J_{sc}$  loss values for the following architecture: 350 nm Mo/500 nm CIGS (1.16 eV bandgap)/50 nm CdS/100 nm ZnO/400 nm AZO. b) Penetration depth of light—the distance from the surface where light intensity drops by a factor of  $1/e \approx 37\%$ —as a function of wavelength in a bulk CIGS material with typical composition of  $[\text{Ga}]/[\text{Ga}+\text{In}]$  (GGI) = 0.3. Penetration depth values of 100, 500, and 2000 nm are highlighted to illustrate significant wavelength values to which an efficient light absorption can still be maintained, for different absorber layer thicknesses. c) Simulated CIGS absorbance of thin (2000 nm) and ultrathin (500 nm) solar cell devices (without metallic grid shading), with the same architecture as in (a).

solar cell air-front surface, a fraction of it is reflected, accounting for a  $J_{sc}$  loss of  $2 \text{ mA cm}^{-2}$ . This phenomenon results from the  $n$  offset between the air and the solar cell front medium. A change in the  $n$  value must be overcome, to minimize front surface reflection. Hence, AR strategies have to be employed to decrease this optical loss. In addition, light can be absorbed prior to reaching the CIGS layer, which adds up to a  $5 \text{ mA cm}^{-2} J_{sc}$  loss. This parasitic effect arises from free carrier absorption at the IR region, as well as from absorption at energy values ranged above the bandgap energy, from the window and the buffer layers, which does not contribute to the photocurrent.<sup>[10,41,60,83,84]</sup> Hence, it is termed parasitic absorption. Minimization of the latter effect involves thickness optimization of the front solar cell layers and their replacement by materials with higher-bandgap energy values. CdS is the typical buffer layer in a CIGS device, with a bandgap energy value of around 2.4 eV. Nonetheless, alternative compounds with higher-bandgap energy values have been explored as potential replacements.<sup>[11,60–64]</sup> It is noteworthy that currently both lab-scale and module cell world record architectures use Cd-free buffer layers.<sup>[11,85]</sup> Alternatively, luminescent materials able to convert high-energy photons into lower energy ones can be exploited to tackle the parasitic absorption losses.<sup>[86]</sup> However, with ultrathin absorbers, other optical phenomena have to be considered. Despite the direct-bandgap nature and consequent high absorption coefficient of the CIGS technology, submicrometer thickness poses a problem—incomplete light absorption. In Figure 2b, the optical penetration depth in a CIGS absorber is presented. In thin absorbers (2000 nm), a single pass of the incident light becomes enough for it to be absorbed up to wavelength values close to 1000 nm. However, as the technology moves toward the ultrathin regime, the absorption limit shifts to lower-wavelength values. Such inability to absorb low-energy photons in ultrathin devices leads to a lower  $J_{sc}$  value. The incomplete light absorption effect is shown in Figure 2c, where the simulated CIGS absorbance of a thin and ultrathin layer is compared. At wavelength values higher than 600 nm, the 500 nm CIGS absorber starts to underperform in comparison with the 2000 nm counterpart, leading to a  $4 \text{ mA cm}^{-2}$  decrease of the  $J_{sc}$  value. Overall, research efforts should be directed in finding and implementing cost-effective light management schemes that would allow to suppress the optical losses inherent to the conventional architecture performance and reach or even surpass the predicted limit, independently of the CIGS absorber thickness.<sup>[87]</sup>

The efficiency of the solar cell is limited by its lack of sensitivity to the AM 1.5 G solar spectrum, which encompasses a wavelength range between 280 and 2500 nm. However, single-junction solar cells only take advantage of a small portion of the solar spectrum, as the spectral response is limited by the absorber bandgap energy value.<sup>[86,88,89]</sup> Photons with energy lower than the bandgap energy value will not be absorbed, and the excess energy arising from the absorption of photons with energy much higher than the bandgap will be released as heat and not used to generate electron–hole pairs, in a process named thermalization.<sup>[86]</sup> These nonabsorption and thermalization losses can be decreased using luminescent layers in single-junction solar cell devices, able to convert IR and UV/vis spectral ranges to values that better match the solar cell spectral response,<sup>[86,89]</sup> or using multijunction solar cell devices that

efficiently respond to different spectral regions.<sup>[90,91]</sup> In the UV regime, between 280 and 400 nm, there is  $1.35 \text{ mA cm}^{-2}$  available. Downshifting (DS) or downconversion (DC) with a quantum yield of 95% would allow for a power conversion efficiency of 26.3%, if applied to the current world record solar cell with the same optical losses as Si (25.51%). In the same way, in the wavelength range from the corresponding value of the champion cell CIGS bandgap (1148 nm) to 1300 nm, there are around  $6 \text{ mA cm}^{-2}$ . However, even considering a still challenging 25% quantum yield in an upconversion (UC) process, an increase in  $1.5 \text{ mA cm}^{-2}$  would be obtained providing a solar cell with an efficiency of 27.1%, by adding this approach to the aforementioned ones. Hence, these calculations together with the exhaustive review of several promising technologies provide a roadmap of several strategies that would allow for a significant increase in the performance of current CIGS solar cells.

### 3. Light Management Strategies in CIGS Solar Cells

Light management schemes are essential to increase the number of photons absorbed in the active layer. Most of the reviewed light management concepts can be applied to both thin and ultrathin technology, particularly the ones concerning an enhanced light incoupling and improved spectral response. However, light-trapping schemes are critical in ultrathin solar cells, where incomplete light absorption problems become evident. Nonetheless, an improved light trapping is also beneficial in thin-film solar cells, as a 2000 nm CIGS layer can only efficiently absorb wavelength values up to 1000 nm. Therefore, in this section, an evaluation over the light management strategies applied to CIGS solar cells will be presented, with a critical outlook on the limitations and benefits of each approach. Section 3 is divided into front light management, rear light management, and spectral conversion strategies. Section 3.1 details the advances performed in light management schemes applied at the solar cell front layers for an omnidirectional AR, such as interference-type AR coatings, texturization, and resonant architectures. In Section 3.2, rear-contact metallic mirrors, texturization, and resonant architectures to increase the optical path length in the CIGS absorber are explored. Finally in Section 3.3, full-spectrum harvesting through spectral conversion strategies in single-junction CIGS devices is detailed.

#### 3.1. Front Light Management Strategies

An extensive discussion of the light management schemes applied at the front architecture of the CIGS solar cell, to provide an omnidirectional reflection minimization, is performed herein. Nonetheless, some of the light management strategies detailed in this section have complementary functionalities, such as an increase in the optical path length in the CIGS absorber, through light scattering, as shown in Figure 3. This section will start with the most basic AR concept, already widely applied in champion cells, which is an interference-type dielectric coating. However, the AR coating (ARC) strategy does not satisfy the omnidirectional low-reflectance condition. Other approaches have been researched for that purpose, such as microscale

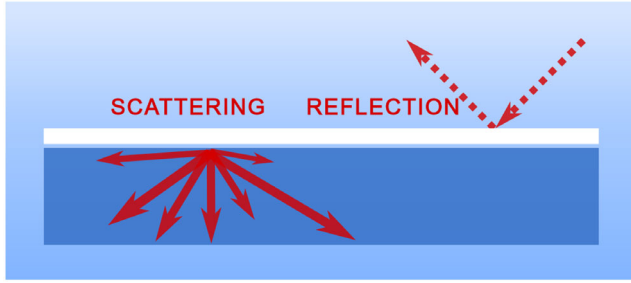


**Figure 3.** Schematic illustration of the light management mechanisms that can be used at the front of CIGS solar cells. Scattering for a prolonged optical path length in the CIGS absorber and broadband and wide-angle AR schemes to minimize the front-surface reflection.

texturization, resonant schemes, and nanoscale texturization, each with its own set of advantages and disadvantages.<sup>[92]</sup>

### 3.1.1. Interference-Type AR Coatings

The most common and simple AR strategy is a thin dielectric layer at the top surface of the solar cell, in which destructive interference effects between reflected light rays can promote an enhanced light incoupling.<sup>[93–104]</sup> As a simplistic approach, the solar cell top interface can be considered for the material and thickness optimization of the thin AR layer. In **Figure 4**, a schematic illustration that describes the light reflection and refraction phenomena, when the AR layer is placed in the top solar cell surface, is shown. Considering the AR layer to be dielectric 2, the incident light will be reflected from the interface dielectric 2 ( $n_2$ )/dielectric 1 ( $n_1$ ), as well as from the dielectric 3 ( $n_3$ )/dielectric 2 ( $n_2$ ) interface. Depending on the total phase difference between the reflected rays,  $r_{12}$  and  $r_{23}$ , constructive or destructive interference may occur, enabling a decreased or enhanced overall AR, respectively. Typically, for an optimized AR layer performance, the  $n$  of the involved layers should be organized in a grading manner ( $n_1 < n_2 < n_3$ ) or  $n_1 > n_2 > n_3$ .<sup>[93]</sup> With a grading  $n$ , a destructive interference between reflected

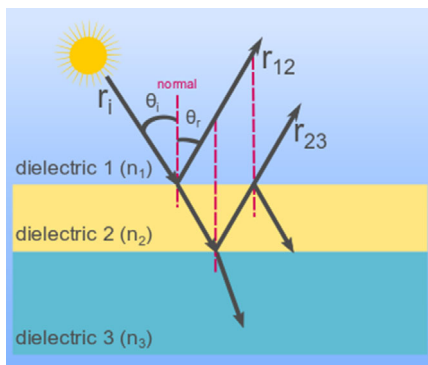


**Figure 4.** Schematic illustration of an incident ray reflection, at a thin dielectric layer, with refractive index  $n_2$  in between two dielectric media with refractive indices  $n_1$  and  $n_3$ , with  $\theta_i$  and  $\theta_r$  being the incident and reflected angles of the incident ray and  $r_{12}$  and  $r_{23}$  being the reflected rays from the upper and lower interface of dielectric 2.

light rays is achieved when the path difference ( $\delta$ ) satisfies the following rule<sup>[93]</sup>

$$\delta = 2d = \left(m + \frac{1}{2}\right) \frac{\lambda}{n_2} \quad (1)$$

with  $d$  being the thickness of the AR layer,  $m$  a whole number, and  $\lambda$  the incident light wavelength value. For an AR layer thickness that satisfies Equation 1, the overall front reflectance is given by

$$R = \left(\frac{n_1 n_3 - n_2^2}{n_1 n_3 + n_2^2}\right)^2 \quad (2)$$

A detailed derivation of the front reflection, by solving the Maxwell electromagnetic equations with appropriate boundary conditions, is performed in the study by Solanki et al.<sup>[93]</sup> For zero reflectance, an optimum  $n_2$  value can be found according to

$$n_2 = \sqrt{n_1 n_3} \quad (3)$$

as for a CIGS cell, the AZO layer has  $n_3$  of 1.9 at 600 nm and air  $n_1$  of 1. Therefore, the correspondent  $n_2$  value is equal to 1.38. It is important to consider that in a commercial module the ARC is placed between the AZO layer and a glass cover ( $n_1$  of 1.4).<sup>[17]</sup> In this case, the optimum  $n$  value changes to 1.63. Magnesium fluoride ( $\text{MgF}_2$ ) with  $n$  of 1.38 at 600 nm is typically the chosen material for an ARC in CIGS solar cells.<sup>[11,41,102–105]</sup> Nevertheless, considering the complex CIGS solar cell architecture, and that the CdS ( $n = 2.89$  at 600 nm)/ZnO ( $n = 1.98$  at 600 nm)/AZO ( $n = 1.89$  at 600 nm)<sup>[10]</sup> multilayer already demonstrates a gradual  $n$  decrease, the AR improvements in CIGS solar cells have been mostly optimized with a single  $\text{MgF}_2$  layer.<sup>[11,15,31]</sup> Adding multiple AR layers would lead to increased production complexity, manufacturing costs, and hinder fabrication throughput.<sup>[106]</sup> To find the AR layer optimal thickness value, all the inactive layers that act as an obstacle between air and CIGS have to be considered.<sup>[107,108]</sup> Rajan et al. demonstrated the dependence of the optimal  $\text{MgF}_2$  thickness value on the individual solar cell layers' thickness variation: CIGS absorber (500–2500 nm), the CdS buffer (20–90 nm), and the AZO window (150–300 nm).<sup>[108]</sup> To do so, the authors used a transfer matrix theory optical model combined with in situ real-time spectroscopic ellipsometry measurements, while depositing the AR layer, to measure the unpolarized reflection as a function of the AR thickness. With such an approach, both theoretical models and experimental results demonstrated that as the individual solar cell layers thickness values are modified, the optimum  $\text{MgF}_2$  thickness has to be adjusted to achieve a minimum reflectance.

Initially, AR layers, such as silicon dioxide ( $\text{SiO}_2$ )<sup>[109]</sup> and silicon nitride ( $\text{Si}_3\text{N}_4$ ),<sup>[110]</sup> were implemented in CIGS devices, in accordance with AR developments in mono-Si technology. However,  $\text{MgF}_2$  is the standard material used in high-efficiency devices since the 1990s.<sup>[111,112]</sup> Up to the current world record cell,  $\text{MgF}_2$  has been the material of choice for an ARC, having suffered only small thickness variations throughout the years, arising from different solar cell windows and buffer layer architectures in champion devices. Thus, architectural changes demand an optimization of the ARC, which has an optical impact

on the solar cell device. Through the implementation of an optimized  $\text{MgF}_2$  layer, a conversion efficiency increase of 1% can be obtained.<sup>[113]</sup> However, the interference-type ARC is only effective in a narrow-wavelength value range. Furthermore, it only performs optimally for certain incident light angles, close to normal incidence.<sup>[93,97,114–116]</sup> Hence, these ARCs are mostly for laboratory best cell applications, and industrial solutions are the research topics of several complementary works.<sup>[42,117,118]</sup>

### 3.1.2. Microscale Texturization

Microscale textures enable an improved and broadband AR effect, stemming from multiple interactions with the rough surface before being reflected.<sup>[93,119]</sup> Following ray optics, **Figure 5a** schematically represents the light interaction with a micropylamid array (MPA) textured surface. When the incident light (ray 1) impinges onto the surface, a portion will be transmitted and a portion may be reflected onto another pyramid surface (ray 2), which in turn will be partly transmitted (ray 3) and reflected, with the possibility to reach another surface feature. An in-depth optical behavior analysis of the MPA architecture is performed by Baker-Finch et al.<sup>[120]</sup> Geometrical principles were used to determine the fractions of light submitted to consecutive bounces at the pyramid facets, having reached a value of 89% for two and 11% for three bounces.<sup>[120]</sup> It is these multiple interactions that increase the probability of light incoupling into the solar cell,

allowing for a reduced reflection independently of the incident angle.<sup>[119]</sup> The MPA may be optimized, such that reflected light from the rear surface impinges the front surface with an angle higher than its critical value, enabling total internal reflection (Figure 5a—ray 4).<sup>[93]</sup> Furthermore, the microscale features promote large-angle light refraction, as opposed to a flat surface, enabling a prolonged optical path length.<sup>[93,119,121]</sup> When integrated in a solar cell device with an ideal rear reflector, random microtextures promote an increased number of light surface interactions and allow for a  $4n^2$  enhancement of the optical path length.<sup>[122]</sup> Nonetheless, by comparison, modeling optimization of periodic architectures remains a simpler task than for random architectures, as these increase the modeling complexity.<sup>[120]</sup>

In CIGS solar cells, only few studies report the incorporation of microscale texturization for the reflectance broadband minimization.<sup>[119,123,124]</sup> The architecture choice has been either a periodic or random micropylamid texture, implemented in polymeric encapsulation layers. Those layers allow for improved solar cell long-term stability and are compatible with industry-friendly soft lithography processes.<sup>[124]</sup> Furthermore, applying texturization schemes to the encapsulation layer leaves the solar cell structure unchanged, avoiding charge dynamic-related problems.<sup>[119,124]</sup> In the case of a periodic approach, the light management performance is very dependent on the array architecture, the height-to-length aspect ratio being of critical importance.<sup>[93,119,125,126]</sup> Dottermusch et al. compared three CIGS solar

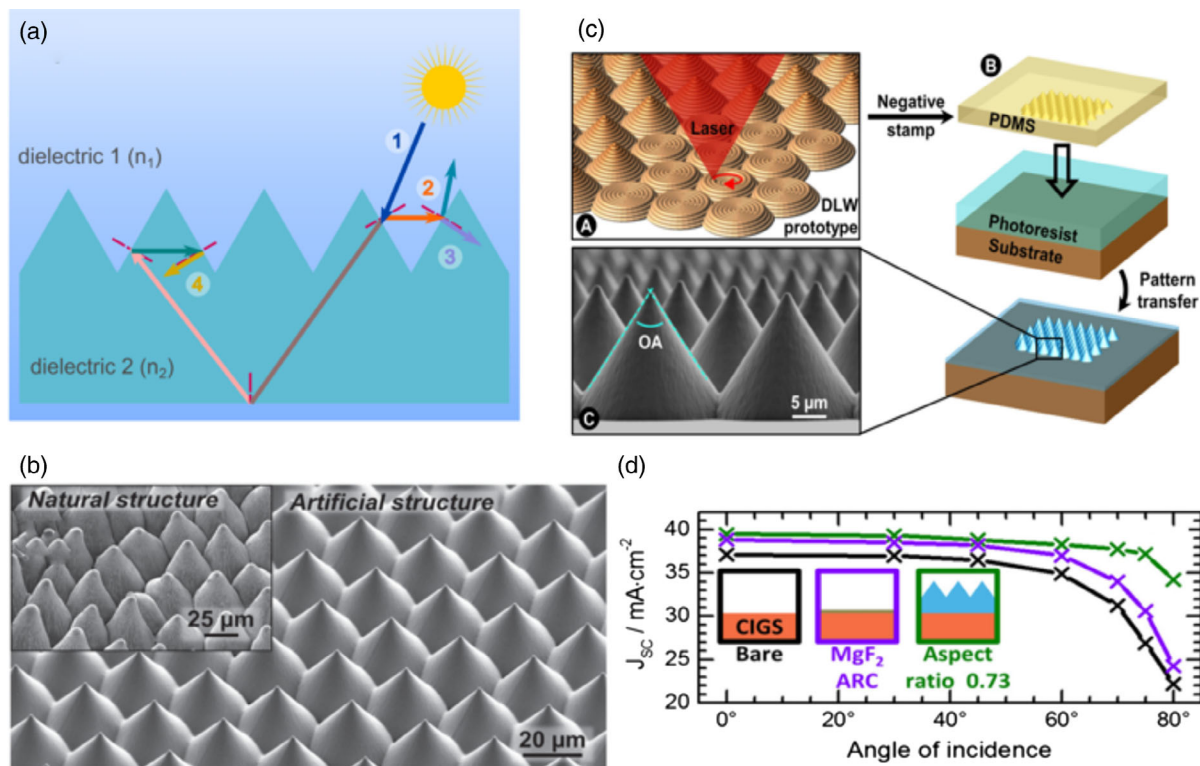


**Figure 5.** a) Schematic depiction considering ray optics of light ray interaction with MPA. b) Scanning electron microscope (SEM) image of the fabricated MPA. In the inset the replicated natural textures found in viola flowers are shown. Reproduced with permission.<sup>[119]</sup> Copyright 2019, Wiley-VCH; c) Schematic illustration of the MPA fabrication procedure: A) direct write laser (DWL) master mold fabrication. B) Texture replication on an UV-curable photoresist through a PDMS stamp. C) Cross-section SEM image of the MPA. Reproduced with permission.<sup>[119]</sup> Copyright 2019, Wiley-VCH; d) Measured  $J_{sc}$  in the bare,  $\text{MgF}_2$ , and micropylamid devices as a function of the incident angle. Reproduced with permission.<sup>[119]</sup> Copyright 2019, Wiley-VCH.

cell architectures to demonstrate the benefits of an MPA texturization AR approach.<sup>[119]</sup> a) bare, a typical CIGS device without any AR strategy; b) MgF<sub>2</sub>, where a single MgF<sub>2</sub> layer on top of the bare device is used; and c) micropyramid, a resist layer patterned with an MPA with a pitch of 25 μm was used as an encapsulation layer on top of the bare device (Figure 5b).

Optical simulations based on ray tracing were first performed to optimize the MPA, resulting in an aspect ratio of 0.73, to attain minimal reflection losses. The array was developed through a soft lithography technique via a PDMS stamp, as shown in Figure 5c. The MPA architecture enabled a 2 mA cm<sup>-2</sup> enhancement of the  $J_{sc}$  value for normal incidence, which led to a 3.5% relative increase in the power conversion efficiency value over the bare device. Such improvement was attributed to a minimization of the average reflectance value, being below 1% between 400 and 1100 nm. The three devices' dependence of the  $J_{sc}$  value on the incident angle is shown in Figure 5d. The Micropyramid performance was generally preserved under tilted illumination conditions. However, in the bare and MgF<sub>2</sub> planar-configuration devices, a large drop in the  $J_{sc}$  value is observed at incidence angles higher than 60°.

An additional effect inherent to the micrometer-large surface features is the ability to increase the optical path length through light refraction in the tapered structures. Therefore, the optical gains resultant from a reflectance decrease, or due to a prolonged optical path stemming from large refraction angles, must be decoupled. Čampa et al. used the 1D SunShine optical software, which is based on a semicoherent model that combines scalar scattering theory and ray tracing with wave optical models, to study the optical performance of a 360 nm CIGS device with a texturized front surface.<sup>[83]</sup> An optical analysis decoupling the two effects, AR and light scattering, arising from the textured front surface, was performed. Through the modeling of the texturized CIGS device, with a root mean square roughness value of 100 nm, a broadband improvement of the external quantum efficiency (EQE) spectrum only considering the AR effect was obtained, in comparison with a flat ultrathin device without any AR strategy.<sup>[83]</sup> Furthermore, the authors demonstrated that when only scattering from the textured surface is considered, this effect is even detrimental, due to the promoted long optical path length inside the solar cell top inactive media, which will lead to increased parasitic absorption. In addition, according to Snell's law, large refraction angles will be significantly reduced when light enters the high  $n$  medium. Thus, rays will not propagate into large refraction angles in the CIGS absorber. Hence, the improved optical performance of a CIGS device with a textured surface stems mostly from the AR effect. Krč et al. used the same software to quantify the  $J_{sc}$  gains attained by applying scattering at each CIGS solar cell interface.<sup>[42]</sup> In this study, ideal scattering surfaces with haze equal to unity were considered. The studied solar cells encompassed a glass encapsulation layer and have the following architecture: rear contact/300 nm CIGS/CdS/AZO/glass. From the simulated architectures, it was shown that applying scattering directly at each of the CIGS surfaces is the most favorable approach, as the  $J_{sc}$  value improvement exceeds 17% when each interface is considered, in comparison with the low enhancement (<8%) obtained when scattering is implemented either in the glass/air or CdS/AZO interfaces. Such discrepancy is a result of increased parasitic absorption in the

optical window and buffer layers, unavoidable when longer optical path lengths are promoted from the top-most interfaces. Therefore, the guidelines provided by this work suggest that scattering structures should either be used at the CdS/CIGS interface or at the rear contact, or that the window layers' parasitic absorption has to be reduced. The CdS/CIGS interface is the most sensitive component of the solar cell architecture, as the p–n heterojunction is established here. Thus, any modifications applied to this interface will inevitably affect the solar cell optoelectronic performance.<sup>[42]</sup> Therefore, wavelength-independent scattering approaches should be carefully analyzed, before being integrated at the CIGS front surface, the implementation of optical path length enhancement strategies in the rear architecture being a safer choice.<sup>[42]</sup> Besides enabling an omnidirectional AR performance, MPA schemes have been optimized in CIGS solar cells to minimize metallic grid shading.<sup>[117,127]</sup> Through the refraction phenomenon, incident light can be deviated from its path, avoiding its interaction with the highly reflective metal grids.<sup>[117,127]</sup>

### 3.1.3. Resonant Architectures

Resonant architectures have the potential to promote a more efficient light incoupling and increased optical path length at specific wavelength values, when compared with the microscale approach. Here, configurations such as periodic gratings,<sup>[128–130]</sup> plasmonic NPs,<sup>[70,131–138]</sup> and dielectric nanostructures<sup>[70,139–141]</sup> are included. Morphology-dependent light scattering and/or localization can be achieved through schemes exploiting resonant photonic or plasmonic effects. Mesoscale periodic gratings can be used to increase the optical path length.<sup>[92]</sup> Diffracted light from the periodic arrays can be coupled to waveguide modes in the absorber layer, that is, light is trapped in the absorber through the phenomenon of total internal reflection. Such waveguide mode excitations give rise to optical path length enhancements higher than the Lambertian limit of  $4n^2$ , achieved through full light randomization.<sup>[142]</sup> However, the diffraction effects arising from the gratings will lead to the same parasitic absorption effect as the one arising from refracted light by microscale textures. Hence, there are very few reports on gratings implemented in CIGS solar cells, being mostly simulation studies.<sup>[128–130]</sup> Furthermore, the optical benefits achieved with these architectures are commonly attributed to an angle-independent AR effect from light interaction with subwavelength structures, rather than coupling with waveguide modes through diffraction effects.<sup>[128–130]</sup> AR benefits derived from light interaction with subwavelength structures will be explored in Section 3.1.4.

Wavelength-selective resonant architectures on the solar cell interfaces have been commonly integrated through metallic or dielectric NPs.<sup>[41,70,131–138,141]</sup> Plasmonic architectures present additional benefits, as compared with the typical periodic mesoscale gratings. The resonant optical behavior of metallic NPs is a result of the free-electron motion. As an NP is illuminated, the external electric field interacts with it and promotes the movement of conduction electrons, to the surface opposite to the electric field. Due to the confinement of the electrons in an NP, positive charges will be accumulated in the opposite NP surface, creating an electric dipole. An electric field in the interior of the



NP, counterbalancing the external electric field, is created and forces the electrons to return to the equilibrium position.<sup>[143]</sup> Thus, the displacement of electronic charges induces an oscillatory behavior similar to a linear oscillator. This collective movement of electrons in a metallic NP is denominated as localized surface plasmons (LSPs). The LSP allows for an amplification of the incident electromagnetic field, which is maximum at the LSP resonant frequencies (Mie resonances), leading to an increase in the NP absorption and scattering cross sections.<sup>[144]</sup> The Mie resonance depends on a plethora of parameters, such as the NPs' shape, size, dielectric medium, and composition, among others.<sup>[145]</sup> An improved solar cell optical performance can be attained from the following mechanisms:<sup>[146]</sup> near-field scattering, the NPs present an evanescent electromagnetic field localized in their vicinity, working as subwavelength antennas and enabling an absorption enhancement if they are close to the CIGS layer, as shown in **Figure 6a**,<sup>[146–148]</sup> and far-field scattering, which is related to electromagnetic waves generated at distances much larger than the incident wavelength value, represented in **Figure 6b**. Preferential forward scattering from the plasmonic nanostructures leads to a significant reflection reduction. Furthermore, the plasmonic nanostructures can rescatter the incident light over a broad angle range, allowing for total internal reflection.<sup>[41,146–148]</sup> A comprehensive review of the LSP concept, as well as the mathematic formalism to describe it, is given in the study by Garcia et al.<sup>[143]</sup>

Despite the expected benefits, several conceptual and architectural constraints have to be overcome to attain an increased optical performance with metallic NPs. Reflection losses can never be completely suppressed.<sup>[70,149,150]</sup> In the light regime of out-of-resonance wavelength values, the highly reflective metallic structures block the incoming light (shading effect), and at resonant wavelength values, a fraction of light is additionally backscattered.<sup>[41,70]</sup> Therefore, for the best AR performance, an optimal surface coverage is required. Jeng et al. deposited Ag and Au NPs on the top of CIGS solar cells, with an absorber thickness value of 1700 nm.<sup>[135]</sup> The plasmonic nanostructures with diameters larger than 100 nm were deposited by spin coating of colloidal solutions. The deposition procedure was optimized, such that surface coverages ranging from 1% to 40% were achieved. In the referred study, an increase in the solar cells  $J_{sc}$  value was only accomplished for low NP surface coverages

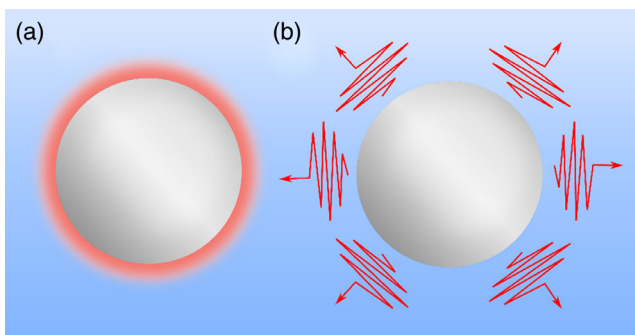


**Figure 6.** Schematic illustration of the effects resulting from plasmonic NPs interaction with light: a) near-field localization and b) far-field scattering.

(below 5%). A maximum conversion efficiency value relative increase of 1.1% was observed, compared with a solar cell device without NPs. The minor optical improvement was limited by shading effects from the metallic nanostructures, along with other aspects that prevent a full exploitation of the plasmonic configuration at the solar cell front surface. The near-field light localization has a nanometric evanescent decay. Therefore, the near field cannot be exploited in a configuration where the NPs are implemented on the topmost surface, as when inserted in a typical CIGS architecture, the NPs are separated from the absorber by thick multiple inactive layers with a total thickness of hundreds of nanometers.<sup>[70,148]</sup> Hence, the AR benefits that can be exploited from plasmonic NPs implemented on the front surface arise from far-field rescattered light, which allows for both better light incoupling and enhanced optical path length.<sup>[70]</sup> To fully exploit the NPs' near-field and far-field effects, these have additionally been implemented directly on top of the CIGS layer. When in direct contact with the absorber, near-field light localization effects can be exploited and large-angle far-field scattering will promote a longer optical path length inside the CIGS<sup>[41]</sup>. Chen et al. spray deposited 10 nm Au NPs at the CIGS/CdS interface.<sup>[133]</sup> The implementation of the Au NPs in direct contact with the absorber interface contributed to absolute augmentments of 10 mV and 3 mA cm<sup>-2</sup>, for  $V_{oc}$  and  $J_{sc}$ , respectively.<sup>[133]</sup> Optical simulations revealed a stronger field localization at the NP vicinity, indicating that the experimental improved figures of merit resulted from a near-field effect, due to strong absorption, as well as improved carrier extraction. Nonetheless, there is a fundamental limit on the plasmonic approach, as the metallic NPs present a large absorption cross section, leading to additional parasitic absorption.<sup>[70]</sup>

Absorption-free wavelength-scale dielectric structures have appeared as an alternative to avoid the issues arising from the inherent parasitic absorption of metallic NPs<sup>[70,140,142,151–157]</sup>. In an analogy to metallic NPs, dielectric structures can additionally be polarized upon light illumination and are able to support Mie resonances through the generation of electric dipoles, enabling for near-field and far-field effects. However, the dielectric polarization results from fixed charges; hence, it is not designated as plasmonic. Consequently, the polarizability of dielectric NPs is usually weaker than metallic ones. Therefore, for dielectric NPs to reach the same scattering performance as plasmonic ones, higher surface coverages and/or radii are required.<sup>[151]</sup> Besides electrical resonances, dielectric NPs offer the additional benefit of supporting magnetic dipole resonances, stemming from the coupling of the incident light to circular displacement currents of the electric field in the particle.<sup>[152]</sup> Magnetic and electric dipole resonances are usually of equal strength, and at resonant frequencies, the magnetic dipole resonances can provide a dominant contribution to the NP scattering cross section.<sup>[152]</sup> Furthermore, dielectric structures support whispering gallery modes that have been explored to significantly enhance the absorption in solar cells.<sup>[70,153,157]</sup> The dielectric structures work as optical cavities, by trapping light through total internal reflection. The electromagnetic field will then preferentially leak to the layers below, with a higher  $n$  compared to air. A detailed review of the optical behavior of dielectric NPs can be found in other studies.<sup>[70,152]</sup>

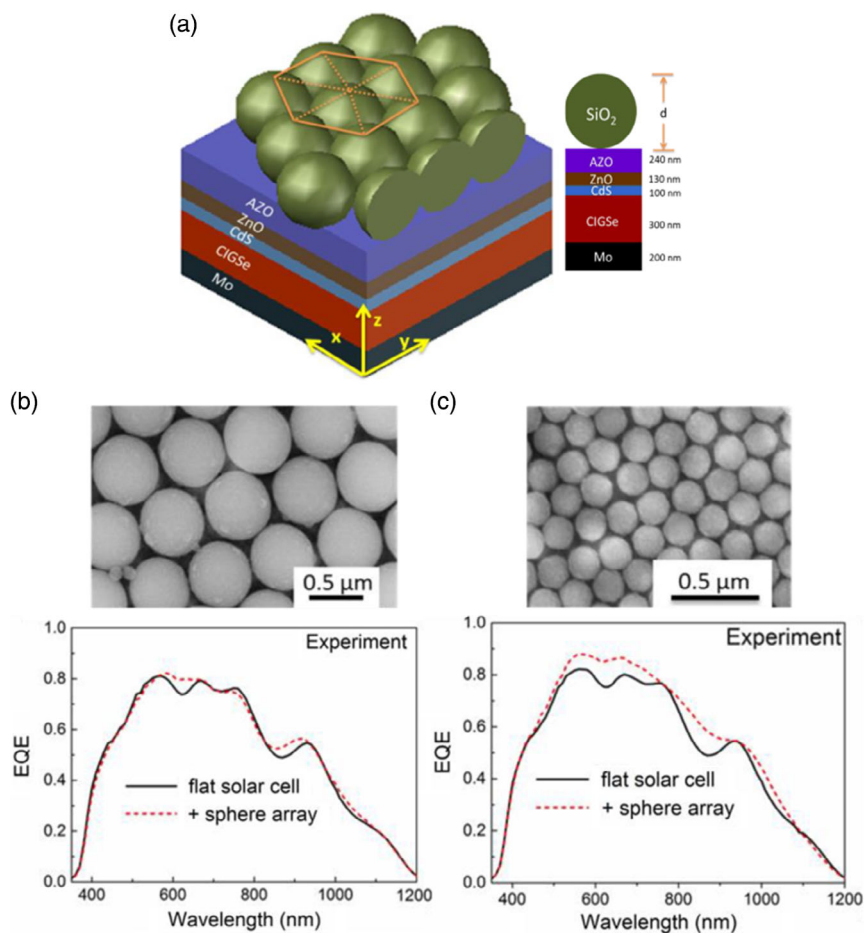


**Figure 7.** a) Schematic illustration of the ultrathin CIGS device with SiO<sub>2</sub> wavelength-scale spheres. b) SEM image of the deposited 600 nm sphere array and EQE of the solar cell with 600 nm spheres in comparison with a flat reference. c) SEM image of the deposited 120 nm sphere array and EQE of the solar cell with 120 nm spheres in comparison with a flat reference. Reproduced with permission.<sup>[157]</sup> Copyright 2016, Elsevier Inc.

The Langmuir–Blodgett method was used by Yin et al. to deposit SiO<sub>2</sub> spheres with diameters of 600 and 120 nm on a 300 nm CIGS-based solar cell, according to the architecture depicted in **Figure 7a**.<sup>[157]</sup> The solar cell with 600 nm spheres obtained a 0.4 mA cm<sup>-2</sup> increase of the *J*<sub>sc</sub> value in comparison with a flat reference without any AR strategy. The achieved improvement is shown in the region around 600–700 nm of the EQE spectrum, **Figure 7b**, attributed to the whispering gallery mode absorption enhancement in that wavelength range. Near-field enhancement from Mie resonances did not contribute to a significant absorption increase with the presented architecture, as the dipole moment is attenuated from a large distance between the air-front surface and the CIGS layer. Moreover, higher-order resonant modes are in the wavelength range where parasitic absorption in the CdS/ZnO/AZO stack is predominant (<550 nm). A better optoelectronic performance was achieved when using SiO<sub>2</sub> spheres with 120 nm. A broadband enhancement in the EQE spectrum in comparison with the one from the flat reference without dielectric spheres is shown in **Figure 7c**, which led to *J*<sub>sc</sub> enhancement of 1.6 mA cm<sup>-2</sup>. The improved optical performance observed for the implemented 120 nm spheres over the larger-diameter counterparts was

attributed to an enhanced AR performance. Light interacts with the subwavelength dielectric nanostructures as if it was a characteristic single layer characterized by an *n* value obtained through the volume fraction of SiO<sub>2</sub> spheres/air. The estimated effective *n* value of the characteristic layer was 1.3, which is close to the desired 1.38 value. The enhanced performance of the nanoscale structures serves as an introduction for Section 3.1.4, where an improved broadband and angular-independent AR effect through the use of grading-type architectures is evaluated and discussed.

### 3.1.4. Nano-Scale Texturization

Enhanced parasitic absorption issues arising from light scattering can be overcome by considering a grading AR strategy, which enables a broadband angle-independent AR. In the grading approach, a decreased reflection is achieved by a gradual change in the *n* value down to the absorber layer. Such a concept follows the Rayleigh effect principle, well detailed in other studies,<sup>[95,158]</sup> whereby the incident light ray will continuously bend inward, while traveling in a medium with a gradual increase in the *n*

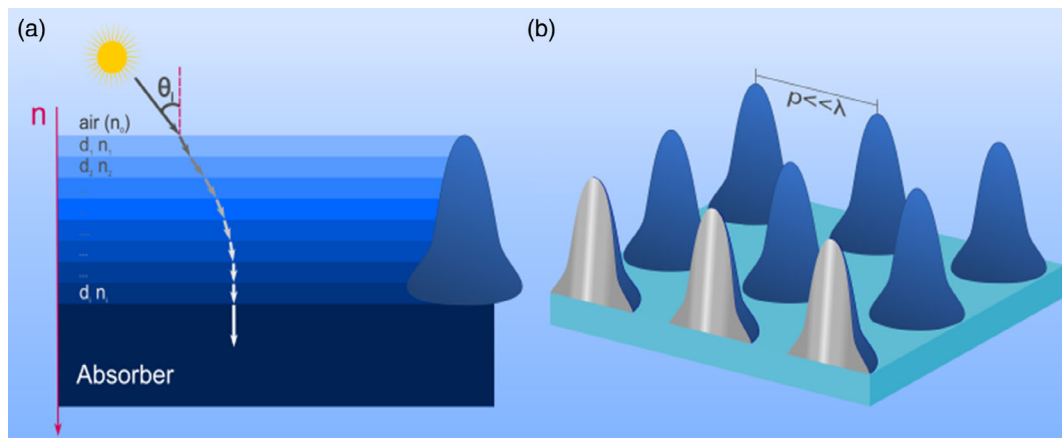


**Figure 8.** a) Schematic depiction considering ray optics of the Rayleigh effect, which describes light interaction upon a continuous gradient of increasing  $n$ . b) Schematic illustration of the moth-eye architecture, where the structure period ( $p$ ) is smaller than the incoming light wavelength.

value, as represented in **Figure 8a**. An architecture with  $n$  gradient is perceived as a single nonuniform layer, blurring the interface between air and the solar cell. Accordingly, an almost complete suppression of the reflection—for all wavelength values, that is, broadband—can be achieved, by avoiding abrupt changes in the  $n$  value.<sup>[159–161]</sup>

To replicate a grading-type architecture, researchers have been inspired by patterns found in nature.<sup>[161]</sup> In the eyes and wings of certain moth species, subwavelength structured arrays of tapered pillars are present.<sup>[161]</sup> As opposed to the interaction of light with geometrical uniform microfeatures, where there would always be reflection and refraction phenomena, incident light wavefronts will behave differently to subwavelength features. Incident light will interact with the nanostructures as a single entity, once the incoming wavelength is larger than the surface features.<sup>[95]</sup> Light interaction with subwavelength features is described by the EMT. The EMT is a homogenization theory, which states that if the period-to-wavelength ratio of the surface texture tends to zero, that is, the wavelength is much larger than the period, the optical properties of the textured surface will be identical to a homogenized planar version.<sup>[162]</sup> According to the EMT, the nanostructured surface can be approximated by series of multilayers, in which the effective  $n$  depends on the volume fractions of the nanostructures.<sup>[162]</sup> The moth-eye architectures have a tapered profile, as illustrated in **Figure 8b**. As the fraction of air around the structures gradually decreases from the top down to the base, incident photons feel a grading  $n$  as the one represented in **Figure 8a**.<sup>[95,161,163,164]</sup>

Over the past years, several architectures (cones, domes, pillars, pyramids) have been used to mimic the moth-eye texture.<sup>[159]</sup> In a previous work,<sup>[43]</sup> optical simulations through the FDTD method were performed to study the effect of pyramidal array trenches on the AZO layer in ultrathin CIGS devices, as shown in **Figure 9a**. Two different pitch sizes of the modeled array were studied, 1000 and 50 nm. In a periodic grating with large structural features, incident light will be scattered into different diffraction orders, and an AR effect is achieved from multiple interactions of the incident rays with the tapered profile. However, with subwavelength features, photons interact with

the textured surface without significant scattering and reflection effects. These phenomena are shown when comparing the electric field profiles on the 500 nm CIGS layer of both the studied devices (**Figure 9b,c**), at an incident wavelength value of 1000 nm. In both profiles, interference effects resulting from light reflection at the Mo rear contact are present, which is typical in ultrathin layers. However, the electric field profile of the device with a 1000 nm pitch is molded by the diffraction on the large period grating at the top, while the profile in the device with a 50 nm pitch is similar to what is observed on a flat device, without any clear diffraction from the rough layer. The structure with nanoscale features demonstrated a broadband minimization of the solar cell reflectance in comparison with the large features one, resulting from a gradient  $n$  profile, as demonstrated in **Figure 9d**. Such AR improvement led to a broadband absorbance enhancement over the large-scale featured device. To perform numerical simulations and optimize the performance of different moth-eye-like architectures in CIGS solar cell devices, the RCWA method was used by Hwang et al.<sup>[71]</sup> The moth-eye texturization was applied onto the window and buffer layer of the solar cell with three different profiles, conic, quadratic, and parabolic, as represented in **Figure 9e**. For every configuration, a reflectance decrease was observed with an increase in the features' aspect ratio. The optimized conic configuration allowed for effective reflectance values as low as 1%. Furthermore, when comparing the simulated transmittance as a function of the incident angle from the devices with an optimized conic pattern, an MgF<sub>2</sub> single layer, and a bare surface, a more efficient light incoupling for any angle of incidence is obtained with the textured surface.

Various techniques have been used to fabricate periodic nanoscale arrays, such as electron beam,<sup>[165]</sup> nanoimprint,<sup>[166]</sup> colloidal,<sup>[167]</sup> and interference lithography processes.<sup>[168]</sup> Burghoorn et al. patterned a moth-eye architecture with an average height and pitch of 350 and 300 nm, respectively, on a resist layer on top of thin-film CIGS solar cell devices.<sup>[169]</sup> The developed texture enabled for  $\approx 8\%$  decrease of the device's average relative reflectance, which led to a 10.6% increase of the  $J_{sc}$  over a flat reference device, for an absorber thickness of 1000 nm.<sup>[169]</sup> Furthermore,

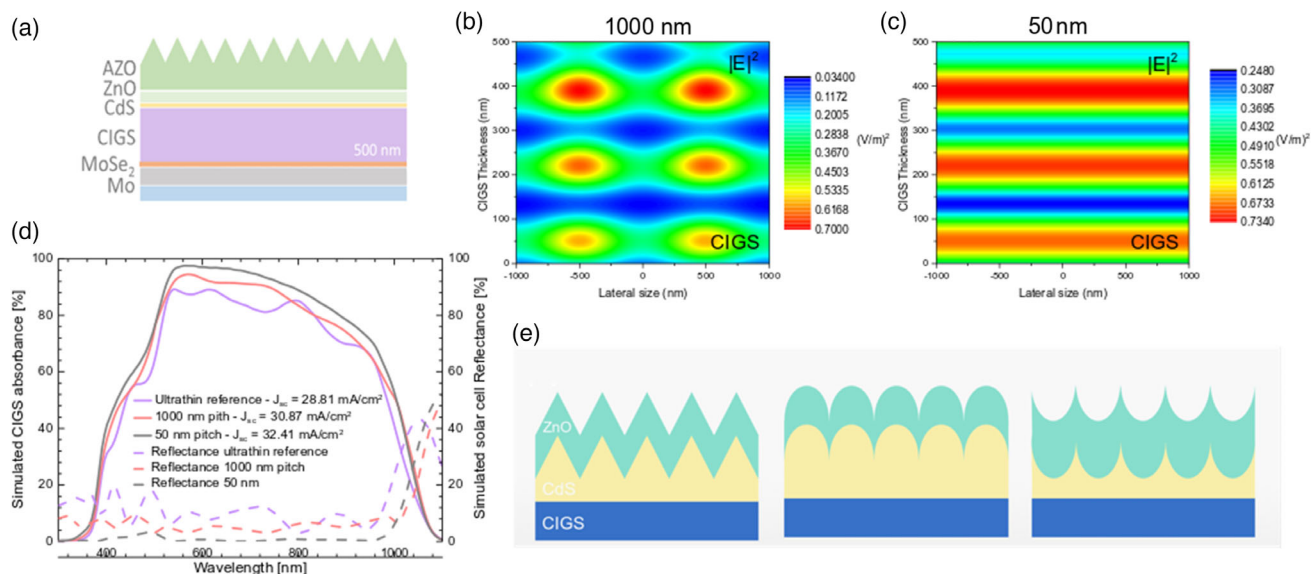


**Figure 9.** a) Studied architecture with the pyramid array. Electric field intensity in the absorber layer at an incident wavelength of 1000 nm, for: b) grating with a 1000 nm pitch and c) grating with 50 nm pitch. d) Simulated CIGS absorbance and total solar cell reflectance of an ultrathin flat reference and the aforementioned textured devices. Reproduced with permission.<sup>[43]</sup> Copyright 2021, SPIE. e) Schematic illustration of the pyramid, quadratic, and parabolic moth-eye profiles in the front layers of CIGS solar cells, studied by Hwang et al.<sup>[71]</sup>

different CIGS layer thicknesses (2000, 1000, and 850 nm) were employed and no trend toward a larger relative  $J_{sc}$  increase with decreasing CIGS thickness was observed. Hence, the optical performance improvement was attained mostly from the decreased AR effect and not due to an optical path length increase from diffraction effects in the subwavelength structures.

There is a high cost associated with a dense array of nanostructures over large areas. Therefore, surfaces with random subwavelength texturization have been explored to achieve the gradient effect, either through chemical methods to produce several nanomaterials or one-step wet-etching processes to promote anisotropic etching on the window layers.<sup>[98,116,170–173]</sup> Lai et al. used a chemical solution method to grow ZnO nanorods

on top of a CIGS device window layer.<sup>[172]</sup> The ZnO nanostructures were encapsulated with a PDMS layer, as demonstrated in **Figure 10a**. The PDMS layer was used to confer flexibility to the nanostructure array, as in previous studies, the rigidity of the nanostructures ensembles made them unsuitable for flexible PV applications.<sup>[172,174,175]</sup> Furthermore, the PDMS layer has  $n$  value in between the ones of AZO and air. Therefore, the  $n$  gradient provided by the PDMS-encapsulated ZnO nanostructures will be smoother as opposed to the case where the ZnO nanostructures were directly exposed to air. The  $n$  depth profiles along the top solar cell layers for the nanorod architectures, with and without the PDMS layer, are presented in Figure 10b,c. With the addition of the encapsulated nanorod architecture, a broadband

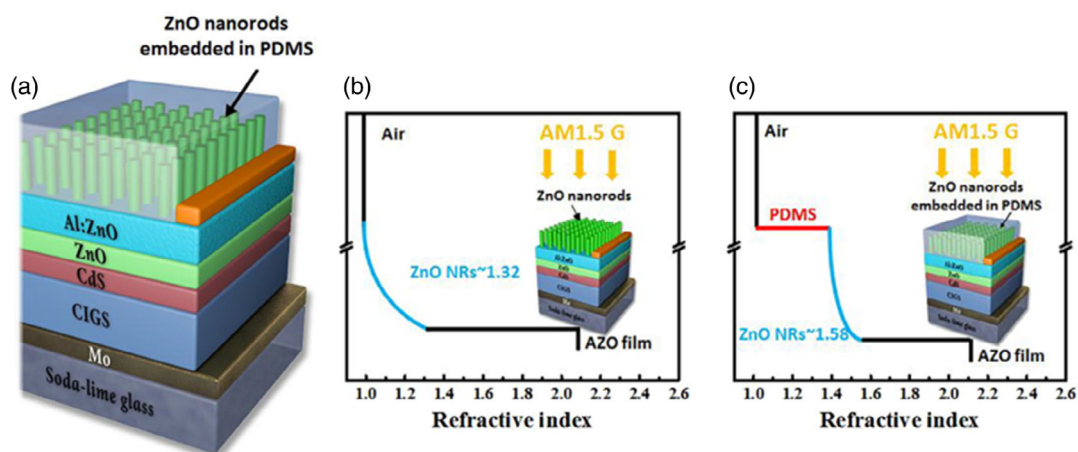


**Figure 10.** a) Schematic representation of the CIGS solar cell with ZnO nanorods embedded in a PDMS encapsulation layer. b) Schematic representation of the  $n$  profiles of b) only the ZnO nanorods architectures, and c) the architecture with ZnO nanorods embedded in PDMS. Reproduced with permission.<sup>[172]</sup> Copyright 2020, Wiley-VCH.

and omnidirectional decrease of the reflectance was achieved between the angles of incidence of  $-60^\circ$  and  $+60^\circ$ , in comparison with a planar device with only the PDMS layer.

A broad survey of the progress in light management schemes experimentally applied at the CIGS solar cell front layers through ARC, texturization, resonant, or nanoscale approaches is provided in **Table 1**. It is clear that nanotextured surfaces promote the highest  $J_{sc}$  enhancements among the AR strategies in CIGS solar cell devices.<sup>[115,176]</sup> Furthermore, the abundance of works regarding nanotextures corroborates the main conclusion from this section—at the CIGS solar cell front surface, an efficient omnidirectional AR without significant light scattering is required.

### 3.2. Rear Light Management Strategies

An extensive discussion of the light management schemes applied at the CIGS absorber rear to increase the optical path length, either through scattering or multireflection schemes (**Figure 11**), is performed. Hence, this section will start by reviewing the last advances that have been made to replace the Mo contact, by a configuration that provides more optical benefits. It is clear that the rear-contact replacement is a necessity. Nonetheless, other strategies have to be explored for ultrathin absorbers to reach the performance of their thicker counterparts. Hence, the schemes that have been applied to provide additional optical path enhancements, through scattering and/or coupling to waveguide modes, in ultrathin absorbers, are here detailed. Two main strategies have been explored, random microtexturization and resonant architectures, such as periodically spaced dielectric structures and metallic NPs.

#### 3.2.1. Rear-Contact Replacement

Conventionally, Mo is the material of choice to be used as a rear contact in CIGS devices.<sup>[11,31,177]</sup> The chemical and mechanical stability, low elemental diffusivity into the absorber film, and high melting point ( $\approx 2700^\circ\text{C}$ ) of Mo make it suitable to withstand the commonly harsh conditions during CIGS growth.<sup>[113,178,179]</sup> Although Mo does not react with copper (Cu), indium (In), or gallium (Ga), it reacts with Se to form molybdenum diselenide ( $\text{MoSe}_2$ ). The  $\text{MoSe}_2$  layer allows for a quasi-ohmic contact with CIGS<sup>[180,181]</sup>. However, Mo use is a tradeoff, as the low interface reflectivity ( $<20\%$ ) achieved with the Mo/ $\text{MoSe}_2$  and CIGS system compromises the optical path length enhancement.<sup>[42,181]</sup> Several approaches have been developed to replace the Mo rear contact by a more optically favorable configuration, ranging from 1) a direct metallic layer replacement;<sup>[179,182–186]</sup> 2) addition of a nanostructured reflective passivation layer;<sup>[36,187–190]</sup> 3) through the coupling of a metallic reflective layer with a point-contact passivation architecture;<sup>[191,192]</sup> or 4) different combinations of TCOs and metallic rear reflectors.<sup>[55,193–195]</sup> Nonetheless, this is not a simple task, as a great variety of requirements must be fulfilled to attain a viable rear contact, such as thermal, chemical, and mechanical stability, low interface recombination, and the ability to achieve an ohmic contact. For an optimized optical performance, ideally, Au, Ag, copper (Cu), or aluminum (Al) should be used as rear

reflectors, as they would allow for the highest rear-contact reflectance. However, the elemental diffusivity of these metals into the CIGS layer makes them unsuitable candidates.<sup>[184,196]</sup> Tungsten (W), niobium (Nb), tantalum (Ta), zirconium nitride (ZrN), and titanium nitride (TiN) have been identified as suitable replacements to the Mo rear contact.<sup>[185,186,197]</sup> Nevertheless, the achieved optical gains with these layers are usually counterbalanced by optoelectronic losses, associated with a higher contact resistivity and rear-contact recombination, when compared with Mo.<sup>[197]</sup> An academic approach for rear-contact replacement used a lift-off procedure to detach the Mo layer from the remaining CIGS cell, allowing for thermally evaporated Au layers to be deposited at the solar cell rear.<sup>[184]</sup> With an implemented Au reflective rear contact, only small variations on the  $J_{sc}$  value were obtained with a decrease in the absorber thickness. Nevertheless, this lift-off approach is limited to small areas, and the up-scale to industrial processes has not yet been demonstrated. Nanostructured dielectric layers can be used to passivate the rear interface and reduce recombination losses on ultrathin solar cell devices.<sup>[37]</sup> These stand-alone dielectric layers allow to boost the  $V_{oc}$  and  $J_{sc}$  values, as they enable for a carrier collection improvement, and increase reflectance when compared with the Mo/ $\text{MoSe}_2$  contact.<sup>[36,181,187–190,198–200]</sup> Lopes et al. went even further and used 18 nm nanopatterned aluminum oxide ( $\text{Al}_2\text{O}_3$ ) passivation layers, to encapsulate highly reflective metal layers in accordance with the schematic of **Figure 12**.<sup>[191]</sup> This architecture allows for both an interface passivation effect and enhanced optical reflection, enabling for an enhancement over the EQE of a reference device with a Mo layer. A 2.2% efficiency increase over a device with only the dielectric layer was achieved with a TiW reflector.<sup>[191]</sup> However, the developed architecture was not able to avoid unwanted diffusion of other tested metals, as the used lithographic procedure did not allow for encapsulating the metallic layer sidewalls.

In addition, attempts to integrate Ag mirrors have been done.<sup>[55,193]</sup> Nevertheless, when in direct contact with CIGS, Ag diffuses even at room temperature.<sup>[184]</sup> Thus, the main approach taken by many groups is to encapsulate the Ag mirror with TCOs. An effort has been made to use TCOs as rear contacts in CIGS solar cells, essentially through  $\text{SnO}_2\text{:F}$  (FTO),<sup>[90,91,124,195,201,202]</sup>  $\text{In}_2\text{O}_3\text{:Sn}$  (ITO),<sup>[91,123,194,201]</sup> or AZO.<sup>[55,91,195,203–206]</sup> Besides allowing to couple the rear contact with a highly reflective metal layer, the contact between TCO and CIGS can be exploited for other CIGS solar cell architectures, such as bifacial,<sup>[124,195,202]</sup> superstrate approaches<sup>[183,204–208]</sup> and multijunction devices with CIGS as a top cell.<sup>[90,91]</sup> Nevertheless, several issues have to be overcome for a viable TCO implementation. The metallic layer/TCO configuration blocks the sodium (Na) diffusion from the soda lime glass (SLG) to the CIGS, which is known to improve the optoelectronic properties, leading to an  $V_{oc}$  and conversion efficiency values' improvement.<sup>[20,178,209]</sup> Nonetheless, the Na absence can be surpassed by performing alkali PDT, which has been commonly used in high-efficiency devices.<sup>[20,31]</sup> Furthermore, a resistive gallium oxide ( $\text{Ga}_2\text{O}_3$ ) interface layer has been reported after CIGS growth at high temperatures on top of the TCOs<sup>[55,194,201]</sup>. As a result, the CIGS growth on TCOs is normally carried out at lower temperatures, which has an effect on the CIGS layer compositional gradient and grain size, hampering the performance of

**Table 1.** General overview of light management schemes comprising AR coatings, texturization, and resonant schemes, experimentally applied at the front layers of CIGS solar cells. The strategy, architecture, CIGS thickness,  $J_{sc}$ , and power conversion efficiency value ( $\eta$ ), as well as the relative increase in the  $J_{sc}$  and  $\eta$  values with respect to reference architectures, are listed.

Work	Strategy	Architecture	CIGS [ $\mu\text{m}$ ]	$J_{sc}$ [ $\text{mA cm}^{-2}$ ]	Relative $J_{sc}$ increase	$\eta$ [%]	Relative $\eta$ increase	Comment
Interference-type AR								
[96]	Single layer	• <sup>a)</sup>	–	31.5	–	8.5	–	–
		•/Teflon AF	–	32.7	↑ 3.8%	8.7	↑ 2.4%	105 nm-thick Teflon
[99]	Single layer	Thin-film CIGS solar cell	Thin	33.9	–	14.6	–	–
		Thin-film CIGS solar cell/MgF <sub>2</sub>	Thin	36.1	↑ 6.5%	15.5	↑ 6.2%	114 nm-thick MgF <sub>2</sub>
[108]	Single layer	•	2	35.6	–	16.7	–	–
		•/MgF <sub>2</sub>	2	37.5	↑ 5.3%	17.6	↑ 5.4%	MgF <sub>2</sub> layer thickness optimized for minimum reflectance at 500 nm
[274]	Multilayer	•	1	30.6	–	–	–	–
		•/2× (HfO/MgF <sub>2</sub> )	1	32.0	↑ 4.6%	–	–	Multilayer AR with high-/low-index profile
		•	0.6	27.5	–	–	–	–
		•/2× (HfO/MgF <sub>2</sub> )	0.6	29.8	↑ 8.4%	–	–	Multilayer AR with high-/low-index profile
Microscale texturization								
[123]	Random microtexturization	•	2	22.1	–	9.4	–	–
		•/Textured PDMS	2	23.9	↑ 8.1%	10.2	↑ 8.5%	Texturization Height: 2.5 $\mu\text{m}$
[124]	Random microtexturization	In <sub>2</sub> O <sub>3</sub> :Sn/CIGS/CdS/i-ZnO/ In <sub>2</sub> O <sub>3</sub> :Sn	0.32	19.0	–	9.0	–	–
		In <sub>2</sub> O <sub>3</sub> :Sn/CIGS/CdS/i-ZnO/ In <sub>2</sub> O <sub>3</sub> :Sn/textured PDMS	0.32	21.0	↑ 10.5%	10.5	↑ 16.7%	–
[275]	Microtexturization	–/Mo/CIGS/CdS/i-ZnO/ITO	2	23.6	–	9.6	–	–
		–/Mo/textured CIGS/CdS/ i-ZnO/ITO	2	24.5	↑ 3.8%	10.5	↑ 9.4%	Microhole array Height: 184.5 nm; Diameter: 4000 nm; Pitch: 5000 nm
		–/Mo/textured CIGS/CdS/ i-ZnO/ITO	2	25.7	↑ 8.9%	11.2	↑ 16.7%	Microdome array Height: 854.7 nm; Diameter: 2500 nm; Pitch: 5000 nm
[119]	Microtexturization	•	2.5–3.0	39.2	–	20.2	–	–
		•/NOA 88 based MPA	2.5–3.0	41.2	↑ 5.1%	20.9	↑ 3.5%	Aspect Ratio: 0.73 Height: 18.25 $\mu\text{m}$ Pitch: 25 $\mu\text{m}$
[127]	Microtexturization	▲ <sup>b)</sup>	2	28.0	–	9.7	–	–
		▲/NiAl/PDMS with MPA	2	29.4	↑ 5.0%	10.2	↑ 5.2%	MPA on the grid Height: 13.4 $\mu\text{m}$ Width: 21 $\mu\text{m}$
Resonant architectures								
[131]	NPs	•	2.3	34.0	–	16.5	–	–
		•/Ag NPs in Al <sub>2</sub> O <sub>3</sub>	2.3	33.1	↓ 2.6%	15.9	↓ 3.6%	Ag NPs: 4 nm
[133]	NPs	▲	Thin	34.8	–	8.3	–	–
		SS/Mo/CIGS/Au NPs/CdS/ i-ZnO/AZO	Thin	37.8	↑ 8.6%	10.4	↑ 25.3%	Au NPs: 10 nm

**Table 1.** Continued.

Work	Strategy	Architecture	CIGS [ $\mu\text{m}$ ]	$J_{sc}$ [ $\text{mA cm}^{-2}$ ]	Relative $J_{sc}$ increase	$\eta$ [%]	Relative $\eta$ increase	Comment
[135]	NPs	•	1.7	24.3	–	10.2	–	–
		•/Au NPs	1.7	25.4	↑ 4.5%	10.3	↑ 1.0%	Au NPs: 100 nm 1% surface coverage
		•	1.7	28.1	–	9.31	–	–
		•/Ag NPs	1.7	29.8	↑ 6.0%	9.44	↑ 1.1%	Ag NPs: 100 nm 5% surface coverage
[216]	Dielectric structures	•	0.46	28.6	–	10.1	–	–
		•/Textured $\text{TiO}_2$	0.46	29.8	↑ 4.2%	10.9	↑ 7.9%	Periodic dielectric structures Height: 120 nm Width: 120 nm Pitch: 500 nm
Nanoscale texturization								
[276]	Random Nanotexturization	SLG/Mo/CIGS/(Zn,Mg)O/ ZnO:Al	thin	35.8	–	15.8	–	–
		SLG/Mo/CIGS/(Zn,Mg)O/ ZnO:Al/ ZnO nanorods	thin	37.9	↑ 5.9%	16.6	↑ 5.1%	ZnO nanorods Height: 450 nm Diameter: 80 nm
[176]	Random Nanotexturization	•	1.7	30.1	–	10.0	–	–
		•/ZnO nanorods	1.7	35.0	↑ 16.3%	11.5	↑ 15.0%	Conic ZnO nanorods Height: 400 nm Diameter: 200 nm
		•/ZnO nanorods	1.7	33.7	↑ 12.0%	10.9	↑ 9.0%	Flat ZnO nanorods Height: 400 nm Diameter: 200 nm
[97]	Random nanotexturization	•	2	30.9	–	10.4	–	–
		•/Textured ZnO	2	33.8	↑ 9.4%	10.5	↑ 1.0%	870 nm-thick ZnO (before etch)
[115]	Random nanotexturization	•	1.5	22.7	–	9.1	–	–
		•/ZnO nanorods	1.5	29.5	↑ 30.0%	11.1	↑ 22.0%	ZnO nanorods Diameter: 15 nm
[160]	Random Nanotexturization	•	2	36.3	–	16.9	–	–
		•/SiO <sub>2</sub> Nps	2	38.1	↑ 5.0%	17.2	↑ 1.8%	SiO <sub>2</sub> NPs: 20–30 nm
[277]	Random Nanotexturization	•	–	–	–	10.3	–	–
		•/SiO <sub>2</sub> –PEG	–	–	–	11.1	↑ 7.8%	Nanopores Diameter: 50–200 nm
		•	–	–	–	10.2	–	–
[116]	Random Nanotexturization	•	2	–	–	10.4	–	–
		•/Textured ZnO/MgF <sub>2</sub>	2	–	↑	11.0	↑ 5.8%	Texturization Height < 350 nm 100 nm-thick MgF <sub>2</sub>
[157]	Random Nanotexturization	•	0.3	24.2	–	9.0	–	–
		•/SiO <sub>2</sub> spheres	0.3	25.8	↑ 6.6%	9.7	↑ 7.8%	SiO <sub>2</sub> spheres: 120 nm
		•	0.3	24.2	–	9.1	–	–
		•/SiO <sub>2</sub> spheres	0.3	24.6	↑ 1.7%	9.2	↑ 1.1%	SiO <sub>2</sub> spheres: 600 nm

**Table 1.** Continued.

Work	Strategy	Architecture	CIGS [ $\mu\text{m}$ ]	$J_{sc}$ [ $\text{mA cm}^{-2}$ ]	Relative $J_{sc}$ increase	$\eta$ [%]	Relative $\eta$ increase	Comment
[171]	Random Nanotexturization	■ <sup>c)</sup> /MgZnO:Ga	Thin	27.1	–	9.2	–	–
		■/MgZnO:Ga/ ZnO nanorods	Thin	29.9	↑ 10.3%	9.9	↑ 7.6%	ZnO nanorods Height: 100 nm
		■/MgZnO:Ga/MgF <sub>2</sub>	Thin	30.9	–	10.2	–	100 nm MgF <sub>2</sub> thick
		■/MgZnO:Ga/ ZnO nanorods/MgF <sub>2</sub>	Thin	32.3	↑ 4.5%	10.8	↑ 5.9%	ZnO nanorods Height: 100 nm 100 nm MgF <sub>2</sub> thick
[136]	Random Nanotexturization	■/i-ZnO/ITO	Thin	36.1	–	10.2	–	–
		■/i-ZnO/ Ag nanowires and Au NPs	Thin	37.5	↑ 3.9%	10.3	↑ 1.0%	Ag nanowires Diameter: 120–150 nm Au NPs: 70–90 nm
[117]	Random Nanotexturization	•/NiAl	2	34.5	–	14.1	–	–
		•/NiAl/NOA 164/Glass MPA and randomly textured	2	37.6	↑ 9.0%	15.3	↑ 8.5%	MPA on the grid Height: 6.2 $\mu\text{m}$ Width: 20 $\mu\text{m}$
[118]	Random Nanotexturization	•	2	36.6	–	15.0	–	–
		•/Borosilicate glass textured	2	38.2	↑ 4.4%	15.9	↑ 6.0%	Cone-shape subwavelength structures
[278]	Random Nanotexturization	•	2.5–3.0	–	–	–	–	–
		•/MgF <sub>2</sub>	2.5–3.0	–	↑ 6.3% <sup>d)</sup>	–	↑ 7.2%	105 nm-thick MgF <sub>2</sub>
		•/Textured PMMA	2.5–3.0	–	↑ 6.5% <sup>d)</sup>	–	↑ 6.6%	biomimetic rose petals
[172]	Random Nanotexturization	•	2	18.3	–	7.2	–	–
		•/PDMS	2	19.0	↑ 3.8%	7.5	↑ 4.2%	70 $\mu\text{m}$ -thick PDMS
		•/ZnO nanorods	2	19.3	↑ 5.5%	7.6	↑ 5.6%	ZnO nanorods Diameter: 70–100 nm Height: 1500 nm
		•/PDMS/ZnO nanorods	2	19.8	↑ 8.2%	7.8	↑ 8.3%	70 $\mu\text{m}$ -thick PDMS ZnO nanorods Diameter: 70–100 nm Height: 1500 nm
[169]	Nanotexturization	•/	0.85	22.4	–	10.5	–	–
		•/Textured Kriya SPF1439-a3	0.85	24.5	↑ 9.4%	10.9	↑ 3.8%	Textured Kriya SPF1439-a3- Pitch: 300 nm Height: 350 nm
		•/	1	25.4	–	11.0	–	–
		•/Textured Kriya SPF1439-a3	1	28.1	↑ 10.6%	11.9	↑ 8.2%	Textured Kriya SPF1439-a3- Pitch: 300 nm Height: 350 nm
		•/	2	31.9	–	14.7	–	–
		•/Textured Kriya SPF1439-a3	2	33.3	↑ 4.4%	15.5	↑ 5.4%	Textured Kriya SPF1439-a3- Pitch: 300 nm Height: 350 nm
[167]	Nanotexturization	•	2	29.9	–	10.3	–	–
		•/Textured ZnO	2	32.6	↑ 9.0%	11.4	↑ 10.7%	Honeycomb-like cavities

<sup>a)</sup>• stands for SLG/Mo/CIGS/CdS/i-ZnO/AZO; <sup>b)</sup>▲ stands for stainless steel (SS)/Mo/CIGS/CdS/i-ZnO/AZO; <sup>c)</sup>■ stands for SLG/Mo/CIGS/CdS; <sup>d)</sup>calculated from short circuit current ( $I_{sc}$ ) value.

the overall device.<sup>[55,59,194,210,211]</sup> Nevertheless, ACIGS solar cells have been successfully developed in SLG substrates under low temperatures, down to a nominal substrate temperature of

253 °C, albeit with a conversion efficiency value decrease as lower deposition temperatures are used.<sup>[67]</sup> Several works report an increased conversion efficiency when going from Mo to a



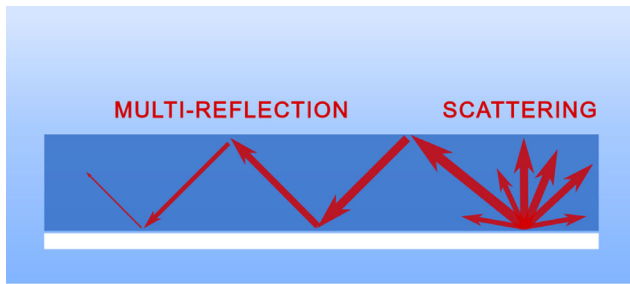


**Figure 11.** Schematic illustration of the light management mechanisms that can be used at the rear of CIGS solar cells: light trapping through multiple reflections at absorber interfaces and scattering for a prolonged optical path length.

mirror/TCO stack.<sup>[55,193–195]</sup> However, it is important to note that the CIGS deposition is changed from the state-of-the-art process to answer the TCO requirement. Hence, even with the optical path length enhancement, Mo is still the most suitable candidate. Currently, the world record for ultrathin devices is still held by a Mo-contacted solar cell, reaching a conversion efficiency of 15.2%.<sup>[34]</sup>

Considering the ideal perfect reflective mirror as the solar cell rear contact, it would be possible to double the optical path length in the absorber layer and significantly enhance the  $J_{sc}$  value.<sup>[42,43]</sup> To quantify the possible increase in the  $J_{sc}$  value, optical simulations were performed in three CIGS device architectures: 1) 500 nm CIGS with a typical Mo rear contact; 2) 500 nm CIGS with a perfect reflective interface; and 3) 2000 nm absorber with a typical Mo rear contact. The FDTD-simulated CIGS absorbance for the three studied devices is shown in **Figure 13**. Through the upgrade from a poor Mo reflector to a perfect reflective layer, a  $J_{sc}$  improvement of  $1.8 \text{ mA cm}^{-2}$  could be achieved, coming mostly from the reflection of the long-wavelength light. Even with a perfect reflector, there is still a  $J_{sc}$  value gap of  $2.1 \text{ mA cm}^{-2}$  to achieve the performance obtained for a 2000 nm absorber. A rear-contact replacement is needed to increase the optical path length. However, it is only a step toward a larger goal, as the obtained double-optical path length enhancement, achieved through a perfect reflector, is not able to tackle

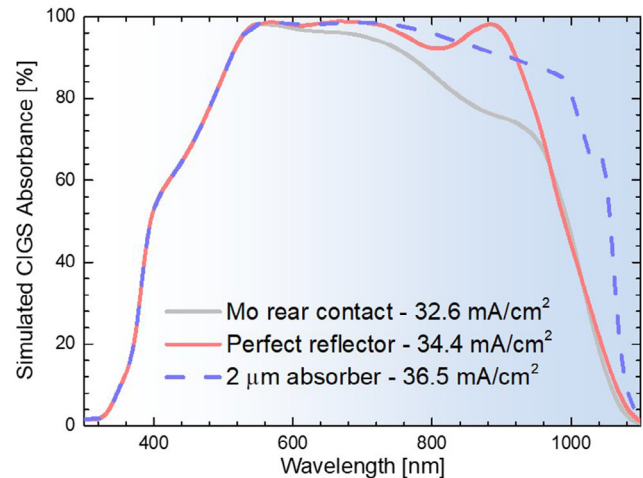


**Figure 13.** Simulated CIGS absorbance of the ultrathin 500 nm absorber with a typical Mo rear contact, or a perfect reflective interface, and a thin 2000 nm absorber with a typical Mo rear contact where the window layers are the same for all structures.

the gap that exists in the NIR range to the thin absorber. For that, scattering strategies are necessary to improve the light-trapping capabilities of an ultrathin solar cell.

### 3.2.2. Microscale Texturization

A great variety of works report on the optical benefits of a textured rear interface in CIGS devices through optical simulations.<sup>[42,212,213]</sup> Kovačič et al. applied an optical model to study different light management approaches to improve the performance of ultrathin CIGS devices.<sup>[213]</sup> Four different Mo surface textures were studied according to **Figure 14**, step 1: flat, sine-like, u-like, and negative u-like. The pitch and height of the textures were varied to find a geometry able to maximize the  $J_{sc}$  value. From the modeled architectures, a sine-like texture with a pitch of 800 nm and 300 nm height performed the best, leading to a  $1.1 \text{ mA cm}^{-2}$   $J_{sc}$  value increase with respect to the flat architecture. Next, an Ag/ $\text{Al}_2\text{O}_3$  stack was used on top of the textured Mo to improve the optical reflection of the rear contact, as

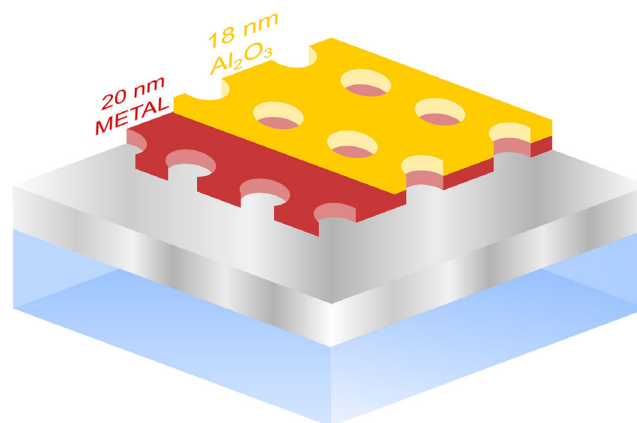


**Figure 12.** Schematic illustration of the fabricated ultrathin CIGS solar cell architecture, with nanostructured passivation layers used for the encapsulation of metallic layers.<sup>[191]</sup>

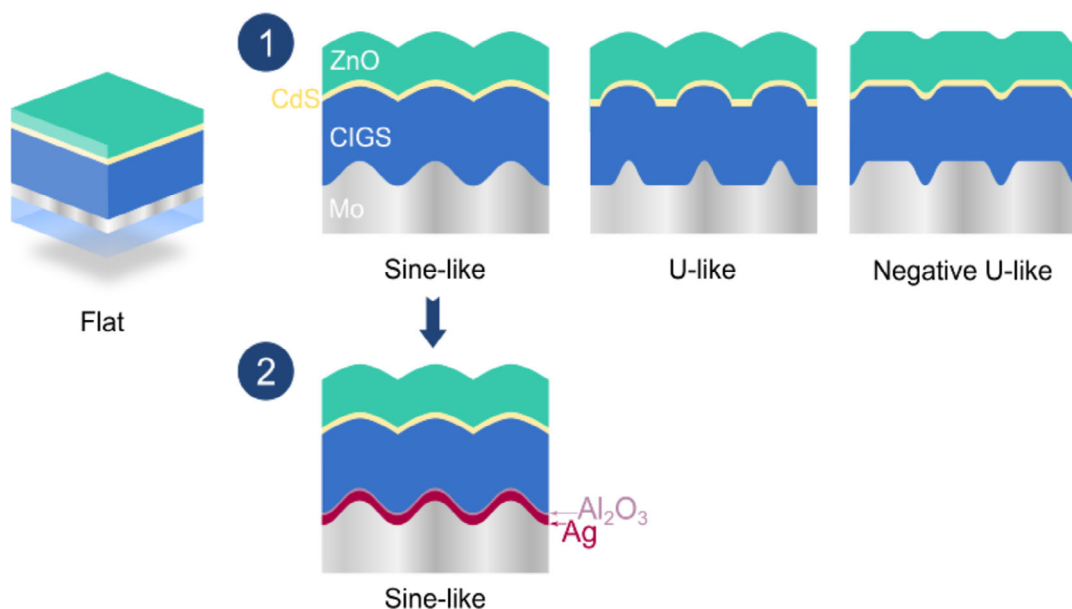


**Figure 14.** Schematic illustration of the flat, sine-like, u-like, and parabolic texture profiles studied by Kovacic et al.<sup>[213]</sup> Step 1 illustrates the solar cell architecture with the Mo layer in direct contact with the absorber, while in step 2 a rear reflector/Al<sub>2</sub>O<sub>3</sub> stack is added on top of Mo.

presented in Figure 14, step 2. By adding the reflective layer, the  $J_{sc}$  further increased by  $5.5 \text{ mA cm}^{-2}$ , compared with the former sine architecture. When the flat and sine-like architectures, both with a rear reflector (Ag/Al<sub>2</sub>O<sub>3</sub> stack), are compared, a relative  $J_{sc}$  increase of 12.6% is achieved, which is much higher than the 4.0% enhancement obtained when the same comparison is done without a rear reflector. This result demonstrates the importance of coupling a reflective mirror with light-trapping approaches, with the aim of exploiting the potential of the scattering surface to the fullest.<sup>[42,213]</sup> Despite the promising results obtained through optical modeling, the practical implementation of rear-contact texturing is limited by surface roughness.<sup>[214,215]</sup> In CIGS solar cell devices, the use of textured surfaces generally leads to a poor solar cell performance, originating from a drop of the fill factor (FF) often accompanied by  $V_{oc}$  losses.<sup>[65,124,214,215]</sup> To scatter light efficiently, the texturing dimensions must be at least in the order of the illuminating wavelength values. Such rough substrates challenge the desired conformal growth of the CIGS absorber, leading to a more defective rear interface and promoting the formation of pinholes.<sup>[65]</sup> Typically, texturing approaches lead to a great number of short-circuited solar cells, or even a poor CIGS adhesion to the substrate, completely ruining the PV device.<sup>[214,215]</sup> Furthermore, the growth over the rough substrate leads to a partial transfer of the texturization to all the solar cell layers, which implies an increased roughness that can result in a higher sheet resistance in the solar cell contact layers.<sup>[214]</sup>

### 3.2.3. Resonant Architectures

Significant conversion efficiency enhancements through textured rear surfaces have only been reported when resonant architectures, capable of exciting waveguide modes in the absorber, are applied.<sup>[141,216–218]</sup> Wang et al. developed a novel

architecture with periodic resonant cavities at the Mo rear contact.<sup>[218]</sup> Through optical simulations, resonant electric field enhancements in the NIR region that excite guided-mode resonances and contribute for a  $J_{sc}$  value improvement were observed. In addition, an Al<sub>2</sub>O<sub>3</sub> point-contact architecture developed through grazing-angle deposition, on the fabricated cavities, enabled to suppress the interface recombination losses by providing a passivation effect.<sup>[218]</sup> Periodic dielectric structures are used as a resonant architecture that, in resemblance to the dielectric NPs applied at the front contact, can support Mie and whispering gallery mode resonances.<sup>[70,153,157,219]</sup> The used dielectric materials must be thermally and electrically stable to survive the CIGS growth. SiO<sub>2</sub> satisfies the above requirements, thus being a common material choice. Several works have reported on the utilization of SiO<sub>2</sub> as a rear passivation layer, obtaining considerably high  $V_{oc}$  values in ultrathin devices without absorber bandgap gradients, from a reduction of the interface recombination rate.<sup>[36,38–40,220]</sup> Besides the expected optical benefit, an improved electrical performance can thus be expected with SiO<sub>2</sub> nanostructures at the rear contact in ultrathin solar cells.<sup>[217]</sup> However, a nanopatterned passivation layer can often lead to an FF value decrease, as a consequence of the reduced contact area, thickness of the dielectric passivation layer, and even an inhomogeneous alkali doping distribution in the absorber.<sup>[40,187,220]</sup> An array of SiO<sub>2</sub> nanostructures with a conical shape was fabricated by Yin et al. through substrate conformal imprint lithography.<sup>[217]</sup> The developed nanostructures presented a height of 210 nm and a pitch of 513 nm, as shown in Figure 15a. The developed solar cell architecture is shown in Figure 15b. The nanostructures were implemented on top of an ITO rear contact, and when coupled with a reflective rear mirror, a  $J_{sc}$  enhancement of  $6.9 \text{ mA cm}^{-2}$  was achieved over the reference planar device. The coupling with highly reflective layers allows for the light to be scattered back to the absorber

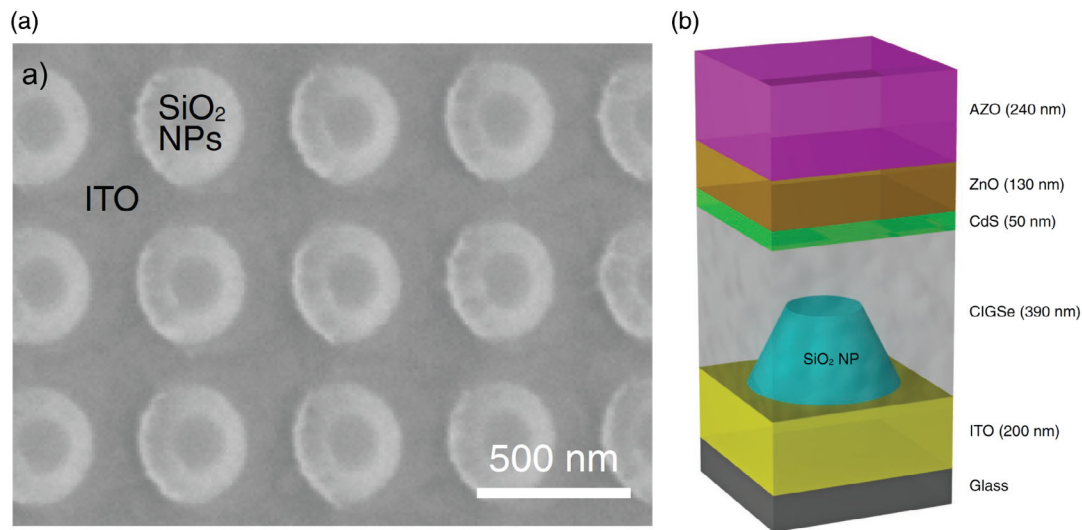


**Figure 15.** a) SEM top-view image of the fabricated SiO<sub>2</sub> dielectric structures array on the ITO rear contact. b) Schematic representation of the fabricated CIGS solar cell with the SiO<sub>2</sub> dielectric structures. Reproduced with permission.<sup>[217]</sup> Copyright 2017, Wiley-VCH.

either by direct interaction with the photonic structures or through reflection by the metallic mirror.<sup>[149,217]</sup> Most importantly, as opposed to the typical tendency verified with microtexturization, there was a  $V_{oc}$  improvement through the implementation of the SiO<sub>2</sub> cones. The  $V_{oc}$  increase is likely due to the interface passivation effect of SiO<sub>2</sub>.

A scattering approach using metallic nanostructures at the rear interface has been receiving attention. Schmid et al. used the FEM to predict the optimum size of metallic and dielectric NPs to promote absorbance enhancements in a CIGS layer.<sup>[70]</sup> While a maximum absorbance enhancement for Ag NPs is obtained with diameters around 100–150 nm, diameters above 200 nm are required for a beneficial optical effect to arise when dielectric NPs are integrated at the rear contact.<sup>[70]</sup> Thereafter, using metallic nanostructures can be beneficial as the harmful electrical degradation arising from a strong texturing can be minimized. Moreover, smaller structures are in principle more beneficial for module production, particularly in terms of interconnects incorporation. When integrated at the rear absorber interface, the metallic NPs only interact with the long-wavelength light and the resonant scattering wavelength values can be tuned to the NIR range by changing the NP size, shape, and dielectric medium.<sup>[43,70,146,149,221]</sup>

Vermang et al. exploited the resonant effects arising from Mo spheres in ultrathin CIGS-based devices.<sup>[189]</sup> Those 200 nm Mo spheres were directly implemented between the Mo rear contact and the CIGS absorber. The implementation of the nanostructures led to a 1.3 mA cm<sup>-2</sup> increase on the  $J_{sc}$  value, compared with a Mo-based contact, arising from an improved rear scattering combined with an AR effect promoted by the front-surface texturization. However, the solar cell performance was limited by a large  $V_{oc}$  value loss of 225 mV over a device without the spheres. The growth of the CIGS absorber on the Mo spheres increases the surface area and consequently the interface recombination. However, it was demonstrated that a combined rear passivation, through a dielectric layer and bandgap gradient,

allowed for a mitigation of the  $V_{oc}$  losses. Ultimately, the authors were able to obtain a small conversion efficiency value enhancement of 0.4%, through the implementation of Mo spheres coupled with a passivation strategy, compared with a reference device. Further improvements on the used light-trapping architecture are required, as Au or Ag NPs with smaller dimensions can provide a higher scattering performance, when compared with Mo spheres.<sup>[138,146,148,222]</sup> Nonetheless, Au and Ag will diffuse during the high-temperature absorber growth, if not properly encapsulated.<sup>[43,65,70,148,191]</sup> One of the proposed architectures uses a TCO rear contact to encapsulate the metallic NPs.<sup>[148,223,224]</sup> Schmid et al. demonstrated the stability of the architecture with a thick TCO layer encapsulating metallic NPs.<sup>[224]</sup> A substrate with Ag NPs encapsulated by a 100–200 nm ITO layer was proven to be able to withstand temperatures up to 630 °C, demonstrating the compatibility with the CIGS deposition process. However, the NP encapsulation with such thick TCO layers inhibits the effective coupling of the resonant modes with the absorber. In addition, parasitic absorption from the thick TCO might hamper the plasmonic enhancement.<sup>[70]</sup> Thus, a novel architecture involving the encapsulation of the nanostructures with a dielectric passivation layer was proposed.<sup>[43,65]</sup> A line contact architecture can be performed with the NPs placed on top of a Mo rear contact, only separated from the absorber by a thin passivation layer. A substrate combining light trapping through metallic NPs, and passivation through the dielectric layer with a line contact pattern, can thus be achieved. In a previous work, the effective encapsulation of Au NP aggregates with a 25 nm Al<sub>2</sub>O<sub>3</sub> layer in a complete CIGS device was demonstrated through an X-ray photoelectron spectroscopy depth analysis.<sup>[65]</sup> Here, micrometer-large Au aggregates were used instead of a plasmonic approach with individualized NPs, as the main goal was to establish a proof of concept for the encapsulation with a thin dielectric layer. The integration of the metallic aggregates led to an optical improvement that resulted in a  $J_{sc}$  value enhancement of 3.7 mA cm<sup>-2</sup>, originating

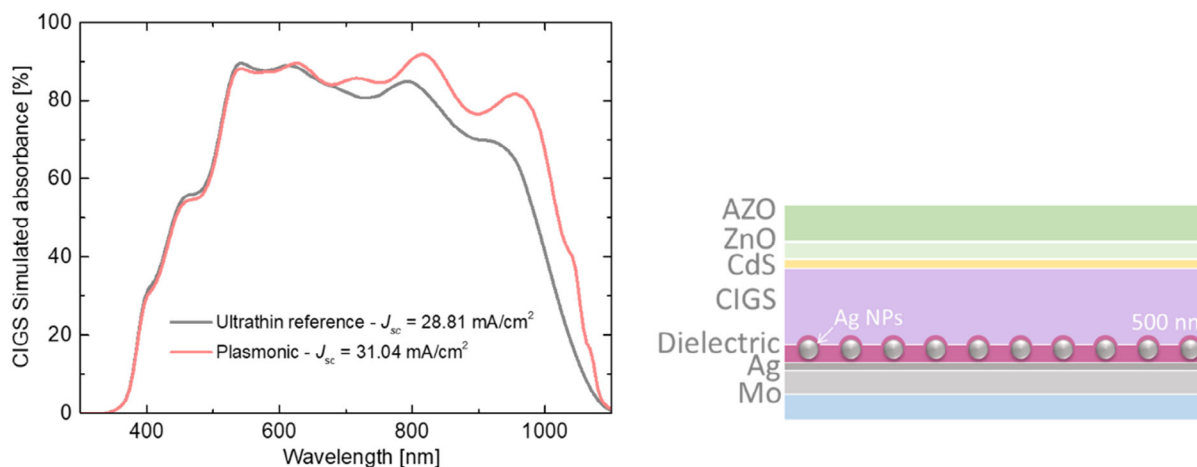


**Figure 16.** Simulated CIGS absorbance in the plasmonic configuration with an encapsulated Ag mirror and a reference solar cell with no light-trapping architecture. Adapted with permission.<sup>[43]</sup> Copyright 2021, SPIE.

from an enhanced rear scattering, as well as an improved AR as in the study by Vermang et al.<sup>[189]</sup> However, the developed Au aggregates were micrometer large, creating a highly irregular and rough rear interface, leading to a  $V_{oc}$  value decrease. In an additional work, FDTD optical simulations demonstrated the scattering benefits that can be obtained through the introduction of individualized Ag NPs with a diameter of 100 nm encapsulated with a titanium oxide ( $TiO_2$ ) layer.<sup>[43]</sup> To fully exploit the plasmonic scattering benefits, a rectangular lattice of Ag NPs with an optimized pitch was coupled with a Ag metallic mirror, with the dielectric layer on top of both, as represented in **Figure 16**. A volume compensation approach was used to introduce the NPs in the solar cell architecture, that is, the volume occupied by the metallic NPs was added to the total absorber thickness without texturization. This way, the presented optical benefits result only from an enhanced rear light scattering. The simulated absorbance of this plasmonic configuration was compared with the one of an ultrathin reference, as shown in **Figure 16**. An absolute  $J_{sc}$  enhancement of  $2.2 \text{ mA cm}^{-2}$  was obtained over the reference device.

Despite the expected beneficial effects of the metallic nanostructures, a practical implementation with a significant conversion efficiency value increase is yet to be demonstrated, mostly due to the complexity arising from the poor thermal and chemical compatibility of these nanostructures.

A broad survey of the progress in light management schemes experimentally applied at the rear of the CIGS absorber for an optical path length enhancement, through increased reflection and/or scattering, is provided in **Table 2**. For rear-contact replacement, the coupling of a metallic mirror with an encapsulation strategy has shown great promise. Several works have presented a significant  $J_{sc}$  and conversion efficiency enhancement, either through the use of a nanopatterned dielectric layer or a TCO, for the metallic mirror encapsulation.<sup>[55,191,192,194,195]</sup> To further increase the optical path length, microscale textures or resonant strategies have been applied. If a metallic mirror is coupled with plasmonic or photonic scattering approaches, the full potential of the scattering architectures can be exploited. However, the

roughness introduced by microtexturization causes a degradation of the electrical performance, and metallic NPs demonstrate fabrication compatibility issues, leading to the drop in FF and  $V_{oc}$  values when compared with reference devices, despite the  $J_{sc}$  enhancement.<sup>[65,124,189]</sup> Thus, among the scattering approaches, the use of wavelength-scale dielectric structures remains the most favorable, as besides an optical benefit, these structures additionally provide for interfacial passivation, allowing for significant conversion efficiency enhancements over reference devices.<sup>[141,216,217]</sup>

### 3.3. Spectral Conversion

In a single-junction CIGS solar cell, there are two spectral windows not efficiently exploited, as presented in **Figure 17a**: 1) the UV/vis region, due to parasitic absorption in the window and buffer layers, and thermalization losses; and 2) the active layer sub-bandgap wavelength region, resultant from nonabsorption. Passive luminescent layers, able to convert light from the uncollected spectral windows to a wavelength region efficiently absorbed by the solar cell, have emerged as a promising route to achieve full-spectrum absorption and surpass the uppermost limits established for a single-junction solar cell.<sup>[89,225–227]</sup> Three photon conversion processes can be distinguished: DS, DC, and UC, represented in **Figure 17b**. A comprehensive review over the available materials for spectral conversion can be found in the study by Huang et al.<sup>[86]</sup> and an outlook for their integration in PV systems in the study by Ferreira et al.<sup>[89]</sup>

#### 3.3.1. Spectral DS/DC

Both DC and DS processes involve the conversion of high-energy photons, that is, UV/vis, into lower-energy photons. However, DC involves one photon being converted into two, while DS is a one-to-one photon conversion process. As UV/vis photons are either absorbed in the top window layers or at the CIGS first nanometers, a beneficial effect is expected when DS/DC layers are placed in the solar cell front, as shown in **Figure 17c**.

**Table 2.** General overview of light management schemes comprising rear reflector, microtexturization, or resonant architectures, experimentally applied at the rear of the CIGS absorber. The strategy, architecture, CIGS thickness,  $J_{sc}$  and power conversion efficiency value ( $\eta$ ), as well as the relative increase in the  $J_{sc}$  and  $\eta$  values with respect to reference architectures, are listed.

Work	Strategy	Architecture	CIGS [ $\mu\text{m}$ ]	$J_{sc}$ [ $\text{mA cm}^{-2}$ ]	Relative $J_{sc}$ increase	$\eta$ [%]	Relative $\eta$ increase	Comment
Rear-contact replacement								
[185]	Direct replacement	SLG/Mo/ $\Delta^a$ )	1.4	–	–	13.8	–	700 nm-thick Mo
		SLG/W/ $\Delta$	1.4	–	–	14.2	↑ 2.9%	700 nm-thick W
		SLG/Ta/ $\Delta$	1.4	–	–	13.3	↓ 3.6%	700 nm-thick Ta
		SLG/Nb/ $\Delta$	1.4	–	–	10.0	↓ 27.5%	700 nm-thick Nb
		SLG/Cu/ $\Delta$	1.4	–	–	5.9	↓ 57.2%	700 nm-thick Cu
		SLG/V/ $\Delta$	1.4	–	–	3.4	↓ 75.4%	700 nm-thick V
[197]	Direct replacement	SLG/Mo/ZrN/ $\Delta$	0.5–0.6	24.9	–	7.2	–	1 $\mu\text{m}$ -thick ZrN
		SLG/Mo/ZrN/MoSe <sub>2</sub> / $\Delta$	0.5–0.6	25.4	↑ 2.0%	10.4	↑ 44.4%	1 $\mu\text{m}$ -thick ZrN
[192]	Nanopatterned dielectric layer encapsulation	SLG/Mo/ $\Delta$	0.62	21.4	–	5.4	–	–
		SLG/Mo/Al <sub>2</sub> O <sub>3</sub> / $\Delta$	0.62	23.1	↑ 7.9%	7.2	↑ 33.3%	18 nm-thick Al <sub>2</sub> O <sub>3</sub> Pitch: 2.8 $\mu\text{m}$ ; Line width: 0.7 $\mu\text{m}$
		SLG/Mo/Ta/Al <sub>2</sub> O <sub>3</sub> /Mo/ $\Delta$	0.62	23.4	↑ 9.3%	9.6	↑ 77.8%	10 nm-thick Ta 18 nm-thick Al <sub>2</sub> O <sub>3</sub> Pitch: 2.8 $\mu\text{m}$ ; Line width: 0.7 $\mu\text{m}$ Mo used to encapsulate metal sidewalls
[191]	Nanopatterned dielectric layer encapsulation	SLG/Mo/ $\Delta$	0.50	24.3	–	6.2	–	–
		SLG/Mo/Al <sub>2</sub> O <sub>3</sub> / $\Delta$	0.50	24.7	↑ 1.6%	7.7	↑ 24.2%	18 nm-thick Al <sub>2</sub> O <sub>3</sub> Pitch: 2.0 $\mu\text{m}$ ; Hole : 0.2 $\mu\text{m}$
		SLG/Mo/TiW/Al <sub>2</sub> O <sub>3</sub> / $\Delta$	0.50	25.3	↑ 4.1%	9.9	↑ 59.7%	20 nm-thick TiW 18 nm-thick Al <sub>2</sub> O <sub>3</sub> - Pitch: 2.0 $\mu\text{m}$ ; Hole : 0.2 $\mu\text{m}$
[195]	TCO rear contact	SLG/Mo/ $\Delta$	0.30	17.9	–	7.2	–	–
		Cu/SLG/SnO <sub>2</sub> :F/ $\Delta$	0.30	22.8	↑ 27.4%	9.5	↑ 31.9%	700 nm-thick SnO <sub>2</sub> :F
[194]	TCO encapsulation	SLG/Al <sub>2</sub> O <sub>3</sub> /Mo/ $\Delta$	0.49	22.4	–	9.3	–	–
		SLG/ITO/ $\Delta$	0.49	23.2	↑ 3.6%	10.0	↑ 7.5%	300 nm-thick ITO
		SLG/Ag/ITO/ $\Delta$	0.49	27.0	↑ 20.5%	–	–	150 nm-thick Ag 30 nm-thick ITO
[55]	TCO encapsulation	SLG/Mo/ $\Delta$	0.55	25.6	–	9.5	–	–
		SLG/AZO/Ag/AZO/ITO/Al <sub>2</sub> O <sub>3</sub> / $\Delta$	0.55	27.8	↑ 8.6%	11.3	↑ 18.9%	50 nm-thick AZO 150 nm-thick Ag 30 nm-thick AZO 100 nm-thick ITO 3 nm-thick Al <sub>2</sub> O <sub>3</sub>
[193]	TCO encapsulation	SLG/Mo/ $\Delta$	0.51	26.2	–	12.4	–	–
		SLG/AZO Ag/AZO/ITO/ $\Delta$	0.51	28.5	↑ 8.8%	11.4	↓ 8.8%	50 nm-thick AZO 150 nm-thick Ag 30 nm-thick AZO 100 nm-thick ITO
		SLG/AZO/Ag/AZO/ITO/Al <sub>2</sub> O <sub>3</sub> / $\Delta$	0.51	28.9	↑ 10.3%	12.3	↓ 0.8%	50 nm-thick AZO 150 nm-thick Ag 30 nm-thick AZO 100 nm-thick ITO 3 nm-thick Al <sub>2</sub> O <sub>3</sub>

**Table 2.** Continued.

Work	Strategy	Architecture	CIGS [ $\mu\text{m}$ ]	$J_{sc}$ [ $\text{mA cm}^{-2}$ ]	Relative $J_{sc}$ increase	$\eta$ [%]	Relative $\eta$ increase	Comment
Microscale texturization								
[214]	Random	SLG/SiO <sub>2</sub> /Mo/ $\Delta$	1.64	29.4	–	8.4	–	–
	Microtexturization	Textured SLG/SiO <sub>2</sub> /Mo/ $\Delta$	1.64	31.8	$\uparrow$ 8.2%	8.7	$\uparrow$ 3.6%	2.5 $\mu\text{m}$ SiO <sub>2</sub> spheres buried in the SLG
[65]	Random	SLG/Mo/ $\Delta$	0.46	21.2	–	6.3	–	–
	Microtexturization	SLG/Mo/Au NP aggregates/Al <sub>2</sub> O <sub>3</sub> / $\Delta$	0.46	24.9	$\uparrow$ 17.5%	5.8	$\downarrow$ 7.9%	Aggregates of 25 nm Au Nps 25 nm-thick Al <sub>2</sub> O <sub>3</sub>
[124]	Random	SLG/In <sub>2</sub> O <sub>3</sub> :Sn/ $\Delta$	0.32	19.0	–	9.0	–	–
	Microtexturization	SLG/Textured SnO <sub>2</sub> :F/ $\Delta$	0.32	21.2	$\uparrow$ 11.6%	9.0	–	Commercial SnO <sub>2</sub> :F (Asahi U-type)
Resonant architectures								
[216]	Dielectric structures	SLG/Mo/ $\Delta$	0.46	28.6	–	11.1	–	–
		SLG/Mo/SiO <sub>2</sub> Domes/ $\Delta$	0.46	30.6	$\uparrow$ 7.0%	12.3	$\uparrow$ 10.8%	SiO <sub>2</sub> dome array
[141]	Dielectric structures	SLG/Mo/ $\Delta$	0.37	23.7	–	8.8	–	–
		SLG/Mo/SiO <sub>2</sub> nanomesh/ $\Delta$	0.37	25.5	$\uparrow$ 7.6%	10.1	$\uparrow$ 14.8%	SiO <sub>2</sub> cavities Diameter: 350 nm Height: 40 nm
		SLG/Mo/SiO <sub>2</sub> nano-mesh/ $\Delta$	0.37	27.5	$\uparrow$ 16.0%	11.4	$\uparrow$ 29.5%	SiO <sub>2</sub> cavities Diameter: 350 nm Height: 150 nm
[217]	Dielectric structures	SLG/ITO/ $\Delta$	0.39	25.5	–	6.8	–	–
		SLG/ITO/SiO <sub>x</sub> cones/ $\Delta$	0.39	30.5	$\uparrow$ 19.6%	8.8	$\uparrow$ 29.4%	SiO <sub>x</sub> cone array Pitch: 513 nm; Height : 210 nm
		SLG/Ag/ITO/SiO <sub>x</sub> cones/ $\Delta$	0.39	32.4	$\uparrow$ 27.1%	10.0	$\uparrow$ 47.1%	200 nm-thick Ag SiO <sub>x</sub> cone array Pitch: 513 nm Height : 210 nm
[218]	Dielectric structures	SLG/Ti/Al/TiN/Mo/ $\Delta$	0.34	16.0	–	3.7	–	–
		SLG/Ti/Textured Al/TiN/Mo/Al <sub>2</sub> O <sub>3</sub> / $\Delta$	0.34	17.4	$\uparrow$ 8.8%	4.7	$\uparrow$ 27.0%	Voronoi cavities— Pitch: 690 nm
[215]	Dielectric structures	SLG/Mo/Al/ITO/CIGS/CdS/i-ZnO/ITO	0.6	27.3	–	11.8	–	–
		SLG/Mo/SiO <sub>2</sub> cones/Al/ITO CIGS/CdS/i-ZnO/ITO	0.6	27.9	$\uparrow$ 2.2%	–	$\downarrow$	SiO <sub>2</sub> cone array Pitch: 1.96 $\mu\text{m}$ Height: 499 nm
[189]	Metallic NPs	SLG/Mo/ $\Delta$	0.35	20.4	–	8.2	–	Flat Ga profile
		SLG/Mo/Mo Nps/ $\Delta$	0.35	21.7	$\uparrow$ 6.4%	3.2	$\downarrow$ 61.0%	Flat Ga profile Mo Nps: 150–200 nm
		SLG/Mo/Mo Nps/Al <sub>2</sub> O <sub>3</sub> / $\Delta$	0.35	22.1	$\uparrow$ 8.3%	6.4	$\downarrow$ 22.0%	Flat Ga profile Mo Nps: 150–200 nm
		SLG/Mo/ $\Delta$ /MgF <sub>2</sub>	0.38	22.2	–	8.4	–	Single-graded Ga profile
		SLG/Mo/Mo NPs/ $\Delta$ /MgF <sub>2</sub>	0.38	25.3	$\uparrow$ 14.0%	5.8	$\downarrow$ 31.0%	Single-graded Ga profile Mo NPs: 150–200 nm
		SLG/Mo/Mo Nps/Al <sub>2</sub> O <sub>3</sub> / $\Delta$ /MgF <sub>2</sub>	0.38	25.7	$\uparrow$ 15.8%	8.8	$\uparrow$ 4.8%	Single-graded Ga profile Mo NPs: 150–200 nm

<sup>a)</sup> $\Delta$  stands for CIGS/CdS/i- ZnO/AZO.

Low-energy photons will be absorbed by the DC and DS layers and re-emitted in a suitable wavelength range, around 600 nm, matching the typical maximum EQE peak of a CIGS solar cell.

Furthermore, DC materials have the potential to minimize thermalization losses in solar cell devices, as a high-energy photon is converted into two low-energy photons.<sup>[228]</sup>

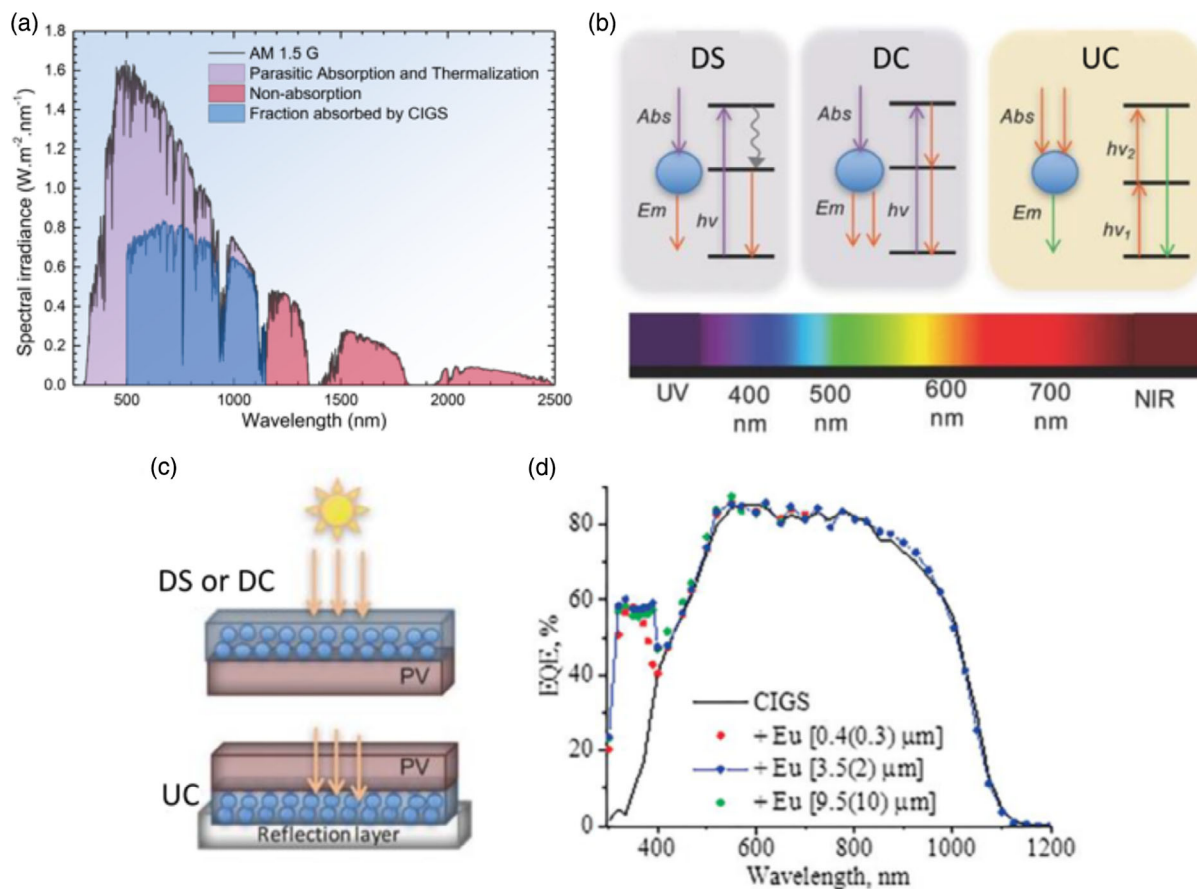


**Figure 17.** a) AM1.5 G irradiance spectrum, with the shadowed areas representing the spectral windows inefficiently exploited by a CIGS solar cell. The fraction absorbed by a CIGS solar cell with a 1.08 eV bandgap, corresponding to the record CIGS device,<sup>[11]</sup> is presented. Redrawn from [89]. b) Simplified representation of the energy diagrams in DS, DC, and UC processes. Reproduced with permission.<sup>[228]</sup> Copyright 2017, Wiley-VCH. c) Schematic representation of the integration of spectral conversion architectures in solar cell devices. Reproduced with permission.<sup>[228]</sup> Copyright 2017, Wiley-VCH. d) Experimental EQE of CIGS solar cell devices covered with  $[\text{Eu}(\text{TTA})_3(\text{TPPO})_2]$  layers of different thicknesses. Reproduced with permission.<sup>[229]</sup> Copyright 2017, Wiley-VCH.

The DS/DC materials are usually integrated within the polymer encapsulation layer.<sup>[226,229–234]</sup> In addition, luminescent layers have also been implemented between the buffer and window, either by doping a TCO with luminescent compounds or through the deposition of quantum dots (QDs).<sup>[235–238]</sup> In this placement, the luminescent layer can have a harmful effect on the solar cell FF value, which has an impact on the overall solar cell efficiency.<sup>[237,238]</sup> Therefore, the integration into an encapsulation polymer matrix appears more advantageous, as an optimization independent from the solar cell technology can be done.<sup>[229,234]</sup> In addition, if the luminescent material is integrated in an encapsulation polymer matrix, low-energy photons are converted before being parasitically absorbed in the window layers. Luminescent DS/DC layers can potentially substitute the conventional polymeric encapsulation layers, while maintaining the protective and transparency properties.<sup>[239–241]</sup> Furthermore, by the conversion of UV radiation, the DS/DC layer can reduce the polymeric layer photodegradation, consequently improving the PV module lifetime.<sup>[239]</sup> Nonetheless, a DS/DC layer must satisfy certain requirements for an efficient implementation in a PV device. The luminescent characteristic should be optimized; this

implies a wide absorption window in the 300–500 nm wavelength values range, an intense emission spectrum—meaning high quantum yield—at energy values matching the EQE peak and considerably smaller than the bandgap energy values of the window and buffer layers, and finally long-term stability.<sup>[242,243]</sup> Moreover, as in every light management technology, the cost has to be considered; hence, the development of low-cost solution-processed DS/DC layers should be favored.<sup>[243]</sup> Three approaches have been applied to CIGS solar cells in DS/DC layers: 1) organic dyes, 2) lanthanide-doped phosphors, and 3) QDs. Organic dyes are today the most used luminescent DS materials in PV, due to their near-unit quantum yield,<sup>[230,244,245]</sup> having demonstrated considerable improvements when implemented in several PV technologies, such as Si-based,<sup>[246]</sup> CdTe,<sup>[247]</sup> and CIGS solar cells.<sup>[230,234,244,248]</sup> In addition, they can be easily integrated in polymer matrixes by solution process methods, having led, in CIGS solar cells, to relative efficiency enhancements of up to 8.5%, compared with a reference solar cell.<sup>[244]</sup> Still, research efforts have been applied to find more suitable alternatives, as the narrow absorption band limits the viability of the organic dyes. For a full coverage of the

desired spectral window, more than one type of dye is required.<sup>[246]</sup> Currently, the variety of organic dyes integrated in CIGS solar cells have shown absorption bands between 300 and 500 nm and an emission spectra between 400 and 600 nm. A limited shift between emission and absorption spectra, typically below 50 nm, is an inherent characteristic of these organic molecules, limiting the efficiency of the DS layer due to reabsorption of the emitted photons.<sup>[229,232,242,249,250]</sup> Furthermore, long-term stability upon irradiation can be quite challenging with organic dyes, as every organic molecule presents unique chemical properties that are dependent on the embed polymer matrix. A proper optimization of host polymer matrix and luminescent molecules combination is required, as an unstable environment or unstable luminescent molecules lead to a deterioration of the DS/DC phenomenon.<sup>[229,231,232,251]</sup> In contrast, lanthanide-doped phosphors are stable over long irradiation periods, present high thermal resistance, and, depending on the lanthanide complex and host matrix, can have high quantum yields (>80%).<sup>[86,229,232]</sup> However, the major benefit arising from these rare-Earth materials is the ability to obtain a significant shift between the absorption and excitation spectrum with no overlap; hence, avoiding the reabsorption of emitted light.<sup>[229]</sup> A great variety of works have reported a conversion efficiency enhancement in CIGS solar cells stemming from a DC or DS of UV/vis light through the use of rare-Earth complexes.<sup>[229,232,235,237,249]</sup> Gavriluta et al. studied the effect of 13 different ternary europium (Eu<sup>III</sup>) complexes on top of CIGS solar cells.<sup>[229]</sup> The luminescent DS layers were deposited directly on top of the CIGS solar cell device. Besides changing the material complexes, the thickness of the luminescent layer was optimized. Two deposition methods, spin coating and drop casting, were adjusted to attain nanosized- and micro-sized-thick layers. The best-performing layer used [Eu(TTA)<sub>3</sub>(TPPO)<sub>2</sub>] as luminescent material and had a broad absorption spectrum ranging from 250 to 420 nm and a narrow emission peak at around 615 nm. An enhancement of 1.8 mA cm<sup>-2</sup> on the  $J_{sc}$  value was obtained over the reference device. This optical improvement resulted from the high quantum yield obtained with this compound (72%), along with a beneficial AR effect arising from the polymer EVA matrix, where the luminescent materials were embedded. It was estimated that the DS process solely was responsible for 0.8 mA cm<sup>-2</sup> of the observed  $J_{sc}$  increase. The improved UV response is shown in Figure 17d, where the EQE of the CIGS solar cell devices with the [Eu(TTA)<sub>3</sub>(TPPO)<sub>2</sub>]-based DS layer with different thickness values is compared with a reference device. However, a limitation of this approach comes from the size of the phosphor particles. Typically, the phosphors consist of micro-sized particles that promote a strong light backscattering, inhibiting an efficient light incoupling toward the solar cell.<sup>[231,243,249]</sup> Nanosized semiconductor QDs do not demonstrate such scattering effects.<sup>[233,249]</sup> The broad light absorption, narrow emission spectrum, high quantum yield, high photostability, and size-dependend bandgap make these nanostructures very interesting to be applied as a DS/DC layer.<sup>[226,231,233,252]</sup> A broad survey of progress in light management schemes experimentally applied at the front layers of CIGS solar cells through DS or DC is provided in Table 3. When DS/DC approaches are coupled to CIGS solar cells, these QD nanostructures have shown the highest  $J_{sc}$

enhancements.<sup>[226,238]</sup> However, the development and application of QD luminescent layers have been lagging, as the most typical material complexes used for these luminescent materials are Cd or In based, which are critical and/or toxic materials.<sup>[226,238,250,252–254]</sup> Recently, perovskite CsPbX<sub>3</sub> nanocrystals and graphene QDs have demonstrated high quantum yields, while being nontoxic solution-compatible alternatives.<sup>[233,253,255–257]</sup> For example, Khan et al. were able to achieve a 1.1 mA cm<sup>-2</sup> enhancement of the  $J_{sc}$  value on a CIGS solar cell device by introducing N-functionalized graphene QDs at the solar cell top.<sup>[255]</sup> The developed nanostructures demonstrated a broad absorption band (200–400 nm) and a narrow emission peak around 503 nm. The  $J_{sc}$  value increase is a combination of the DC of low-energy photons, as well as from AR and light-trapping effects, promoted through the presence of the QD layer.<sup>[255]</sup>

### 3.3.2. Spectral UC

UC processes involve the conversion of two or more photons transparent to the absorber ( $\lambda > 1200$  nm) into usable photons with energy higher than the absorber bandgap. Conceptually, some issues hamper the efficiency of UC materials when placed at the solar cell front, as they might decrease the transmittance of the incident light to the absorber. Hence, a better use of the UC luminescent materials is reached when they are placed at the CIGS rear interface (Figure 17c).<sup>[89,228]</sup> For the UC process to occur, the absorption of at least two photons is required; hence, the quantum yield is limited to 50%. Nonetheless, the utilization of UC layers would hamper losses arising in the wasted IR region of the solar spectrum, which totals nearly 35% of the spectral photon flux, that is,  $1.5 \times 10^{17}$  photons s<sup>-1</sup> cm<sup>-2</sup> of the  $4.3 \times 10^{17}$  photons s<sup>-1</sup> cm<sup>-2</sup> allowed by the AM 1.5 G incident spectrum. A theoretical conversion efficiency value limit of 47.6% was established by Trupke et al., for SQ solar cell devices with UC layers.<sup>[258]</sup> Regarding PV applications, the great majority of the UC mechanisms result from the combination of excited-state absorption (ESA) and energy transfer UC (ETU) processes.<sup>[86]</sup> ESA is a two-step process in which two or more photons are absorbed in an intermediate-energy level. The first absorbed photon allows an electronic transition from the ground to an intermediate state, and a sequential absorption of a second photon promotes the transition to a higher energy state. Consequently, a higher-energy photon is emitted from the transition between the excited to the ground state.<sup>[86,89]</sup> The ETU process involves the excitation of two neighboring ions into a metastable energy state by two photons. Nonradiative energy exchanges, then promote one ion to a higher-energy-emitting state.<sup>[86,89]</sup> These processes can be accomplished using lanthanide-based systems in an extensive variety of materials covering a wide range of shapes and sizes. However, there are considerable limitations regarding the use of lanthanide-doped complexes for UC processes, as metastable intermediate levels are required.<sup>[86,89]</sup> Moreover, lanthanide-doped materials for UC have a narrow and weak absorption band, being only able to upconvert a small solar spectrum fraction. Coupling the lanthanide complexes with organic dye molecules can improve the absorption capabilities of the UC material.<sup>[89]</sup> The organic dyes



**Table 3.** General overview of light management schemes comprising DC and DS, experimentally applied at the front layers of CIGS solar cells. The strategy, architecture, CIGS thickness,  $J_{sc}$ , and power conversion efficiency value ( $\eta$ ), as well as the relative increase in the  $J_{sc}$  and  $\eta$  values with respect to reference architectures, are listed.

Work	Strategy	Architecture	CIGS [ $\mu\text{m}$ ]	$J_{sc}$ [ $\text{mA cm}^{-2}$ ]	Relative $J_{sc}$ increase	$\eta$ [%]	Relative $\eta$ increase	Comment
[248]	Fluorescent dye	▲ <sup>a)</sup> /Glass	–	26.1	–	14.0	–	–
		▲/Glass/PMMA with fluorescent dye	–	27.6	↑ 5.7%	14.8	↑ 5.7%	Lumogen F Violet 570 and Yellow 083
[244]	Fluorescent dye	▲	1.7	35.1	–	–	–	–
		▲/EVA with fluorescent dye	1.7	38.1	↑ 8.5%	–	–	Lumogen F Violet 570
[234]	Fluorescent dye	Commercial cell/Eva	–	7.5	–	15.1	–	–
		Commercial cell/Eva with fluorescent dye	–	7.9	↑ 5.3%	15.8	↑ 4.6%	Glutanide-derived pyrene with Coumarin 6
		Commercial cell/Eva with fluorescent dye	–	7.7	↑ 2.7%	15.3	↑ 1.3%	Glutanide-derived pyrene with Nile Red
[230]	Fluorescent dye	▲	–	25.6	–	8.8	–	–
		▲/PVB with fluorescent dye	–	25.9	↑ 1.2%	8.9	↑ 1.1%	Lumogen F Violet 570
		▲/PVB with fluorescent dye	–	25.8	↑ 0.8%	8.9	↑ 1.1%	Lumogen F Yellow 083
		▲/PVB with fluorescent dye	–	26.4	↑ 3.1%	9.2	↑ 4.5%	Lumogen F Violet 570 and Yellow 083
[231]	Nanostructured organosilicon luminophores (NOLs)	▲	–	29.1	–	9.3	–	–
		▲/PVB with NOLs	–	30.2	↑ 3.8%	9.7	↑ 4.3%	NOL 15
		▲/EVA with NOLs	–	29.8	↑ 2.4%	9.6	↑ 3.2%	NOL 15
[229]	Rare-Earth compound	▲	2	29.0	–	–	–	–
		▲/EVA with rare-Earth compound	2	30.8	↑ 6.2%	–	–	Eu(TTA) <sub>3</sub> (TPPO) <sub>2</sub>
[232]	Rare-Earth compound	▲	2	–	–	13.1	–	–
		▲/EVA with rare-Earth compound	2	–	–	13.9	↑ 6.1%	[Eu(TTA) <sub>3</sub> (DPEPO)]
[235]	Rare-Earth compound	■ <sup>b)</sup> /SnO <sub>2</sub> with rare-Earth compound/AZO	–	32.3	–	10.4	–	SnO <sub>2</sub> :Nd
[236]	Rare-Earth compound	▲	2.5	28.7	–	9.9	–	–
		■/SnO <sub>2</sub> with rare-Earth compound/AZO	2.5	29.3	↑ 2.1%	10.5	↑ 6.1%	SnO <sub>2</sub> :Yb
[249]	Rare-Earth compound	▲	2.0–3.0	32.7	–	17.7	–	–
		▲/MgF <sub>2</sub>	2.0–3.0	34.2	↑ 4.6%	18.5	↑ 4.5%	110 nm thick MgF <sub>2</sub>
		▲/Coupling layer/Y <sub>3</sub> Al <sub>5</sub> O <sub>12</sub> /MgF <sub>2</sub>	2.0–3.0	34.2	↑ 4.6%	18.5	↑ 4.5%	110 nm-thick MgF <sub>2</sub> Coupling layer: $n = 1.8$ , Cargille, USA
		▲/Coupling layer/Y <sub>3</sub> Al <sub>5</sub> O <sub>12</sub> doped with rare-Earth compound/MgF <sub>2</sub>	2.0–3.0	34.8	↑ 6.4%	19.0	↑ 7.3%	110 nm-thick MgF <sub>2</sub> Coupling layer: $n = 1.8$ , Cargille, USA Y <sub>3</sub> Al <sub>5</sub> O <sub>12</sub> :Ce
[237]	Rare-Earth compound	▲	1.5–1.7	38.5	–	11.2	–	–
		■/ZTO with rare-Earth compound/AZO	1.5–1.7	39.2	↑ 1.8%	10.3	↓ 8.0%	100 nm-thick ZTO:Yb
[238]	QDs	SS/Mo/CIGS/CdS/i-ZnO/AZO	2	31.9	–	8.4	–	–
		SS/Mo/CIGS/CdS/QDs/i-ZnO/AZO	2	35.5	↑ 11.3%	9.3	↑ 10.7%	10 nm aggregates of 3–5 nm CdSe/ZnS core–shell QD
[252]	QDs	▲	2	32.6	–	13.8	–	–
		▲/QDs/MgF <sub>2</sub>	2	34.0	↑ 4.3%	14.3	↑ 3.6%	CdSe/CdZnS core–shell QDs: 5.5 nm

**Table 3.** Continued.

Work	Strategy	Architecture	CIGS [ $\mu\text{m}$ ]	$J_{sc}$ [ $\text{mA cm}^{-2}$ ]	Relative $J_{sc}$ increase	$\eta$ [%]	Relative $\eta$ increase	Comment
[255]	QDs	▲	3	30.7	–	14.4	–	–
		▲/QDs	3	31.8	↑ 3.6%	15.3	↑ 6.3%	N-functionalized graphene QDs: 2–4 nm
[256]	QDs	▲	3	29.7	–	–	–	–
		▲/QDs	3	32.1	↑ 8.1%	–	↑ 12.2%	N-functionalized graphene QDs: 3.9 nm
[226]	QDs	SLG/CIGS solar cell/	–	22.0	–	–	–	–
		SLG/CIGS solar cell/PMMA with QDs	–	24.1	↑ 9.5%	–	–	CdSe QDs: 2 nm
[170]	QDs	▲	–	34.0	–	13.0	–	–
		▲/QDs/NOA 164/Glass	–	35.3	↑ 3.8%	13.6	↑ 4.6%	CdSe/CdZnS core–shell QDs: 5.5 nm
		▲	–	34.1	–	13.6	–	–
[250]	QDs	▲/QDs/NOA 164/Textured glass	–	36.6	↑ 7.3%	14.6	↑ 7.4%	CdSe/CdZnS core–shell QDs: 5.5 nm Nanotexturization
		SS/EVA/CIGS solar cell/EVA/Glass	–	26.6	–	10.7	–	–
[233]	QDs	SS/EVA/CIGS solar cell/EVA/glass with QDs	–	27.0	↑ 1.5%	10.8	↑ 0.9%	InP/ZnSe <sub>x</sub> S <sub>1–x</sub> QDs: 3.5 nm
		CIGS solar cell	–	24.9	–	8.8	–	–
[253]	Nanocrystal	CIGS solar cell/NOA with QDS	–	27.1	↑ 8.8%	9.7	↑ 10.2%	N-functionalized graphene QDs: <10 nm
		SS/Mo:Na/Mo/CIGS/CdS/i-ZnO/AZO	2	35.6	–	11.1	–	–
[257]	Nanocrystal	SS/Mo:Na/Mo/CIGS/CdS/i-ZnO/AZO/Nanocrystals	2	37.2	↑ 4.5%	11.6	↑ 4.5%	Cubic-shaped CsPbBr <sub>3</sub> perovskites Nanocrystals Diagonal length: 8–18 nm
		▲/Quartz	1.2–2.2	27.0	–	13.0	–	–
		▲/Quartz with nanocrystals	1.2–2.2	28.9	↑ 7.0%	13.2	↑ 1.5%	Cubic-shaped CsPbBr <sub>3</sub> perovskites Nanocrystals: 10–13 nm

<sup>a)</sup>▲ stands for SLG/Mo/CIGS/CdS/i-ZnO/AZO. <sup>b)</sup>■ stands for SLG/Mo/CIGS/CdS.

can trap incoming photons over a broad range of wavelength values, thus improving the spectral response of the UC approach. However, the photon conversion efficiency of the lanthanide-based UC process is still very low (<3%), and unless new technologies or materials are developed, the implementation in CIGS devices is not yet viable.<sup>[86,89]</sup> UC processes following the sensitized triplet–triplet annihilation (TTA) phenomenon using chromophores appear as an alternative, as high-photon conversion efficiencies can be achieved even at low-excitation power densities.<sup>[259–261]</sup> Photon conversion efficiencies of over 30% have been reported for the TTA upconvertors.<sup>[259–261]</sup>

TTA systems have been generally applied in wide-bandgap solar cells and for photocatalytic water splitting for hydrogen production, as the absorbance UC spectrum of this approach is usually around the 650–700 nm wavelength range.<sup>[86,89]</sup> For wavelength values higher than the mentioned range, high-efficiency TTA UC systems have not yet been achieved.<sup>[89]</sup> Kozinsky et al. predicted through FDTD simulations a conversion efficiency enhancement up to 5% in a wide-bandgap ( $\approx 1.6$  eV) CIGS device through the implementation of the TTA-based UC layer at the solar cell rear structure.<sup>[262]</sup> However, high-efficiency CIGS solar cells typically have a Ga profile with a minimum bandgap value of around

1.1 eV,<sup>[11,31]</sup> for which the most efficient UC systems are not compatible. Despite the promising concept, the current technological outlook in luminescent upconvertors does not allow for a cost-effective and efficient implementation of UC layers in CIGS devices.

#### 4. Light Management in Mono-Si World Record Device

Si-based solar cells are at the forefront of PV evolution and progress when it comes to light management. Many optical architectures have first been implemented on mono-Si, multi-crystalline Si, or amorphous Si solar cells before expanding to other efficient and promising PV technologies.<sup>[50,122]</sup> The requirement to reduce optical losses through innovative schemes has been present for more than 40 years, mostly to overcome the shortcomings of the indirect bandgap nature of Si solar cells.<sup>[122]</sup>

The great dilemma is why is not a mature CIGS technology fulfilling its optical potential? To answer this question, we must discriminate the optical characteristics of the current world record mono-Si architecture that allow for efficient light harvesting. The state-of-the-art mono-Si solar cell architecture is shown in **Figure 18**. The most notable example of a light management scheme in this architecture, is the square-based pyramid random texturization, which is now an industry standard.<sup>[263]</sup> This scheme is fabricated by anisotropic etching procedures on the absorber interface, with its first application dating back to 1974.<sup>[18,264]</sup> As detailed in Section 3.1.2, a microtextured front surface allows for an omnidirectional low reflectance, due to multiple interactions in the large pyramidal textures.<sup>[93,119]</sup> In addition, this architecture is coupled with highly reflective Al rear electrodes. Hence, an optical path length enhancement of up to  $4n^2$  can be obtained with this optical scheme.<sup>[122]</sup> However, implementing microscale textures directly at the front surface of a thin-film absorber, such as CIGS, is not straightforward. Due to the already thin absorber, these devices will be severely limited by interface recombination, as the texturing dimensions are similar to the absorber thickness. Moreover, a highly reflective rear contact has been one of the optical pitfalls of the CIGS architecture. However, the backbone of the Si high-efficiency devices is the IBC configuration. The IBC concept is highly efficient mostly due its outstanding optical and electrical benefits. In optical terms, having the contacts on the back surface allows for light to reach the absorber layer untampered, introducing a concept with no shading or parasitic absorption.<sup>[18,82]</sup> In addition, the

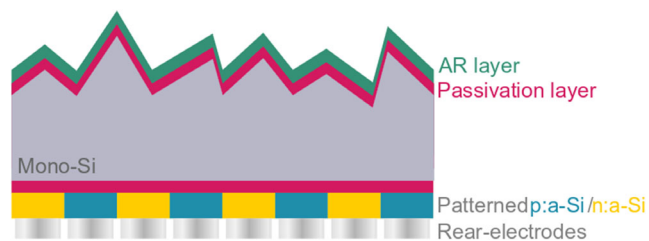


**Figure 18.** Schematic representation of the world record mono-Si solar cell architecture.<sup>[18]</sup>

absence of thick TCO window layers opens the door to the implementation of more advanced light management concepts at the front surface, such as diffraction gratings, dielectric structures, and metallic NPs. In electrical terms, having the contacts in a distance close to the charge carrier diffusion length allows reducing series resistance losses and recombination. With these advantages, it is not a surprise that the most efficient Si solar cell is an IBC one. Currently, the CIGS state-of-the-art architecture is substrate type. In this configuration, the substrate is only used as a mechanical support and a back-metal layer is the first electrode. The second electrode is a TCO layer that has to be transparent as light reaches the absorber layer through this interface, while at the same time preserving a high conductivity. Typically, the window layers in a CIGS solar cell are hundreds of nanometers in thickness, leading to a considerable parasitic absorption of the incident photons. Therefore, CIGS solar cells would benefit from this IBC approach.<sup>[82]</sup> Nevertheless, strives in finding compatible selective contacts for charge carrier separation and collection, as well as in interfacial passivation, are required. Furthermore, the CIGS carrier diffusion length lower than  $10\ \mu\text{m}$  demands a micro-/nanofabrication process step in the solar cell fabrication and may increase the probability of electrical shunt formation, as the gap between the contacts needs to be smaller or comparable with this value.<sup>[82,265]</sup>

#### 5. Conclusion and Future Perspectives

For a solar cell to reach its full optical potential, light management approaches must be applied such that: 1) omnidirectional reflection of incident light is reduced to zero; 2) light trapping is promoted to increase the optical path length in the absorber; and 3) a full-spectrum harvesting is achieved, assuring efficient absorption. Accomplishing the established requirements through the exploitation of cost-effective light management provides a roadmap to reach higher-energy production levels at lower costs.

The current  $\text{MgF}_2$  ARC, commonly used in high-efficiency world record cells, enables a 1% conversion efficiency enhancement. However, its AR performance is optimized for incident light angles close to normal incidence and specific wavelength values. Therefore, interference-type AR underperforms in terms of omnidirectional and broadband AR. These phenomena must be present for efficient light incoupling, especially for BIPV panels without tracking systems, where an optimal performance is desired for diffuse incident light conditions. Other approaches are being explored to satisfy the ARC limitations, such as micro-scale-textured front surfaces or resonant schemes, as they allow for a broadband reflection minimization over different illumination angles. Micrometer features, larger than the incident light wavelength, assist for an omnidirectional broadband reflection minimization, improving the transmission probability.<sup>[93,119]</sup> Furthermore, large-angle refraction is promoted in these architectures. Resonant schemes, such as metallic NPs or dielectric structures, take advantage of either plasmonic or photonic effects to achieve improved light localization or trapping.<sup>[70]</sup> Nonetheless, the expected light-trapping benefits from micro-scale or resonant approaches are hampered by parasitic absorption in the thick window layers, present in the current state-of-

the-art CIGS architecture. A different contact design architecture, such as IBC, would help unveil the full potential of these strategies, as it eliminates the need for window layers, and light localization effects can effectively be exploited enabling efficient light incoupling. However, the IBC architecture requires advances in interfacial passivation and extensive research on selective contact materials for CIGS solar cells. Furthermore, the relatively low carriers' diffusion length for CIGS might raise fabrication and architectural issues, limiting the IBC approach.<sup>[265]</sup> Hence, for the current substrate-type architecture, light management schemes at the front surface should provide a broadband and omnidirectional AR effect, without significant light scattering. Nanoscale features, with critical dimensions significantly smaller than the incident wavelength values, do not promote light scattering, and a significant AR performance can be achieved. A low-cost and high-throughput technique, that is scalable for large-area deposition and applicable in commercial PV modules, should be searched for the fabrication of nanoscale arrays. Texturing approaches, through nanoimprint lithography or one-step wet-etching procedures, exhibit potential, as they are capable of texturing large areas at a fraction of a cost of other lithography techniques.<sup>[39,97,116]</sup> For a continuous improvement of the nanoscale architecture performance, the implementation in a PV commercial module should be considered. PV modules are subject to several atmospheric agents and conditions. The accumulation of particles at the module surface may hamper the light incoupling and promote their degradation through hot-spots.<sup>[266,267]</sup> Hence, an additional requirement for this ARC is to add different functionalities, such as self-cleaning or antifogging.<sup>[266,267]</sup> Several works have been exploiting subwavelength architectures for that purpose in other PV technologies, as they are in the size range required for a superhydrophobic behavior.<sup>[266–268]</sup>

Light-trapping strategies have to be developed to overcome incomplete light absorption problems, inherent to thinner devices. Currently, the most prominent light-trapping limitation in the state-of-the-art CIGS architecture is the poor Mo reflector. Hence, efforts should be made to replace it for a more beneficial optical configuration, that still preserves a good electrical contact and that survives the absorber preparation. Two strategies to integrate a rear metallic mirror have demonstrated potential: 1) metallic mirror encapsulation with a nanopatterned passivation layer and 2) a TCO rear contact coupled with a metallic mirror. By encapsulating the mirror with the passivation layer, both an interface passivation effect and improved optical reflection can be achieved. Nonetheless, there are still some concerns with this approach as the surface coverage occupied by the metallic layer is limited by the line- or point-contact pattern, hindering the overall reflectivity. Furthermore, for an effective encapsulation of the metallic mirror, the dielectric layer needs to cover the side walls, which increases the complexity of the lithographic procedure.<sup>[191]</sup> Recent progress has been made by establishing the rear contact with a TCO coupled with a metallic mirror. Nonetheless, this approach requires lower deposition temperatures, as a resistive Ga<sub>2</sub>O<sub>3</sub> interface layer is formed at high temperatures at the TCO/CIGS interface. Although world record CIGS devices still depend on high-deposition temperatures, ACIGS solar cells with a conversion efficiency value of 18.5%

have recently been produced at low temperatures ( $\approx 303$  °C) on SLG substrates, a disruptive result that paves the way for the metallic mirror integration.<sup>[67]</sup> However, although the pathway starts by implementing a metallic mirror, the light-trapping ability has to go even further. As a perfect reflector only doubles the optical path length, light scattering from the rear interface is required. One way to do so is using microscale texturization at the rear contact. Nevertheless, for an efficient light-trapping performance, the size of the microscale features is in the same dimension of the absorber thickness, which leads to a complex solar cell fabrication process and fundamental issues. Hence, the research has moved toward resonant architectures, such as dielectric nanostructures and metallic NPs, capable of exciting waveguide modes in the absorber. Up until now, the architectures that have provided a significant optical enhancement, while maintaining suitable  $V_{oc}$  and FF values, are based on SiO<sub>2</sub> dielectric nanostructures.<sup>[217]</sup> Nonetheless, encapsulated metallic NPs are able to strongly scatter light with much smaller dimensions, due to the sustained LSPs<sup>[148,149,221]</sup>, and consequently ease the fabrication of the CIGS device. If the metallic nanostructures are coupled with encapsulation and passivation approaches, the electrical performance obtained with large SiO<sub>2</sub> nanostructures can be surpassed. However, until a beneficial practical implementation is demonstrated, through the smaller metallic nanostructures, dielectric structures are the most viable light-trapping options.

Full-spectrum harvesting is limited by losses in the UV/vis and IR regions. Thermalization and parasitic absorption in the UV/vis region hamper an efficient collection of low-wavelength photons. DS/DC layers have been used at the front of CIGS solar cell devices, to absorb the UV/vis region photons into a wavelength range efficiently harvested by the solar cell. The IR spectrum region can be converted using UC layers at the rear contact of the solar cell. Several photoluminescent approaches have been used for spectral conversion purposes. For DS/DC approaches, QDs have allowed for the best performance when coupled to CIGS solar cells,<sup>[226,238]</sup> due to their broad light absorption (250–500 nm), narrow emission spectrum, and high quantum yield. Nonetheless, concerns regarding the cost and toxicity are present, as most luminescent QDs approaches are Cd or In based. Hence, research efforts have moved to alternative material complexes, such as the perovskite CsPbX<sub>3</sub> nanocrystals and graphene QDs. For UC approaches, the materials compatible with the bandgap of conventional CIGS devices have not yet demonstrated sufficiently high photon conversion efficiencies. Therefore, for the implementation of luminescent layers in CIGS solar cells, continuous progress toward low-cost and efficient UC materials is required. Nonetheless, promising UC efficiencies ( $\approx 10\%$ ) for IR light absorption have been demonstrated with lanthanide-doped complexes, by high-power density excitation with focused sunlight.<sup>[89,269,270]</sup> Hence, coupling UC lanthanide-doped nanomaterials with light-trapping strategies that promote light localization effects, such as plasmonic and dielectric NPs, solar concentrators, or photonic crystals, might be a pathway for an efficient integration of the state-of-the-art UC technology in CIGS solar cells.<sup>[86,89]</sup>

## 6. Experimental Section

**Penetration Depth Calculation:** In-house spectroscopy ellipsometry data were used for the calculation of the light penetration depth in a bulk CIGS material. The CIGS absorption coefficient ( $\alpha$ ) was calculated through:

$$\alpha = \frac{4\pi k}{\lambda} \quad (4)$$

with  $k$  being the extinction coefficient and  $\lambda$  wavelength values. The light penetration depth represented the distance at which the light intensity fell by a factor of  $1/e$  and was given by the inverse of the absorption coefficient  $\alpha^{-1}$ . The  $\alpha$  dependence on wavelength gave rise to a penetration depth wavelength dependence. Generally, semiconductor materials have a large absorption coefficient for high-energy (short-wavelength) photons that decrease with increasing wavelength value. Hence, blue light was absorbed in considerably small depths, whereas considerably higher depths were required for the absorption of red light.

**FDTD Optical Simulations:** Optical simulations were conducted using the FDTD solutions package from the commercial Lumerical software.<sup>[27]</sup> The FDTD method provided direct space and time solutions of the Maxwell equations in complex geometries. The studied reference structure consisted of the following stack: Mo (350 nm)/CIGS/CdS (30 nm)/i-ZnO (50 nm)/AZO (150 nm). In-house spectroscopy ellipsometry measurements were used to obtain the optical constants for CIGS, whereas the optical parameters for the ZnO:Al, i-ZnO and CdS layers were taken from the study by Carron et al.,<sup>[10]</sup> Mo from Werner et al.,<sup>[27]</sup> and MoSe<sub>2</sub> from Beal et al.<sup>[27]</sup> The solar cell stack was illuminated through a broadband plane wave source, with wavelength values ranging from 300 nm to 1000 nm. The Cartesian mesh size used was the smallest possible considering the memory and time requirements of each simulation. Override mesh regions were used at critical interfaces for higher accuracy. Symmetric and antisymmetric boundary conditions were used, reducing by 3/4 the total simulation volume.

**Literature Search:** To have a broad view of the published literature, a survey of the field of light management in solar cell devices was performed, using VOSviewer with a sample data consisting of the information from published articles, letters, reviews, and books from the Scopus database. The following terms were used in the Scopus search: (“Solar cell” AND “Light management”). From each article, information such as the document title, abstract, keywords, and authors’ names was obtained. This allowed for a broad overview of the evolution and current outlook of the light management implementation in different PV technologies. Then, a more focused search was performed, using the terms (“Solar cell” AND (“CIGS\*” OR “CuInGaSe” OR “Copper Indium Gallium Selenide” OR “Copper Indium Gallium Di\*”) AND (“Light management\*”). The main research topics in light management architectures applied to CIGS solar cells could this way be identified. Then, a comprehensive and exhaustive search was performed to include all the experimental works in the survey tables, related to the implementation of the reviewed light management strategies in CIGS solar cells.

## Acknowledgements

Fundação para a Ciência e a Tecnologia (FCT) and Fundo Social Europeu (FSE) are acknowledged through the projects IF/00133/2015, UIDB/50025/2020, UIDP/50025/2020, UIDB/04730/2020, UIDP/04730/2020, and DFA/BD/4564/2020. This research was also supported by NovaCell—Development of novel Ultrathin Solar Cell Architectures for low-light, low-cost, and flexible optoelectronic device project (028075) cofunded by FCT and ERDF through COMPETE2020. This research was supported by InovSolarCells—Development of innovative nanostructured dielectric materials for interface passivation in thin-film solar cells project (029696) cofunded by FCT and ERDF through COMPETE2020. The authors acknowledge the financial support of the project Baterias 2030, with the reference POCI-01-0247-FEDER-046109, cofunded by Operational Programme for Competitiveness and Internationalization

(COMPETE 2020), under the Portugal 2020 Partnership Agreement, through the European Regional Development Fund (ERDF).

## Conflict of Interest

The authors declare no conflict of interest.

## Keywords

Cu(In,Ga)Se<sub>2</sub>, light management, light trapping, solar cells

Received: June 30, 2021

Revised: December 27, 2021

Published online:

- [1] IRENA, International Renewable Energy Agency, *Market Integration of Distributed Energy Resources Innovation Landscape Brief*, Abu Dhabi **2019**.
- [2] IRENA, International Renewable Energy Agency, *Peer-to-Peer Electricity Trading: Innovation Landscape Brief*, Abu Dhabi **2020**.
- [3] M. R. Alam, M. St-Hilaire, T. Kunz, *Appl. Energy* **2019**, 238, 1434.
- [4] S. Zhou, F. Zou, Z. Wu, W. Gu, Q. Hong, C. Booth, *Int. J. Electr. Power Energy Syst.* **2020**, 114, 105378.
- [5] D. Neves, I. Scott, C. A. Silva, *Energy* **2020**, 205, 118023.
- [6] A. Ahl, M. Yarime, K. Tanaka, D. Sagawa, *Renew. Sustain. Energy Rev.* **2019**, 107, 200.
- [7] M. J. A. Baig, M. T. Iqbal, M. Jamil, J. Khan, In *11th Annual IEEE Information Technology, Electronics and Mobile Communication Conf., IEMCON 2020*, IEEE, Piscataway, NJ **2020**, p. 0402.
- [8] *CIGS White Paper*, **2019**.
- [9] I. M. Peters, C. D. Rodriguez Gallegos, S. E. Sofia, T. Buonassisi, *Joule* **2019**, 3, 2732.
- [10] R. Carron, E. Avancini, T. Feurer, B. Bissig, P. A. Losio, R. Figi, C. Schreiner, M. Bürki, E. Bourgeois, Z. Remes, M. Nesladek, S. Buecheler, A. N. Tiwari, *Sci. Technol. Adv. Mater.* **2018**, 19, 396.
- [11] M. Nakamura, K. Yamaguchi, Y. Kimoto, Y. Yasaki, T. Kato, H. Sugimoto, *IEEE J. Photovolt.* **2019**, 9, 1863.
- [12] J. Lindahl, U. Zimmermann, P. Szaniawski, T. Torndahl, A. Hultqvist, P. Salomé, C. Platzer-Björkman, M. Edoff, *IEEE J. Photovolt.* **2013**, 3, 1100.
- [13] A. Chirilă, S. Buecheler, F. Pianezzi, P. Bloesch, C. Gretener, A. R. Uhl, C. Fella, L. Kranz, J. Perrenoud, S. Seyrling, R. Verma, S. Nishiwaki, Y. E. Romanyuk, G. Bilger, A. N. Tiwari, *Nat. Mater.* **2011**, 10, 857.
- [14] I. Repins, M. A. Contreras, B. Egaas, C. DeHart, J. Scharf, C. L. Perkins, B. To, R. Noufi, *Prog. Photovolt.: Res. Appl.* **2008**, 16, 235.
- [15] P. Jackson, D. Hariskos, E. Lotter, S. Paetel, R. Wuerz, R. Menner, W. Wischmann, M. Powalla, *Prog. Photovolt.: Res. Appl.* **2011**, 19, 894.
- [16] ISE Fraunhofer Institute for Solar Energy Systems, *Photovolt. Rep.* **2020**, Freiburg.
- [17] V. Bermudez, A. Perez-Rodriguez, *Nat. Energy* **2018**, 3, 466.
- [18] K. Yoshikawa, H. Kawasaki, W. Yoshida, T. Irie, K. Konishi, K. Nakano, T. Uto, D. Adachi, M. Kanematsu, H. Uzu, K. Yamamoto, *Nat. Energy* **2017**, 2, 17032.
- [19] P. M. P. Salomé, A. Hultqvist, V. Fjallstrom, M. Edoff, B. G. Aitken, K. Zhang, K. Fuller, C. Kosik Williams, *IEEE J. Photovolt.* **2014**, 4, 1659.
- [20] P. M. P. Salomé, H. Rodriguez-Alvarez, S. Sadewasser, *Sol. Energy Mater. Sol. Cells* **2015**, 143, 9.
- [21] H. Lee, Y. Jang, S. W. Nam, C. Jung, P. P. Choi, J. Gwak, J. H. Yun, K. Kim, B. Shin, *ACS Appl. Mater. Interfaces* **2019**, 11, 35653.

- [22] S. Siebentritt, E. Avancini, M. Bär, J. Bombsch, E. Bourgeois, S. Buecheler, R. Carron, C. Castro, S. Duguay, R. Félix, E. Handick, D. Hariskos, V. Havu, P. Jackson, H. Komsa, T. Kunze, M. Malitckaya, R. Menozzi, M. Nesladek, N. Nicoara, M. Puska, M. Raghuvanshi, P. Pareige, S. Sadewasser, G. Sozzi, G. A. N. Tiwari, S. Ueda, A. Vilalta-Clemente, T. P. Weiss, F. Werner, et al., *Adv. Energy Mater.* **2020**, *10*, 1903752.
- [23] A. Chirilă, P. Reinhard, F. Pianezzi, P. Bloesch, A. R. Uhl, C. Fella, L. Kranz, D. Keller, C. Gretener, H. Hagedorfer, D. Jaeger, R. Erni, S. Nishiwaki, S. Buecheler, A. N. Tiwari, *Nat. Mater.* **2013**, *12*, 1107.
- [24] M. A. Contreras, J. R. Tuttle, A. M. Gabor, A. L. Tennant, K. Ramanathan, S. Asher, A. Franz, J. Keane, L. Wang, J. H. Scofield, R. N. Noufi, in *Proc. of 1994 IEEE 1st World Conf on Photovoltaic Energy Conversion – WCPEC (A Joint Conf. of PVSC, PVSEC and PSEC)*, Vol. 1, IEEE, Piscataway, NJ **1994**, pp. 68.
- [25] J. P. Teixeira, R. B. L. Vieira, B. P. Falcaõ, M. Edoff, P. M. P. Salomé, J. P. Leitão, *J. Phys. Chem. C* **2020**, *124*, 12295.
- [26] M. Gloeckler, J. R. Sites, *J. Phys. Chem. Solids* **2005**, *66*, 1891.
- [27] S. M. Schleussner, T. Törndahl, M. Linnarsson, U. Zimmermann, T. Wätjen, M. Edoff, *Prog. Photovolt. Res. Appl.* **2012**, *20*, 284.
- [28] C. Frisk, C. Platzer-Björkman, J. Olsson, P. Szaniawski, J. T. Wätjen, V. Fjällström, P. Salomé, M. Edoff, *J. Phys. D: Appl. Phys.* **2014**, *47*, 485104.
- [29] P. M. P. Salomé, V. Fjällström, P. Szaniawski, J. P. Leitão, A. Hultqvist, P. A. Fernandes, J. P. Teixeira, B. P. Falcão, U. Zimmermann, A. F. da Cunha, M. Edoff, *Prog. Photovolt.: Res. Appl.* **2015**, *23*, 470.
- [30] K. Mitchell, C. Eberspacher, J. Ermer, D. Pier, in *Conf. Record of the 20th IEEE Photovoltaic Specialists Conf.*, IEEE, Piscataway, NJ **1988**, p. 1384.
- [31] P. Jackson, R. Wuerz, D. Hariskos, E. Lotter, W. Witte, M. Powalla, *Phys. Status Solidi RRL* **2016**, *10*, 583.
- [32] R. Brendel, H. J. Queisser, *Sol. Energy Mater. Sol. Cells* **1993**, *29*, 397.
- [33] T. Kirchartz, U. Rau, *Adv. Energy Mater.* **2018**, *8*, 1703385.
- [34] L. M. Mansfield, A. Kanevce, S. P. Harvey, K. Bowers, C. Beall, S. Glynn, I. L. Repins, *Prog. Photovolt.: Res. Appl.* **2018**, *26*, 949.
- [35] T. S. Lopes, J. Wild, C. Rocha, A. Violas, J. M. V. Cunha, J. P. Teixeira, M. A. Curado, A. J. N. Oliveira, J. Borme, G. Birant, G. Brammertz, P. A. Fernandes, B. Vermang, P. M. P. Salomé, *ACS Appl. Mater. Interfaces* **2021**, *13*, 27713.
- [36] José M. V. Cunha, K. Oliveira, J. Lontchi, T. S. Lopes, M. A. Curado, J. R. S. Barbosa, C. Vinhais, W.-C. Chen, J. Borme, H. Fonseca, J. Gaspar, D. Flandre, M. Edoff, A. G. Silva, J. P. Teixeira, P. A. Fernandes, P. M. P. Salomé, *Sol. RRL* **2021**, *5*, 2000534.
- [37] S. Suresh, J. de Wild, T. Kohl, D. G. Buldu, G. Brammertz, M. Meuris, J. Poortmans, O. Isabella, M. Zeman, B. Vermang, *Thin Solid Films* **2019**, *669*, 399.
- [38] S. Bose, J. M. V. Cunha, S. Suresh, J. De Wild, T. S. Lopes, J. R. S. Barbosa, R. Silva, J. Borme, P. A. Fernandes, B. Vermang, P. M. P. Salomé, *Sol. RRL* **2018**, *2*, 1800212.
- [39] T. S. Lopes, J. P. Teixeira, B. R. Ferreira, M. A. Curado, K. Oliveira, J. M. V. Cunha, A. J. N. Oliveira, J. R. S. Barbosa, P. Sousa, J. Borme, J. Ring, W. C. Chen, Y. Zhou, M. Edoff, G. Brammertz, P. A. Fernandes, B. Vermang, P. M. P. Salomé, Unpublished.
- [40] K. Oliveira, W. Chen, J. Lontchi, A. J. N. Oliveira, J. P. Teixeira, D. Flandre, M. Edoff, in *IEEE 48th Photovoltaic Specialists Conf. (PVSC)*, IEEE, Piscataway, NJ **2021**, p. 0928.
- [41] M. Schmid, *Semicond. Sci. Technol.* **2017**, *32*, 043003.
- [42] J. Krc, M. Sever, A. Campa, Z. Lokar, B. Lipovsek, M. Topic, *Thin Solid Films* **2017**, *633*, 193.
- [43] A. Oliveira, J. Barbosa, A. Violas, J. Teixeira, K. Oliveira, T. Lopes, J. Cunha, M. Curado, M. Monteiro, C. Rocha, C. Vinhais, P. Fernandes, P. Salomé, *Proc. SPIE 11681, Physics, Simulation, and Photonic Engineering of Photovoltaic Devices X*, **2021**, p. 1168108.
- [44] A. Razzaq, V. Depauw, J. Cho, H. S. Radhakrishnan, I. Gordon, J. Szlufcik, Y. Abdurraheem, J. Poortmans, *Sol. Energy Mater. Sol. Cells* **2020**, *206*, 110263.
- [45] Q. Huang, J. Zhao, Y. Chen, J. Wang, Y. Zhao, X. Zhang, G. Hou, *Sol. Energy Mater. Sol. Cells* **2021**, *225*, 110997.
- [46] S. Sasidharan, S. C. Pradhan, A. Jagadeesh, B. N. Nair, A. A. P. Mohamed, N. U. Narayanan, S. Soman, U. N. S. Hareesh, *ACS Appl. Energy Mater.* **2020**, *3*, 12584.
- [47] I. Ibrahim, H. N. Lim, N. W. K. Wan, N. M. Huang, S. P. Lim, W. Busayaporn, H. Nakajima, *Sol. Energy* **2021**, *215*, 403.
- [48] K. Deng, Z. Liu, M. Wang, L. Li, *Adv. Funct. Mater.* **2019**, *29*, 1900830.
- [49] C. Ma, C. Liu, J. Huang, Y. Ma, Z. Liu, L. J. Li, T. D. Anthopoulos, Y. Han, A. Fratalocchi, T. Wu, *Sol. RRL* **2019**, *3*, 1900138.
- [50] F.-J. Haug, C. Ballifa, *Energy Environ. Sci.* **2015**, *8*, 824.
- [51] J. Liu, M. Yao, L. Shen, *J. Mater. Chem. C* **2019**, *7*, 3121.
- [52] I. Massiot, A. Cattoni, S. Collin, *Nat. Energy* **2020**, *5*, 959.
- [53] C. Chen, S. Zheng, H. Song, *Chem. Soc. Rev.* **2021**, *50*, 7250.
- [54] R. Saive, *Prog. Photovolt.: Res. Appl.* **2021**, *29*, 1125.
- [55] L. Gouillart, W. C. Chen, A. Cattoni, J. Goffard, L. Riekehr, J. Keller, M. Jubault, N. Naghavi, M. Edoff, S. Collin, *IEEE J. Photovolt.* **2020**, *10*, 250.
- [56] J. Goffard, C. Colin, F. Mollica, A. Cattoni, C. Sauvan, P. Lalanne, J. Guillemoles, N. Naghavi, S. Collin, *IEEE J. Photovolt.* **2017**, *7*, 1433.
- [57] A. Ingenito, O. Isabella, M. Zeman, *ACS Photonics* **2014**, *1*, 270.
- [58] M. Ochoa, S. Buecheler, A. N. Tiwari, R. Carron, *Energy Environ. Sci.* **2020**, *13*, 2047.
- [59] P. M. P. Salomé, A. Hultqvist, V. Fjällström, B. Vermang, M. Edoff, B. Aitken, K. Zhang, K. Fuller, C. Kosik Williams, *Sol. Energy Mater. Sol. Cells* **2014**, *123*, 166.
- [60] W. Witte, S. Spiering, D. Hariskos, *Vak. Forsch. und Prax.* **2014**, *26*, 23.
- [61] V. Fjällström, P. Szaniawski, B. Vermang, P. M. P. Salomé, F. Rostvall, U. Zimmermann, M. Edoff, *IEEE J. Photovolt.* **2015**, *5*, 664.
- [62] P. M. P. Salomé, J. Keller, T. Törndahl, J. P. Teixeira, N. Nicoara, R. R. Andrade, D. G. Stroppa, J. C. González, M. Edoff, J. P. Leitão, S. Sadewasser, *Sol. Energy Mater. Sol. Cells* **2017**, *159*, 272.
- [63] P. M. P. Salomé, J. P. Teixeira, J. Keller, T. Torndahl, S. Sadewasser, J. P. Leitao, *IEEE J. Photovolt.* **2017**, *7*, 670.
- [64] D. H. Cho, W. J. Lee, M. E. Kim, B. Shin, Y. D. Chung, *Prog. Photovolt.: Res. Appl.* **2020**, *28*, 798.
- [65] A. J. N. Oliveira, J. de Wild, K. Oliveira, B. A. Valença, J. P. Teixeira, J. R. L. Guerreiro, S. Abalde-Cela, T. S. Lopes, R. M. Ribeiro, J. M. V. Cunha, M. A. Curado, M. Monteiro, A. Violas, A. G. Silva, M. Prado, P. A. Fernandes, B. Vermang, P. M. P. Salomé, *Sol. RRL* **2020**, *4*, 2000310.
- [66] R. Carron, S. Nishiwaki, T. Feurer, R. Hertwig, E. Avancini, J. Löckinger, S.-C. Yang, S. Buecheler, A. N. Tiwari, *Adv. Energy Mater.* **2019**, *9*, 1900408.
- [67] S. Yang, J. Sastre, M. Krause, X. Sun, R. Hertwig, M. Ochoa, A. N. Tiwari, R. Carron, *Sol. RRL* **2021**, *5*, 2100108.
- [68] M. Topič, M. Sever, B. Lipovšek, A. Čampa, J. Krč, *Sol. Energy Mater. Sol. Cells* **2015**, *135*, 57.
- [69] J. Krč, M. Topič, *Optical Modelling And Simulation Of Thin-Film Photovoltaic Devices*, CRC Press, Boca Raton, FL **2019**.
- [70] M. Schmid, P. Manley, A. Ott, M. Song, G. Yin, *J. Mater. Res.* **2016**, *31*, 3273.
- [71] S. Hwang, J. H. Jang, in *Conf. Record of the IEEE Photovoltaic Specialists Conf.*, IEEE, Piscataway, NJ **2012**, p. 864.
- [72] W. Shockley, H. J. Queisser, *J. Appl. Phys.* **1961**, *32*, 510.
- [73] S. Rühle, *Sol. Energy* **2016**, *130*, 139.
- [74] J. P. Teixeira, R. A. Sousa, M. G. Sousa, A. F. Da Cunha, P. A. Fernandes, P. M. P. Salomé, J. C. González, J. P. Leitão, *Appl. Phys. Lett.* **2014**, *105*, 163901.

- [75] J. P. Teixeira, P. M. P. Salomé, B. Alves, M. Edoff, J. P. Leitão, *Phys. Rev. Appl.* **2019**, *11*, 054013.
- [76] Y. Kato, S. Fujimoto, M. Kozawa, H. Fujiwara, *Phys. Rev. Appl.* **2019**, *12*, 024039.
- [77] M. A. Green, *Prog. Photovolt.: Res. Appl.* **2012**, *20*, 472.
- [78] A. Polman, M. Knight, E. C. Garnett, B. Ehrler, W. C. Sinke, *Science* **2016**, 352.
- [79] J. F. Guillemoles, T. Kirchartz, D. Cahen, U. Rau, *Nat. Photonics* **2019**, *13*, 501.
- [80] U. Rau, B. Blank, T. C. M. Müller, T. Kirchartz, *Phys. Rev. Appl.* **2017**, *7*, 044016.
- [81] N. Deka, P. Changmai, *J. Electr. Electron. Eng.* **2017**, *1*, 18.
- [82] N. Rezaei, P. Procel, M. Simor, Z. Vroon, M. Zeman, O. Isabella, *Prog. Photovolt.: Res. Appl.* **2020**, *28*, 899.
- [83] A. Čampa, J. Krč, J. Malmström, M. Edoff, F. Smole, M. Topič, *Thin Solid Films* **2007**, *515*, 5968.
- [84] B. K. Sarma, P. Rajkumar, *Mater. Today Commun.* **2020**, *23*, 100870.
- [85] M. Green, E. Dunlop, J. Hohl-Ebinger, M. Yoshita, N. Kopidakis, X. Hao, *Prog. Photovolt.: Res. Appl.* **2021**, *29*, 3.
- [86] X. Huang, H. Sanyang, W. Huang, X. Liu, *Chem. Soc. Rev.* **2013**, *42*, 173.
- [87] E. C. Garnett, B. Ehrler, A. Polman, E. Alarcon-Llado, *ACS Photonics* **2021**, *8*, 61.
- [88] M. Alexandre, M. Chapa, S. Haque, M. J. Mendes, H. Águas, E. Fortunato, R. Martins, *ACS Appl. Energy Mater.* **2019**, *2*, 2930.
- [89] R. A. S. Ferreira, S. F. H. Correia, A. Monguzzi, X. Liu, F. Meinardi, *Mater. Today* **2020**, *33*, 105.
- [90] R. Caballero, S. Siebentritt, K. Sakurai, C. A. Kaufmann, M. C. Lux-Steiner, in *Conf. Record of the 2006 IEEE 4th World Conf. on Photovoltaic Energy Conversion, WCPEC-4, IEEE Computer Society, IEEE, Piscataway, NJ* **2006**, p. 479.
- [91] P. J. Rostan, J. Mattheis, G. Bilger, U. Rau, J. H. Werner, *Thin Solid Films* **2005**, *480*, 67.
- [92] A. P. Amalathas, M. M. Alkaisy, *Micromachines* **2019**, *10*, 619.
- [93] C. S. Solanki, H. K. Singh, *Anti-Reflection And Light Trapping In C-Si Solar Cells*, Springer, Singapore **2017**.
- [94] A. S. Mohamed, H. A. Mohamed, *Indian J. Phys.* **2020**, *94*, 1725.
- [95] H. K. Raut, V. A. Ganesh, A. S. Nair, S. Ramakrishna, *Energy Environ. Sci.* **2011**, *4*, 3779.
- [96] H. S. Bae, C. Kim, I. Rhee, H. J. Jo, D. H. Kim, S. Hong, *J. Korean Phys. Soc.* **2014**, *65*, 1517.
- [97] J. A. Frantz, J. D. Myers, R. Y. Bekele, J. S. Sanghera, in *IEEE 40th Photovoltaic Specialist Conf., PVSC 2014, IEEE, Piscataway, NJ* **2014**, pp. 350–352.
- [98] R. B. Wehrspohn, U. Rau, A. Gombert, *Photon Management In Solar Cells*, Wiley-VCH Verlag, Berlin **2015**.
- [99] G. Rajan, K. Aryal, T. Ashrafee, S. Karki, A. R. Ibdah, V. Ranjan, R. W. Collins, S. Marsillac, in *IEEE 42nd Photovoltaic Specialist Conf., PVSC 2015, IEEE, Piscataway, NJ* **2015**.
- [100] N. Rezaei, O. Isabella, Z. Vroon, M. Zeman, *Sol. Energy* **2019**, *177*, 59.
- [101] N. Shahverdi, M. Yaghoubi, M. Goodarzi, A. Soleamani, *Sol. Energy* **2019**, *189*, 111.
- [102] A. Khadir, A. Kouzou, M. K. Abdelhafidi, in *Proc. of the 17th Int. Multi-Conf. on Systems, Signals and Devices, SSD 2020, IEEE, Piscataway, NJ* **2020**, p. 621.
- [103] N. El Islam Boukourt, S. Patane, in *2nd Int. Conf. on Smart Grid and Renewable Energy, SGR 2019 – Proc., IEEE, Piscataway, NJ* **2019**.
- [104] N. E. I. Boukourt, S. Patané, Y. M. Abdulraheem, *Sol. Energy* **2020**, *204*, 440.
- [105] P. Jackson, D. Hariskos, R. Wuerz, W. Wischmann, M. Powalla, *Phys. Status Solidi RRL* **2014**, *8*, 219.
- [106] N. Shanmugan, R. Pugazhendhi, R. M. Elavarasan, P. Kasiviswanathan, N. Das, *Energies* **2020**, *13*, 2631.
- [107] P. Jackson, R. Würz, U. Rau, J. Mattheis, M. Kurth, T. Schlötzer, G. Bilger, J. H. Werner, *Prog. Photovolt.: Res. Appl.* **2007**, *15*, 507.
- [108] G. Rajan, S. Karki, R. W. Collins, N. J. Podraza, S. Marsillac, *Materials* **2020**, *13*, 4259.
- [109] R. A. Mickelsen, W. S. Chen, Y. R. Hsiao, V. E. Lowe, *IEEE Trans. Electron Devices* **1984**, *31*, 542.
- [110] B. J. Stanbery, W. S. Chen, R. A. Mickelsen, G. J. Collins, K. A. Emery, J. J. Rocca, L. R. Thompson, *Sol. Cells* **1985**, *14*, 289.
- [111] NREL, *Research On Polycrystalline Thin-Film CuGaInSe2, Annual Subcontract Report*, Washington **1992**.
- [112] J. Hedstrom, H. Ohlsen, M. Bodegard, A. Klyner, L. Stolt, D. Hariskos, M. Ruckh, H. W. Schock, in *Conf. Record of the IEEE Photovoltaic Specialists Conf., IEEE, Piscataway, NJ* **1993**, p. 364.
- [113] R. Scheer, H. W. Schock, in *Chalcogenide Photovoltaics: Physics, Technologies, And Thin Film Devices*, Wiley-VCH, Hoboken, NJ **2011**.
- [114] G. Rajan, A. R. Ibdah, K. Aryal, T. Ashrafee, V. Ranjan, E. A. Pogue, A. Rockett, R. W. Collins, S. Marsillac, in *IEEE 40th Photovoltaic Specialist Conf., PVSC 2014, IEEE, Piscataway, NJ* **2014**, p. 1687.
- [115] B. T. Jheng, P. T. Liu, M. C. Wu, *Nanoscale Res. Lett.* **2014**, *9*, 331.
- [116] J. A. Frantz, J. D. Myers, R. Y. Bekele, L. E. Busse, J. S. Sanghera, *Prog. Photovolt.: Res. Appl.* **2016**, *24*, 1427.
- [117] S. K. Lee, H. J. Jeong, Y. C. Kim, J. H. Jang, *Sol. Energy Mater. Sol. Cells* **2018**, *186*, 254.
- [118] H. J. Jeong, Y. C. Kim, S. T. Kim, M. H. Choi, Y. H. Song, J. H. Yun, M. S. Park, J. H. Jang, *Micromachines* **2020**, *11*, 877.
- [119] S. Dottermusch, R. Schmager, E. Klampaftis, S. Paetel, O. Kiowski, K. Ding, B. S. Richards, U. W. Paetzold, *Prog. Photovolt.: Res. Appl.* **2019**, *27*, 593.
- [120] S. C. Baker-Finch, K. R. McIntosh, *Prog. Photovolt.: Res. Appl.* **2011**, *19*, 406.
- [121] N. Dahan, Z. Jehl, T. Hildebrandt, J. J. Greffet, J. F. Guillemoles, D. Lincot, N. Naghavi, *J. Appl. Phys.* **2012**, *112*, 094902.
- [122] E. Yablonoivitch, *J. Opt. Soc. Am.* **1982**, *72*, 899.
- [123] S.-Y. Kuo, M.-Y. Hsieh, H.-V. Han, F.-I. Lai, T.-Y. Chuang, P. Yu, C.-C. Lin, H.-C. Kuo, *Opt. Express* **2014**, *22*, 2860.
- [124] M. J. Shin, A. Lee, A. Cho, K. Kim, S. K. Ahn, J. H. Park, J. Yoo, J. H. Yun, J. Gwak, D. Shin, I. Jeong, J. S. Cho, *Nano Energy* **2021**, *82*, 105729.
- [125] A. Deinega, I. Valuev, B. Potapkin, Y. Lozovik, *J. Opt. Soc. Am. A* **2011**, *28*, 770.
- [126] B. Lipovsek, J. Krc, M. Topic, *IEEE J. Photovolt.* **2018**, *8*, 783.
- [127] Y. C. Kim, S. T. Kim, H. J. Jeong, S. K. Lee, J. S. Yoo, J. H. Jang, in *Conf. Record of the IEEE Photovoltaic Specialists Conf., IEEE, Piscataway, NJ* **2020**, p. 0890.
- [128] C. Onwudinanti, R. Vismara, O. Isabella, L. Grenet, F. Emieux, M. Zeman, *Opt. Express* **2016**, *24*, A693.
- [129] M. Amiri, A. Eskandarian, A. A. Ziabari, *Indian J. Phys.* **2020**, 2327.
- [130] L. C. Andreani, P. A. Kowalczewski, C. I. Mura, M. Patrini, M. Acciarri, S. Binetti, A. Sasselà, S. Marchionna, *27th Eur. Photovolt. Sol. Energy Conf. Exhib.* **2012**, 2334.
- [131] G. Baraldi, R. Caballero, C. A. Kaufmann, J. Gonzalo, *Energy Procedia* **2011**, *10*, 38.
- [132] S. U. Park, R. Sharma, J. K. Sim, B. J. Baek, H. K. Ahn, J. S. Kim, C. R. Lee, *Appl. Surf. Sci.* **2013**, *280*, 757.
- [133] S. C. Chen, Y. J. Chen, W. T. Chen, Y. T. Yen, T. S. Kao, T. Y. Chuang, Y. K. Liao, K. H. Wu, A. Yabushita, T. P. Hsieh, M. D. B. Charlton, D. P. Tsai, H. C. Kuo, Y. L. Chueh, *ACS Nano* **2014**, *8*, 9341.
- [134] S. Collin, J. Goffard, A. Cattoni, C. Colin, C. Sauvan, P. Lalanne, J. F. Guillemoles, in *IEEE 42nd Photovoltaic Specialist Conf., PVSC 2015, IEEE, Piscataway, NJ* **2015**.

- [135] M. J. Jeng, Z. Y. Chen, Y. L. Xiao, L. B. Chang, J. Ao, Y. Sun, E. Popko, W. Jacak, L. Chow, *Materials* **2015**, *8*, 6761.
- [136] Y. C. Lin, X. C. Wei, *Chinese J. Phys.* **2017**, *55*, 1219.
- [137] Z. Yang, J. Wang, Z. Cheng, H. Yin, W. Wang, Y. Huang, X. Ren, *OSA Contin.* **2018**, *1*, 1313.
- [138] S. M. S. Hasheminassab, M. Imanieh, A. Kamali, S. A. Emamghorashi, S. Hassanhosseini, *Plasmonics* **2021**, *16*, 273.
- [139] M. Schmid, G. Yin, M. Song, S. Duan, B. Heidmann, D. Sancho-Martinez, S. Kämmer, T. Köhler, P. Manley, M. C. Lux-Steiner, *J. Photonics Energy* **2017**, *7*, 018001.
- [140] M. Y. Hsieh, S. Y. Kuo, F. I. Lai, H. V. Han, T. Y. Chuang, H. C. Kuo, in *2013 IEEE 5th International Nanoelectronics Conference (INEC)*, Singapore, **2013**, p. 411.
- [141] G. Yin, M. Song, S. Duan, P. Manley, D. Greiner, C. A. Kaufmann, M. Schmid, *ACS Appl. Mater. Interfaces* **2016**, *8*, 31646.
- [142] A. Chutinan, N. P. Kherani, S. Zukotynski, *Opt. Express* **2009**, *17*, 8871.
- [143] M. A. Garcia, *J. Phys. D: Appl. Phys.* **2011**, *44*, 283001.
- [144] Koichi Okamoto, Mitsuru Funato, Yoichi Kawakami, Kaoru Tamada, *J. Photochem. Photobiol. C: Photochem. Rev.* **2017**, *32*, 58.
- [145] C. F. Bohren, D. R. Huffman, *Absorption And Scattering Of Light By Small Particles*, WILEY-VCH, Verlag, Berlin, **1998**.
- [146] H. A. Atwater, A. Polman, *Nat. Mater.* **2010**, *9*, 205.
- [147] M. L. Brongersma, P. G. Kik, *Surface Plasmon Nanophotonics* Springer, The Netherlands **2007**.
- [148] G. Yin, A. Steigert, P. Andrae, M. Goebelt, M. Latzel, P. Manley, I. Laueremann, S. Christiansen, M. Schmid, *Appl. Surf. Sci.* **2015**, *355*, 800.
- [149] M. J. Mendes, S. Morawiec, F. Simone, *Nanoscale* **2014**, *6*, 4796.
- [150] W. Wang, L. Qi, *Adv. Funct. Mater.* **2019**, *29*, 1807275.
- [151] Y. A. Akimov, W. S. Koh, S. Y. Sian, S. Ren, *Appl. Phys. Lett.* **2010**, *96*, 073111.
- [152] A. I. Kuznetsov, A. E. Miroshnichenko, M. L. Brongersma, Y. S. Kivshar, B. Luk'Yanchuk, *Science* **2016**, *354*, 6314.
- [153] J. Grandidier, D. M. Callahan, J. N. Munday, H. A. Atwater, *IEEE J. Photovolt.* **2012**, *2*, 123.
- [154] M. López-García, J. F. Galisteo-López, C. López, A. García-Martín, *Phys. Rev. B* **2012**, *85*, 235145.
- [155] P. Spinelli, M. A. Verschuuren, A. Polman, *Nat. Commun.* **2012**, *3*, 699.
- [156] M. van Lare, F. Lenzenmann, A. Polman, *Opt. Express* **2013**, *21*, 20738.
- [157] G. Yin, P. Manley, M. Schmid, *Sol. Energy Mater. Sol. Cells* **2016**, *153*, 124.
- [158] L. Rayleigh, *Proc. Lond. Math. Soc.* **1879**, *s1-11*, 51.
- [159] S. Y. Han, C. Pan, D. H. Kim, C. H. Chang, *RSC Adv.* **2015**, *5*, 24712.
- [160] G. Wakefield, M. Adair, M. Gardener, D. Greiner, C. A. Kaufmann, J. Moghal, *Sol. Energy Mater. Sol. Cells* **2015**, *134*, 359.
- [161] S. A. Boden, D. M. Bagnall, *Prog. Photovolt.: Res. Appl.* **2010**, *18*, 195.
- [162] P. Lalanne, J.-P. Hugonin, *J. Opt. Soc. Am. A* **1998**, *15*, 1843.
- [163] P. B. Clapham, M. C. Hutley, *Nature* **1973**, *244*, 281.
- [164] X. Guo, Q. Liu, H. Tian, B. Li, H. Zhou, C. Li, A. Hu, X. He, *J. Semicond.* **2019**, *40*, 032702.
- [165] C. F. J. Kuo, H. M. Tu., T. L. Su, *J. Appl. Polym. Sci.* **2006**, *102*, 5303.
- [166] A. Jacobo-Martín, J. J. Hernández, P. Pedraz, I. Navarro-Baena, M. A. Monclús, J. M. Molina-Aldareguia, I. Rodríguez, *Adv. Eng. Mater.* **2021**, *23*, 2100603.
- [167] K. Cheng, R. Jin, J. Liu, X. Liu, J. Liu, Z. Lu, Y. Liu, L. Guo, Z. Du, *Sol. Energy Mater. Sol. Cells* **2017**, *170*, 211.
- [168] K. C. Park, H. J. Choi, C. H. Chang, R. E. Cohen, G. H. McKinley, G. Barbastathis, *ACS Nano* **2012**, *6*, 3789.
- [169] M. Burghoorn, B. Kniknie, J. Van Deelen, M. Xu, Z. Vroon, R. Van Ee, R. Van De Belt, P. Buskens, *AIP Adv.* **2014**, *4*, 127154.
- [170] H. J. Jeong, Y. C. Kim, S. K. Lee, J. H. Yun, J. H. Jang, *Sol. Energy Mater. Sol. Cells* **2019**, *194*, 177.
- [171] B. H. Shim, J. W. Kang, H. Jeong, Y. Jeong, T. P. Kumar, J. H. Jang, S. J. Park, *Thin Solid Films* **2016**, *603*, 103.
- [172] F. I. Lai, M. Y. Hsieh, J. F. Yang, Y. C. Hsu, S. Y. Kuo, *Int. J. Energy Res.* **2021**, *45*, 1142.
- [173] M. Brozak, H. Cansizoglu, T. Karabacak, in *IEEE 42nd Photovoltaic Specialist Conf., PVSC 2015*, IEEE, Piscataway, NJ **2015**.
- [174] J. R. Sharma, P. Banerjee, S. Mitra, H. Ghosh, S. Bose, G. Das, S. Mukhopadhyay, *J. Mater. Sci. Mater. Electron.* **2019**, *30*, 11017.
- [175] M. K. Kim, D. K. Yi, U. Paik, *Langmuir* **2010**, *26*, 7552.
- [176] B. K. Shin, T. Il Lee, J. Xiong, C. Hwang, G. Noh, J. H. Cho, J. M. Myoung, *Sol. Energy Mater. Sol. Cells* **2011**, *95*, 2650.
- [177] P. M. P. Salomé, V. Fjallstrom, A. Hultqvist, P. Szaniawski, U. Zimmermann, M. Edoff, *Prog. Photovolt.: Res. Appl.* **2014**, *22*, 83.
- [178] K. H. Ong, R. Agileswari, B. Maniscalco, P. Arnou, C. C. Kumar, J. W. Bowers, M. B. Marsadek, *Int. J. Photoenergy* **2018**, 9106269.
- [179] D. Fraga, T. S. Lyubenova, A. Rey, I. Calvet, R. Martí, J. B. Carda, *Int. J. Appl. Ceram. Technol.* **2015**, *12*, 728.
- [180] T. Feurer, P. Reinhard, E. Avancini, B. Bissig, J. Löckinger, P. Fuchs, R. Carron, T. P. Weiss, J. Perrenoud, S. Stutterheim, S. Buecheler, A. N. Tiwari, *Prog. Photovolt.: Res. Appl.* **2017**, *25*, 645.
- [181] G. Yin, M. Song, M. Schmid, *Sol. Energy Mater. Sol. Cells* **2019**, *195*, 318.
- [182] P. Blösch, D. Güttler, A. Chirila, A. N. Tiwari, *Thin Solid Films*, **2011**, *519*, 7453.
- [183] J. K. Larsen, H. Simchi, P. Xin, K. Kim, W. N. Shafarman, *Appl. Phys. Lett.* **2014**, *104*, 033901.
- [184] Z. J. Li-Kao, N. Naghavi, F. Erfurth, J. F. Guillemoles, I. Gérard, A. Etcheberry, J. L. Pelouard, S. Collin, G. Voorwinden, D. Lincot, *Prog. Photovolt.: Res. Appl.* **2012**, *20*, 582.
- [185] K. Orgassa, H. W. Schock, J. H. Werner, in *Thin Solid Films* **2003**, *431-432*, 387.
- [186] S. Schleussner, T. Kubart, T. Törndahl, M. Edoff, *Thin Solid Films* **2009**, *517*, 5548.
- [187] P. M. P. Salomé, B. Vermang, R. Ribeiro-Andrade, J. P. Teixeira, J. M. V. Cunha, M. J. Mendes, S. Haque, J. Borme, H. Águas, E. Fortunato, R. Martins, J. C. González, J. P. Leitão, P. A. Fernandes, M. Edoff, S. Sadewasser, *Adv. Mater. Interfaces* **2018**, *5*, 1701101.
- [188] G. Birant, J. de Wild, M. Meuris, J. Poortmans, B. Vermang, *Appl. Sci.* **2019**, *9*, 677.
- [189] B. Vermang, J. T. Wätjen, V. Fjällström, F. Rostvall, M. Edoff, R. Gunnarsson, I. Pilch, U. Helmersson, R. Kotipalli, F. Henry, D. Flandre, *Thin Solid Films* **2015**, *582*, 300.
- [190] S. Bose, J. M. V. Cunha, J. Borme, W. C. Chen, N. S. Nilsson, J. P. Teixeira, J. Gaspar, J. P. Leitão, M. Edoff, P. A. Fernandes, P. M. P. Salomé, *Thin Solid Films* **2019**, *671*, 77.
- [191] T. S. Lopes, J. M. V. Cunha, S. Bose, J. R. S. Barbosa, J. Borme, O. Donzel-Gargand, C. Rocha, R. Silva, A. Hultqvist, W. C. Chen, A. G. Silva, M. Edoff, P. A. Fernandes, P. M. P. Salomé, *IEEE J. Photovolt.* **2019**, *9*, 1421.
- [192] J. M. V. Cunha, T. S. Lopes, S. Bose, A. Hultqvist, W.-C. Chen, O. Donzel-Gargand, R. M. Ribeiro, A. J. N. Oliveira, M. Edoff, P. A. Fernandes, P. M. P. Salomé, *IEEE J. Photovolt.* **2019**, *9*, 1857.
- [193] L. Gouillart, A. Cattoni, W. C. Chen, J. Goffard, L. Riekehr, J. Keller, M. Jubault, N. Naghavi, M. Edoff, S. Collin, *Prog. Photovolt.: Res. Appl.* **2021**, *29*, 212.
- [194] L. Gouillart, A. Cattoni, J. Goffard, F. Donsanti, G. Patriarche, M. Jubault, N. Naghavi, S. Collin, *Thin Solid Films* **2019**, *672*, 1.
- [195] F. Mollica, M. Jubault, F. Donsanti, A. Loubat, M. Bouttemy, A. Etcheberry, N. Naghavi, *Thin Solid Films* **2017**, *633*, 202.



- [196] P. M. P. Salomé, R. Ribeiro-Andrade, J. P. Teixeira, J. Keller, T. Torndahl, N. Nicoara, M. Edoff, J. C. Gonzalez, J. P. Leitao, S. Sadewasser, *IEEE J. Photovolt.* **2017**, *7*, 858.
- [197] J. Malmström, S. Schleussner, L. Stolt, *Appl. Phys. Lett.* **2004**, *85*, 2634.
- [198] S. Choi, Y. Kamikawa, J. Nishinaga, A. Yamada, H. Shibata, S. Niki, *Thin Solid Films* **2018**, *665*, 91.
- [199] J. M. V. Cunha, P. A. Fernandes, A. Hultqvist, J. P. Teixeira, S. Bose, B. Vermang, S. Garud, D. Buldu, J. Gaspar, M. Edoff, J. P. Leitao, P. M. P. Salomé, *IEEE J. Photovolt.* **2018**, *8*, 1313.
- [200] J. Lontchi, M. Zhukova, M. Kovacic, J. Krc, W. Chen, M. Edoff, S. Bose, P. M. P. Salomé, J. Goffard, A. Cattoni, L. Guillard, S. Collin, V. Gusak, D. Flandre, *IEEE J. Photovolt.* **2020**, *10*, 1908.
- [201] T. Nakada, Y. Hirabayashi, T. Tokado, D. Ohmori, T. Mise, *Sol. Energy* **2004**, *77*, 739.
- [202] W. Ohm, W. Riedel, U. Aksunger, D. Greiner, C. A. Kaufmann, M. C. Lux-Steiner, S. Gledhill, in *IEEE 42nd Photovoltaic Specialist Conf., PVSC 2015*, IEEE, Piscataway, NJ **2015**.
- [203] J. Keller, W. C. Chen, L. Riekehr, T. Kubart, T. Torndahl, M. Edoff, *Prog. Photovolt.: Res. Appl.* **2018**, *26*, 846.
- [204] M. D. Heinemann, V. Efimova, R. Klenk, B. Hoepfner, M. Wollgarten, T. Unold, H. W. Schock, C. A. Kaufmann, *Prog. Photovolt.: Res. Appl.* **2015**, *23*, 1228.
- [205] J. Chantana, H. Arai, Y. Niizawa, T. Minemoto, *Thin Solid Films* **2016**, *616*, 17.
- [206] F. J. Haug, D. Rudmann, G. Bilger, H. Zogg, A. N. Tiwari, *Thin Solid Films* **2002**, *403*, 293.
- [207] M. Terheggen, H. Heinrich, G. Kostorz, F. J. Haug, H. Zogg, A. N. Tiwari, *Thin Solid Films*, **2002**, *403*, 212.
- [208] M. D. Heinemann, F. Ruske, D. Greiner, A. R. Jeong, M. Rusu, B. Rech, R. Schlatmann, C. A. Kaufmann, *Sol. Energy Mater. Sol. Cells* **2016**, *150*, 76.
- [209] D. Rudmann, A. F. da Cunha, M. Kaelin, F.-J. Haug, H. Zogg, A. N. Tiwari, *MRS Proc.* **2003**, *763*, B1.9.
- [210] S. R. Park, J. Y. Baek, T. Y. Yun, H. J. Han, K. B. Kim, C. W. Jeon, *Mol. Cryst. Liq. Cryst.* **2013**, *585*, 114.
- [211] Q. Sun, K. B. Kim, C. W. Jeon, *J. Nanosci. Nanotechnol.* **2016**, *16*, 5053.
- [212] L. Ji, W. J. Nam, S. Fonash, *Conf. Record of the IEEE Photovoltaic Specialists Conf.*, IEEE, Piscataway, NJ, **2013**, p. 1977.
- [213] M. Kovacic, J. Krc, B. Lipovsek, W. C. Chen, M. Edoff, P. J. Bolt, J. van Deelen, M. Zhukova, J. Lontchi, D. Flandre, P. Salomé, M. Topic, *Sol. Energy Mater. Sol. Cells* **2019**, *200*, 109933.
- [214] L. Grenet, F. Emieueux, O. Dellea, A. Gerthoffer, G. Lorin, F. Roux, S. Perraud, *Thin Solid Films* **2017**, *621*, 188.
- [215] T. Schneider, J. Tröndle, B. Fuhrmann, F. Syrowatka, A. Sprafke, R. Scheer, *Sol. RRL* **2020**, *4*, 2000295.
- [216] C. Van Lare, G. Yin, A. Polman, M. Schmid, *ACS Nano* **2015**, *9*, 9603.
- [217] G. Yin, M. W. Knight, M. C. van Lare, M. M. Solà Garcia, A. Polman, M. Schmid, *Adv. Opt. Mater.* **2017**, *5*, 1600637.
- [218] Y. C. Wang, C. W. Chen, T. Y. Su, T. Y. Yang, W. W. Liu, F. Cheng, Z. M. Wang, Y. L. Chueh, *Nano Energy* **2020**, *78*, 105225.
- [219] G. Yin, P. Manley, M. Schmid, *Sol. Energy* **2018**, *163*, 443.
- [220] K. Oliveira, W. Chen, J. Lontchi, A. J. N. Oliveira, J. P. Teixeira, D. Flandre, M. Edoff, P. Fernandes, P. Salomé, Unpublished.
- [221] S. Morawiec, M. J. Mendes, S. A. Filonovich, T. Mateus, S. Mirabella, H. Águas, I. Ferreira, F. Simone, E. Fortunato, R. Martins, F. Priolo, I. Crupi, *Opt. Express* **2014**, *22*, A1059.
- [222] M. Mirzaei, J. Hasanzadeh, A. A. Ziabari, *J. Electron. Mater.* **2020**, *49*, 7168.
- [223] M. Schmid, R. Klenk, M. C. Lux-Steiner, M. Topič, J. Krč, *Nanotechnology* **2011**, *22*, 025204.
- [224] M. Schmid, J. Klaer, R. Klenk, M. Topič, J. Krč, *Thin Solid Films* **2013**, *527*, 308.
- [225] L. D. Carlos, R. A. S. Ferreira, V. De Zea Bermudez, B. Julián-López, P. Escribano, *Chem. Soc. Rev.* **2011**, *40*, 536.
- [226] Y. Li, H. Lin, J. Zeng, J. Chen, H. Chen, *Sol. Energy* **2019**, *193*, 303.
- [227] M. A. Cardoso, S. F. H. Correia, A. R. Frias, H. M. R. Gonçalves, R. F. P. Pereira, S. C. Nunes, M. Armand, P. S. André, V. de Zea Bermudez, R. A. S. Ferreira, *J. Rare Earths* **2020**, *38*, 531.
- [228] B. McKenna, R. C. Evans, *Adv. Mater.* **2017**, *29*, 1606491.
- [229] A. Gavriluta, T. Fix, A. Nonat, A. Slaoui, J. F. Guillemoles, L. J. Charbonnière, *Eur. J. Inorg. Chem.* **2017**, *2017*, 5318.
- [230] A. Solodovnyk, C. Kick, A. Osvet, H. J. Egelhaaf, E. Stern, M. Batentschuk, K. Forberich, C. J. Brabec, *Energy Technol.* **2016**, *4*, 385.
- [231] T. Uekert, A. Solodovnyk, S. Ponomarenko, A. Osvet, I. Levchuk, J. Gast, M. Batentschuk, K. Forberich, E. Stern, H. J. Egelhaaf, C. J. Brabec, *Sol. Energy Mater. Sol. Cells* **2016**, *155*, 1.
- [232] A. Gavriluta, T. Fix, A. Nonat, A. Slaoui, J. F. Guillemoles, L. J. Charbonnière, *J. Mater. Chem. A* **2017**, *5*, 14031.
- [233] M. Nazim, B. Kim, S. Lee, B. K. Min, J. H. Kim, *Energy Fuels* **2020**, *34*, 14581.
- [234] H. Jintoku, M. Yamaguchi, M. Takafuji, H. Ihara, *Adv. Funct. Mater.* **2014**, *24*, 4105.
- [235] K. Bouras, G. Schmerber, H. Rinnert, D. Aureau, H. Park, G. Ferblantier, S. Colis, T. Fix, C. Park, W. K. Kim, A. Dinia, A. Slaoui, *Sol. Energy Mater. Sol. Cells* **2016**, *145*, 134.
- [236] K. Bouras, G. Schmerber, G. Ferblantier, D. Aureau, H. Park, W. K. Kim, H. Rinnert, A. Dinia, A. Slaoui, S. Colis, *ACS Appl. Energy Mater.* **2019**, *2*, 5094.
- [237] Y. Park, G. Ferblantier, A. Slaoui, A. Dinia, H. Park, S. Alhammadi, W. K. Kim, *J. Alloys Compd.* **2020**, *815*, 152360.
- [238] Y. K. Liao, M. Brossard, D. H. Hsieh, T. N. Lin, M. D. B. Charlton, S. J. Cheng, C. H. Chen, J. L. Shen, L. T. Cheng, T. P. Hsieh, F. I. Lai, S. Y. Kuo, H. C. Kuo, P. G. Savvidis, P. G. Lagoudakis, *Adv. Energy Mater.* **2015**, *5*, 1401280.
- [239] E. Tatsu, G. Griffini, *Sol. Energy Mater. Sol. Cells* **2019**, *196*, 43.
- [240] B. González-Díaz, C. Hernández-Rodríguez, D. Cañadillas-Ramallo, J. Sanchiz, R. Guerrero-Lemus, in *IEEE 7th World Conf. on Photovoltaic Energy Conversion (WCPEC) (A Joint Conf. of 45th IEEE PVSC, 28th PVSEC & 34th EU PVSEC)*, IEEE, Piscataway, NJ **2018**, 2882.
- [241] B. González-Díaz, M. Saw, C. Hernández-Rodríguez, J. Sanchiz, Y. S. Khoo, R. Guerrero-Lemus, *Mater. Sci. Eng. B-Adv. Funct. Solid-State Mater.* **2020**, *261*, 114763.
- [242] A. M. Gabr, A. Walker, A. Trojnar, T. J. Hall, R. N. Kleiman, K. Hinzler, in *Conf. Record of the IEEE Photovoltaic Specialists Conf.*, IEEE, Piscataway, NJ **2013**, p. 1003.
- [243] A. Solodovnyk, A. Hollmann, A. Osvet, K. Forberich, E. Stern, M. Batentschuk, R. Klupp Taylor, C. J. Brabec, in *Next Generation Technologies for Solar Energy Conversion V*, SPIE, Bellingham, WA **2014**, 917806.
- [244] E. Klampaftis, D. Ross, S. Seyrling, A. N. Tiwari, B. S. Richards, *Sol. Energy Mater. Sol. Cells* **2012**, *101*, 62.
- [245] D. Alonso-Álvarez, D. Ross, E. Klampaftis, K. R. McIntosh, S. Jia, P. Storiz, T. Stolz, B. S. Richards, *Prog. Photovolt.: Res. Appl.* **2015**, *23*, 479.
- [246] E. Klampaftis, B. S. Richards, *Prog. Photovolt.: Res. Appl.* **2011**, *19*, 345.
- [247] D. Ross, E. Klampaftis, J. Fritsche, M. Bauer, B. S. Richards, *Sol. Energy Mater. Sol. Cells* **2012**, *103*, 11.
- [248] G. C. Glaeser, U. Rau, *Thin Solid Films* **2007**, *515*, 5964.

- [249] Z. Xiong, J. Gong, Y. Xiong, Y. Lan, M. Yin, Z. Ding, Z. Zhang, X. Xiao, *Sol. RRL* **2020**, *4*, 1900518.
- [250] B. G. Jeong, D. Hahm, J. W. Park, J. Y. Kim, H. E. Song, M. G. Kang, S. Jeong, G. Kang, W. K. Bae, H. J. Song, *Nano Energy* **2020**, *77*, 105169.
- [251] A. Solodovnyk, C. Kick, A. Osvet, H.-J. Egelhaaf, E. Stern, M. Batentschuk, K. Forberich, C. J. Brabec, in *Physics, Simulation, And Photonic Engineering Of Photovoltaic Devices V*, SPIE, Bellingham, WA **2016**, p. 97430G.
- [252] H. J. Jeong, Y. C. Kim, S. K. Lee, Y. Jeong, J. W. Song, J. H. Yun, J. H. Jang, *ACS Appl. Mater. Interfaces* **2017**, *9*, 25404.
- [253] Y. C. Kim, H. J. Jeong, S. T. Kim, Y. H. Song, B. Y. Kim, J. P. Kim, B. K. Kang, J. H. Yun, J. H. Jang, *Nanoscale* **2020**, *12*, 558.
- [254] European Commission, *Critical Raw Materials Resilience: Charting A Path Towards Greater Security And Sustainability*, Brussels **2020**.
- [255] F. Khan, J. H. Kim, *ACS Photonics* **2018**, *5*, 4637.
- [256] F. Khan, J. H. Kim, *Sci. Rep.* **2019**, *9*, 10803.
- [257] F. Sui, M. Pan, Z. Wang, M. Chen, W. Li, Y. Shao, W. Li, C. Yang, *Sol. Energy* **2020**, *206*, 473.
- [258] T. Trupke, M. A. Green, P. Würfel, *J. Appl. Phys.* **2002**, *92*, 1668.
- [259] S. Hoseinkhani, R. Tubino, F. Meinardi, A. Monguzzi, *Phys. Chem. Chem. Phys.* **2015**, *17*, 4020.
- [260] Y. C. Simon, C. Weder, *J. Mater. Chem.* **2012**, *22*, 20817.
- [261] Q. Liu, T. Yang, W. Feng, F. Li, *J. Am. Chem. Soc.* **2012**, *134*, 5390.
- [262] I. Kozinsky, Y. X. Yeng, Y. Huang, In *Materials Research Society Symposium Proceedings Library* **2014**, *1638*, p. 402.
- [263] M. D. Archer, M. A. Green, in *Clean Electricity For Photovoltaics*, 2nd edn, Imperial College Press, Singapore **2015**.
- [264] J. Haynos, J. Allison, R. Arndt, A. Meulenber, in *Int. Conf. on Photovoltaic Power Generation*, Hamburg **1974**, p. 487.
- [265] M. Ochoa, S. Nishiwaki, S. Yang, A. N. Tiwari, R. Carron, *Phys. Status Solidi RRL* **2021**, *15*, 2100313.
- [266] Z. W. Han, Z. Wang, X. M. Feng, B. Li, Z. Z. Mu, J. Q. Zhang, S. C. Niu, L. Q. Ren, *Biosurf. Biotribol.* **2016**, *2*, 137.
- [267] P. Centeno, M. F. Alexandre, M. Chapa, J. V. Pinto, J. Deuermeier, T. Mateus, E. Fortunato, R. Martins, H. Águas, M. J. Mendes, *Adv. Mater. Interfaces* **2020**, *7*, 2000264.
- [268] C. Feng, T. Gou, J. Li, Y. Cai, P. He, J. Huang, Y. Wen, Y. Ma, Z. Zhang, *Mater. Res. Express* **2019**, *6*, 075319.
- [269] S. Fischer, E. Favilla, M. Tonelli, J. C. Goldschmidt, *Sol. Energy Mater. Sol. Cells* **2015**, *136*, 127.
- [270] S. Fischer, R. Martín-Rodríguez, B. Fröhlich, K. W. Krämer, A. Meijerink, J. C. Goldschmidt, *J. Lumin.* **2014**, *153*, 281.
- [271] Ansys/Lumerical, <https://www.lumerical.com/ansys/>, (accessed: June 2021).
- [272] W. S. M. Werner, K. Glantschnig, C. Ambrosch-Draxl, *J. Phys. Chem. Ref. Data* **2009**, *38*, 1013.
- [273] A. R. Beal, H. P. Hughes, *J. Phys. C Solid State Phys.* **1979**, *12*, 881.
- [274] G. Rajan, T. Begou, K. Aryal, T. Ashrafee, S. Karki, V. Ranjan, A. A. Rockett, N. J. Podraza, R. W. Collins, S. Marsillac, in *Conf. Record of the IEEE Photovoltaic Specialists Conf.*, IEEE, Piscataway, NJ, **2016**, p. 1506.
- [275] Y. C. Wang, H. Y. Cheng, Y. T. Yen, T. T. Wu, C. H. Hsu, H. W. Tsai, C. H. Shen, J. M. Shieh, Y. L. Chueh, *ACS Nano* **2015**, *9*, 3907.
- [276] L. Aé, D. Kieven, J. Chen, R. Klenk, T. Rissom, Y. Tang, M. Ch Lux-Steiner, *Prog. Photovolt.: Res. Appl.* **2010**, *18*, 209.
- [277] D. Li, Z. Liu, Y. Wang, Y. Shan, F. Huang, *J. Mater. Sci. Technol.* **2015**, *31*, 229.
- [278] B. Fritz, R. Hünig, M. Guttmann, M. Schneider, K. M. S. Reza, O. Salomon, P. Jackson, M. Powalla, U. Lemmer, G. Gomard, *Sol. Energy* **2020**, *201*, 666.



**António J. N. Oliveira** concluded his integrated master's degree in micro- and nanotechnologies Engineering at School of Science and Technology, New University of Lisbon, in November 2019. His master thesis was performed at the International Iberian Nanotechnology laboratory (INL), where he developed novel light management structures for ultrathin chalcogenide solar cells. Currently, he is pursuing a Ph.D. in physics engineering in University of Aveiro and INL with a competitive FCT Ph.D. grant. He works on the incorporation of plasmonic/photonic nanostructures in solar cell devices, with the finality to increase the optoelectronic performance of solar cell devices while reducing manufacturing costs.



**Jennifer P. Teixeira** is currently working as a postdoc research fellow at the International Iberian Nanotechnology Laboratory, in the Nanofabrication for Optoelectronic Applications group. She received in 2019 a Ph.D. in physics at University of Aveiro, working on the topic of advanced characterization for the identification of recombination losses in thin-film solar cells. Her current research focuses on the development of novel ultrathin solar cell architecture and advanced characterization of charge carrier dynamics in energy materials. She is involved in several national, industrial, and European projects, where she enters as project manager with her vast know-how in semiconductor and materials.



**Duarte Ramos** is a student doing his integrated masters in microelectronic and nanotechnology engineering. He is currently developing his master thesis at the International Iberian Nanotechnology Laboratory, in the Nanofabrication for Optoelectronic Applications group. His research interests center on CIGS thin-film solar cells, mainly on device fabrication, as well as electrical, optical, and material characterization.



**Paulo Fernandes** is currently an associated researcher of the NOA research group at INL, Braga, and adjunct professor of the Department of Physics, School of Engineering, Polytechnic Institute of Porto. His research work is focused on two main areas: the study of new semiconductors for energy harvesting and detection applications in micro- and nanodevices and, the research in passivation techniques and new materials and architectures for thin-film photovoltaic devices. He is also a researcher at the I3N Associated Lab at the University of Aveiro and at CIETI research group School of Engineering, Polytechnic Institute of Porto.



**Pedro Salomé** is the group leader of the Nanofabrication for Optoelectronic Applications group at the International Iberian Nanotechnology laboratory (INL) and received his doctoral degree in the field of applied physics from the University of Aveiro, Portugal, in 2011. He has published over 90 papers in peer-reviewed international journals, having generated 4000 citations with a *h*-factor of 32 (Scopus). He has submitted three patents to the European patent office, being active in the development of renewable energy and nanotechnology, and often contributes with talks at universities, schools, and companies, doing science promotion and connecting the industry with the research community.